Diffusion-weighted Imaging of Lymph Node Tissue

Mariaulpa Sahalan

A thesis submitted in fulfilment of the requirements for the degree of
Doctor of Philosophy

Faculty of Health Sciences

University of Sydney

February 2019

Supervisor's statement

I, Roger Bourne confirm that the work presented in this thesis is that of Mariaulpa Sahalan. It does not contain previously published or written material by another person, except where specifically indicated in the thesis. It does not contain material that has been accepted for award of another degree. This work is based on research conducted under my supervision at the University of Sydney during the time period of March 2013 - September 2016.

Dr Roger M Bourne

Discipline of Medical Radiation Sciences

Faculty of Health Sciences

University of Sydney

02 February 2019

Candidate's statement

I, Mariaulpa Sahalan confirm that the work presented in this thesis in my own. It does not contain previously published or written material by another person, except where specifically indicated in the thesis. It does not contain material that has been accepted for award of another degree. This work is based on research conducted by me at the University of Sydney during the time period of March 2013 - September 2016.

Mariaulpa Sahalan

Faculty of Health Sciences,

The University of Sydney

02 February 2019

Abstract

Purpose

The development of the full potential of diffusion-weighted imaging (DWI) methods for lymph node cancer assessment depends on understanding how water diffusion is affected by the changes in tissue structure that characterise the presence of cancer. However, the biophysical basis of diffusion contrast in lymph node tissue is not well understood. The present study aims to define the biophysical basis of contrast in DWI of the lymph node. It investigates the hypothesis that the clinically observed decreased apparent diffusion coefficient (ADC) of cancerous lymph nodes can be attributed to increased cellularity. The study characterises the microscopic structures of nodes and investigates the correlation between mean diffusivity (MD) and cellularity metrics using DWI from high-resolution 16.4 Tesla MRI. The contrast in DWI images in the present study are based on T2 weighting of the MR signal. It also investigates the theoretical information content of single and multi-biophysical models that include combinations of isotropic, anisotropic, and restricted components in lymph node tissues.

Materials and Methods

Lymph node tissue samples were obtained from humans and animals with institutional ethical approval and written consent from all participating patients. The samples were immersed in 10% neutral buffered formalin post-surgery. A 3 mm diameter core sample was extracted from the tissue using a core punch. The cores were glued to a plastic strip, inserted into a 2 mL screw-top plastic vial and immersed in phosphate-buffered saline (PBS) solution.

For MD measurement, imaging was performed on a Bruker AV700 magnetic resonance microimaging system of a 16.4 T vertical bore magnet with spectrometer running Paravision 4 and a 5 mm bird cage radiofrequency coil. The scanner was equipped with a Micro 2.5 Gradient Set with gradients strength of 2.5 mT/m. For diffusion modelling, the imaging was performed on a 9.4T Bruker system equipped with 72 mm quadrature RF coil and BGA-12S HP gradients with maximum strength of 660 mT/m and slew rate of 4570 T/m/s. A 3D spin echo sequence was employed for diffusion modelling and a 3D spin echo diffusion tensor

imaging (DTI) sequence was employed for microimaging. Both imaging were performed at a monitored room temperature (22 $^{\circ}$C).

Samples were sectioned and stained with haematoxylin and eosin (H&E). Sample slides were digitally scanned at 40× magnification with a spatial resolution of 0.25 microns per pixel using a digital brightfield microscope (Aperio Scan Scope). Diffusion tensor model was fitted voxelwise and MD values were computed using Matlab as: $MD = (\lambda_1 + \lambda_2 + \lambda_3)/3$, where λ_1, λ_2 and λ_3 are the eigenvalues of the diffusion tensor matrix. Then regions of interest (ROIs) were drawn over the sub-structures of interest of the region most representative of the sub-structure of interest on MD images. The sub-structures and histopathological status of the tissue on the selected ROIs were confirmed by an expert pathologist and drawn on the color printed images of H&E slices. The ROIs on MD images was defined to avoid any error due to chemical shift artefact. A MATLAB code was used to views multiples MD images at separation depth from (50 - 200 µm) and subjectively assesses to a satisfied match between MD images with the histological sections. Adjacent MR slices were also checked for discrepancy and to minimize partial volume effects. Measurement of cellularity metrics, including nuclear count and nuclear area, was performed using Image Pro Premier software with semi-automatic segmentation.

For diffusion modelling a total of eleven models, including different combinations of isotropic, anisotropic, and restricted components were tested. Each model was fitted to the data using the Levenberg-Marquardt minimisation algorithm in the open source Camino toolkit. Models were ranked using the Akaike information criterion (AIC), which compared models in terms of theoretical information content (1). SPSS, version 21.0 was used for statistical analysis.

Results

The sub-structures present in DWI images corresponded closely to the histological features seen on light microscopy of stained sections. The findings showed distinct diffusivities of lymph node sub-structures (capsule, parenchyma, and artery). This is consistent with recent reports of distinct diffusivities in prostate and breast tissue sub-structures (2,3). Parenchyma in normal lymph node tissues had higher MD (0.71 ± 0.17 µm^2/ms) than metastatic parenchyma (0.52 ± 0.08 µm^2/ms) and lymphoma (0.47 ± 0.19 µm^2/ms). Capsule in normal node tissues showed a higher MD (1.15 ± 0.16 µm^2/ms) than capsule in metastatic tissues

$(1.07 \pm 0.17 \ \mu m^2/ms)$. The Kruskal-Wallis test indicated a statistically significant difference of MD values in parenchyma in the three tissue types, $\chi^2(2) = 6.129$, ($p = 0.047$).alignment

No correlation was observed between the two independent variables, MD and nuclear count with $r = 0.368$, n =69 at 95 % confidence intervals. For MD and nuclear area there was no correlation with $r = 0.231$, n =69 at 95 % confidence intervals. Pearson's correlation test showed no correlation between MD and cellularity metrics.

In the diffusion modelling of lymph node tissue, the single-component models (ADC and DTI) were ranked the lowest by AIC in all lymph node tissue samples. Three multi-component models, which consist of anisotropic and restricted diffusion (Zeppelin-sphere, Ball-stick-sphere, and Ball-sphere) were ranked highest in the majority of voxels of the tissue samples. The multi-component models that included anisotropic components ranked higher than isotropic models. Multi-component models that account for diffusion restriction ranked higher than unrestricted models. These findings are consistent with those from a recent ex vivo study of prostate (4) and lymph node tissue (5).

Conclusion

Investigation of the biophysical basis of contrast in DWI of the lymph node demonstrated distinct diffusion differences between lymph node sub-structures with no correlation to cellularity. Multi-biophysical models were ranked highest by AIC in the majority of voxels and found to extract more information from the measurement data than simple single biophysical models (ADC and DTI). These findings represent an important first step in enhancing our understanding of the biophysical basis of diffusion changes in lymph node tissue.

Acknowledgements

First and foremost, praise and thanks to God, the Almighty, for His showers of blessings throughout my candidature that enabled me to complete the research successfully.

Second, I would like to express my deep and sincere gratitude to my research supervisor, Dr Roger Bourne, for giving me the opportunity to conduct research and providing invaluable guidance. His critiques, consistent support, attention to detail and patience helped me through this rewarding and challenging PhD journey. I am grateful for your patience and dedication throughout the research and writing processes.

I would like to acknowledge my sponsors, Ministry of Education Malaysia and Universiti Teknologi Malaysia, for their financial support. I am also thankful to my associate supervisor, Dr Mark McEntee for his encouragement. I would like to thank numerous collaborators, without whose support and guidance my study would not have been possible. These are: Dr Laurence Gluch from the Strathfield Breast Centre, Dr Kevin Tay from Westmead Breast Cancer Institute, Dr Julia Fletcher from Concord Repatriation General Hospital, Dr David Taylor from Vetnostics and Dr. Mark Krockenberger from Faculty of Veterinary Science, University of Sydney who provided samples; Dr Gary Cowin and Dr Nyoman Kurniawan from the Centre for Advanced Imaging, University of Queensland who performed ex vivo imaging on 16.4T MRI; Dr Andre Bongers from University of New South Wales who performed ex vivo imaging on 9.4T MRI system; I would like to thank Dr. Carl Power from the University of New South Wales for sectioning the samples. Dr Geoffrey Watson from the Tissue Pathology and Diagnostic Oncology, Royal Alfred Hospital who shared his vast knowledge of lymph node histology; Dr. Sisi Liang from Victoria University, Melbourne who fitted and ranked the diffusion models; Dr Cherry Russell, who kindly assisted by proofreading this thesis.

My sincere thanks to my PhD colleagues at the Sydney Diffusion MRI Group: Narina Norddin, Aritrick Chatterjee, Ned Charles for their constant support and encouragement.

Heartfelt thanks go to my family. Words cannot express how grateful I am to my mother, Rosnah Samsudin, my late father, Sahalan Jamsari , my mother-in-law Norliza Hashim and my father-in law Ismail Abdul Aziz for their constant support and prayers for me. Most

importantly, I am profoundly grateful to my loving and supportive husband, Mohd Izraq Ismail and my three wonderful children, Muhammad Khalif, Muhammad Zaeem and Muhammad Zafran, who provide unending inspiration that have been my pillar of strength through this amazing PhD journey.

Mariaulpa Sahalan

Faculty of Health Sciences,

The University of Sydney

25 July 2018

Table of Contents

List of Tables

List of Figures

List of Abbreviations

ADC	Apparent Diffusion Coefficient
AIC	Akaike Information Criterion
ALND	Axillary Lymph Node Dissection
CT	Computed Tomography
DCE	Dynamic Contrast Enhanced
DDC	Distributed Diffusion Coefficient
DLBCL	Diffuse Large B-Cell Lymphoma
DTI	Diffusion Tensor Imaging
DWI	Diffusion Weighted Imaging
DWIBS	Diffusion-Weighted With Whole Body Suppression
ECS	Extracellular Spaces
EPI	Echo Planer Imaging
FA	Fractional anisotropy
FDG-PET	Fluoro-deoxyglucose positron emission tomography
FSE	Fast Spin Echo
H&E	Hematoxylin and Eosin
ICS	Intracellular Spaces
ITC	Isolated Tumour Cell
IVIM	Intravoxel Incoherent Motion
LF	Lymphoid Follicles
MD	Mean diffusivity
MRI	Magnetic Resonance Imaging
PBS	Phosphate-Buffered Saline

PGSE	Pulse Gradient Spin echo
PNG	Portable Network Graphics
SLNB	Sentinel Lymph Node Biopsy
SVS	ScanScope Virtual Slide
TNM	Tumour-Nodal-Metastasis
T1W	T1 weighted
T2W	T2 weighted
USPIO	Ultrasmall Superparamagnetic Iron Oxide
VERDICT	Vascular, Extracellular and Restricted Diffusion for Cytometry in Tumours

1. Introduction

MRI has long been recognised as an important clinical diagnostic tool in cancer assessment because of its excellent contrast ability for distinguishing soft tissues. Diffusion-weighted MRI (hereafter DWI) is a protocol in MRI that has shown potential in the detection and characterization of cancer. In DWI imaging, diffusion of water molecules were used to generate contrast in MR images. One of the most well-established and main clinical applications of DWI is in neuronal diseases, where DWI has shown high sensitivity in both detection and characterization of neuronal diseases (6,7). DWI is also found to be important for detection and discrimination of non-neurological diseases for example cancer imaging associated with the prostate (8,9) , breast (2,10), liver (11,12), and renal (13,14), but it has had limited application in assessing lymph node diseases (15,16).

One of the main causes of death among cancer patients is the spread of cancer cells to surrounding tissues. The earliest stage of this process occurs within the regional lymph nodes (17). There is a potential role for DWI in detection and characterization of lymph node involvement in the diagnosis of cancer patients. This chapter briefly describes the anatomy and physiology of the lymph node and elaborates on nodal disease, nodal imaging, and the basic theory of DWI.

1.1 Cancer and Lymph Nodes

Cancer is a major health concern around the world. One in every four deaths in the United States is reportedly caused by cancer. According to the American Cancer Society, prostate cancer and breast cancer are the two most common cancers among both men and women in the United States. In 2018, an estimated 3,735,350 new cancer cases were diagnosed and resulted in a total of 609,640 cases of cancer-related deaths (18). The aetiology of cancer is complex, however several factors include use of tobacco, overweight or obesity, and lack of physical activity were identified may increase the risk of developing cancer(19). Lifestyle was found to account for about $134,000$ cases or more than 40 % of cancers in the UK in 2010 (20). The Australian Institute of Health and Welfare (AIHW) has suggested that the increase observed in the absolute number of cancer cases in Australia is partly associated with the growth of the ageing population (21). Genetic factors have also been found to be a risk factor for cancer in later years (22).

One of the main causes of cancer-related death is the spread of cancer cells, or metastasis to the surrounding tissues in the body (23). As they spread, the cancer cells disturb the surrounding cells and eventually prevent the tissues from functioning normally. Metastases from a solid tumour account for 90% of cancer-related deaths (24).

Although the spread of cancer cells to the lymph nodes is not well understood, distinct organ-specific patterns of metastasis have been reported in different types of cancer (17,23,25,26). The spread of cancer cells to the regional lymph nodes is one of the earliest events in the metastatic process, and the enlargement of the lymph node is a common feature of many solid tumours (17,26). The cancer cells from the primary tumour may spread to the nearby tissue through both blood and lymphatic vessels. In this context, the lymphatic vessel may actively promote the spread of cancer cells to other tissue (23).

Patients with node-positive cancer (i.e., cancer detected in the lymph nodes) are almost five times more likely to develop regional and distant cancer recurrence than those with no nodal involvement (27). The five-year survival rate also decreases from 90 % to less than 40 % for patients with node-positive cancer compared to those with no nodal involvement (28,29). In other words, the survival rates appear to decline for cancer patients with positive nodes. The higher likelihood of cancer spreading to the nodes points to the significance of including nodal assessment in the course of diagnosing cancer patients.

In summary, since cancer has high potential to spread to the node and eventually result in death, there is an urgent need to include nodal assessment at an early stage in cancer management. By providing comprehensive treatment to control or reduce the likelihood of cancer metastasis, patients could potentially experience a higher survival rate.

Anatomy of the human lymph node

The lymph node is the major organ within the lymphatic system. It plays a vital role in protecting the human body from harmful foreign agents. The normal lymph node is ovoid or bean-shaped, ranging in size from 2 to 20 mm in length and 3 to 15 mm in diameter (30-32). Lymph nodes are usually clustered in small groups and chained at various locations throughout the lymph vessels (Figure 1.1). Each cluster contains a minimum of three lymph nodes. The lymph nodes contain denser numbers of B- and T-lymphocytes. The lymphocytes serve as the primary site for immune system interactions between the body's host cells and foreign elements such as bacteria, viruses, antigens, and toxins.

The lymph node is surrounded by white adipose tissue. The main components of a node are stroma and parenchyma. The stroma consists of a dense layer of connective tissue that forms a mesh-type network in the capsule of the node. The parenchyma is divided into two regions, the cortex and the medulla. Within the cortex region, follicles are peripherally distributed, evenly spaced and variable in size, and indicate the activation of normal lymph nodes to varying degrees. The follicles in the cortex are the primary site of production of B- and T-lymphocytes (30-33).

Although the nodes are small, reactive and enlarged nodes that are close to the skin surface are occasionally palpable. Reactive and enlarged nodes are usually the result of intense immune response or tumour metastasis. Palpable lymph nodes are more likely to be due to infection from viruses such as the common flu than to tumour metastasis. In many cases, tumour metastasis to the nodes is not palpable as these nodes lie deep inside the human body.

Diagnosis of nodal metastasis often requires clinical imaging to localise the node's exact position within the body. Additionally, a more rigorous clinical assessment, such as biopsy and microscopic viewing of the tissue, is required to accurately determine the nodal pathological condition. Haematoxylin and Eosin (H&E) is used to stain a thin (5 µm) slice of nodal tissue. Haematoxylin stains the nucleus in dark blue or violet, while eosin stains the cytoplasm and stroma in light red or dull pink. H&E stained slides are normally used to study lymph node microstructure. Any microstructural changes are carefully viewed under a microscope to determine the pathological status of the nodal tissue.

The involvement of metastatic disease in lymph nodes often indicates cancer progression. It shows that, through a succession of molecular changes, the cancer cells have the ability to invade, colonise, and disseminate into nodal organs. Although a range of diseases have been found in nodal tissue, only three pathological conditions of nodes are considered in the present study: lymphoma, metastatic, and normal nodes. The pathological conditions of the lymph node are briefly discussed in the following sections.
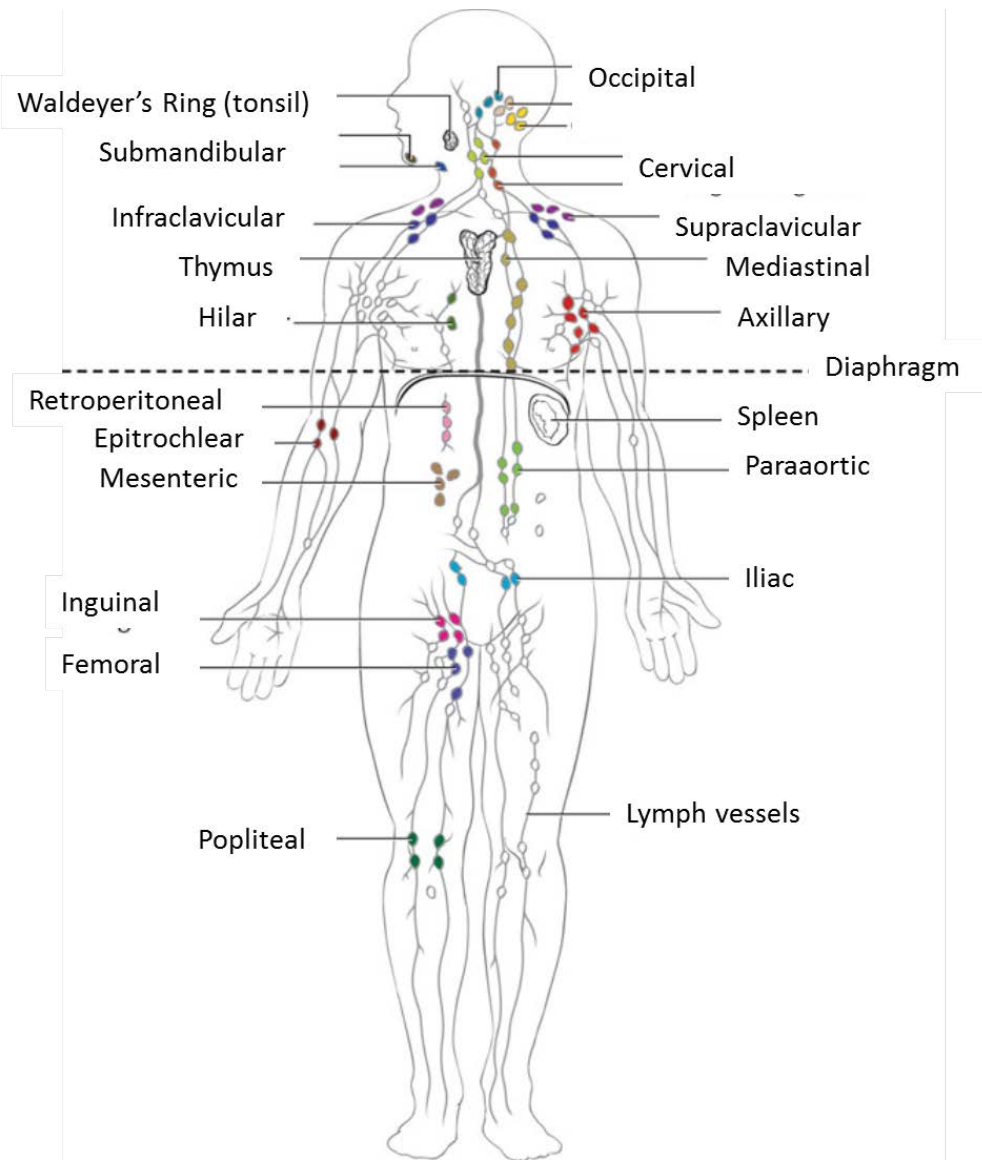
Figure 1.1 Distribution of lymph nodes in the human lymphatic system

Location of major regional lymph nodes in the lymphatic system of women: axillary node, cervical node, mesenteric node, iliac node, inguinal node (reproduced with permission from (34), Springer, London).

1.2 Lymph Node Histology

The lymphocytes dominate the histological appearance of lymph nodes and obscure the stromal supportive framework. Under microscopic viewing, the lymphocytes appear dense and structureless and the cytoplasm is just a thin, perinuclear rim (Figure 1.2).
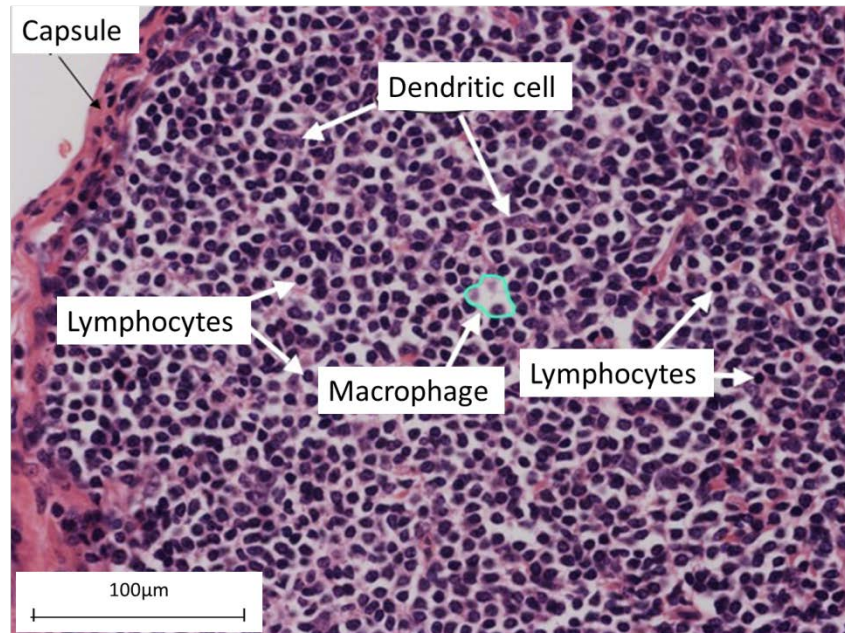
Figure 1.2 Morphology of healthy node tissue

The morphology of healthy node tissue shows densely-packed lymphocytes, sparse distribution of dendritic cell and macrophages in parenchyma of the lymphatic nodule. Image from this study.

The differentiation between metastatic carcinoma, lymphoma, and reactive lymphadenopathy in histology is possible because each nodal disease has distinct cytologic features. More importantly, the histologic features in metastatic carcinoma are more consistent than in lymphoma tissue. In cancerous nodal tissue, the tumour cells are present in a nested island with evidence of cords either inside or outside the parenchyma. The histologic appearance of nodal metastasis often points to the presence of a primary tumour (17,23,25,26). Nodal metastatis in adenocarcinomas often appears as a small gland cluster, such as in invasive prostate and ductal mammary carcinoma. Particularly in invasive lobular mammary carcinoma, a signet ring pattern can often be seen in the nodes. A distinctive histologic feature has also been observed in lymphoma, where the parenchyma shows a monotonous

population of lymphoid cells, as shown in Figure 1.3. In some cases, nodal disease shows distinct histology criteria and can be used as a final measure for disease identification (31,35).
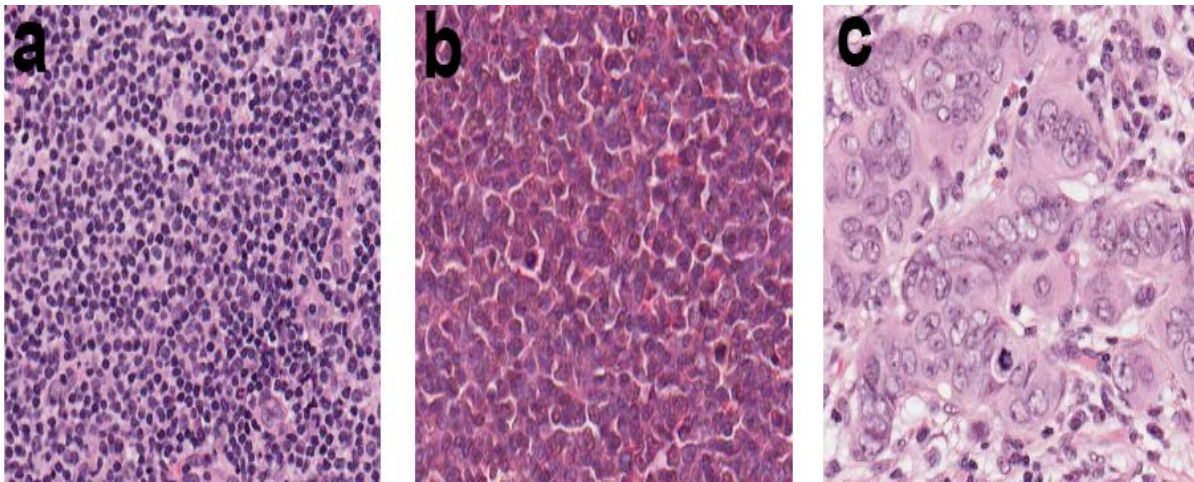
Figure 1.3 Lymph node histology and pathology

Histology of lymph node tissue in three different tissue types: (a) normal, (b) lymphoma, and (c) metastatic cases. Classification of cancer is based on variations observed in nuclear architecture. Images from this study.

1.3 Route of Node Metastasis

An overview of the major route of cancer metastasis can provide a better understanding of the unique challenge faced in clinical nodal assessment. Cancer dissemination starts when cells gain entry into nodes through afferent lymphatic vessels (32,36). The initial metastasis commonly appears in the subcapsular sinus of the lymph node tissue. The cancerous cells then invade and cause partial desmoplastic replacement in the supcapsular sinus. Some may cause further invasive extracapsular extension to the adipose tissue layer or parenchyma region of the lymph node tissue. From the sinus, the malignant cells may travel to the medullary sinus and the parenchyma of the nodes.

In this context, the malignant cells may invade either as isolated tumour cells or as a group of nested malignant cells in the parenchyma region. In the case of an intense desmoplasia, the neoplasm replaces most of the lymph node microstructure and a small island of residual normal lymphocytes is found in between the tumour masses (Figure 1.4). Often a reactive lymph node occurs as a response to metastasis, for example in follicular hyperplasia

(32,34,36). Follicular hyperplasia is characterised by an increased number of secondary follicles. The follicles vary in shape and size, ranging from spherical to oval.

In the present study the biophysical basis of contrast in DWI of the lymph node was explored via microstructural changes observed within the parenchyma region only (37). The parenchyma region was particularly well suited for this purpose because it is where the main microcellular interaction takes place in the lymph node tissue. Microstructural changes in the parenchyma region are particularly important in histopathology analysis in comparison with the other sub-structures in the node.
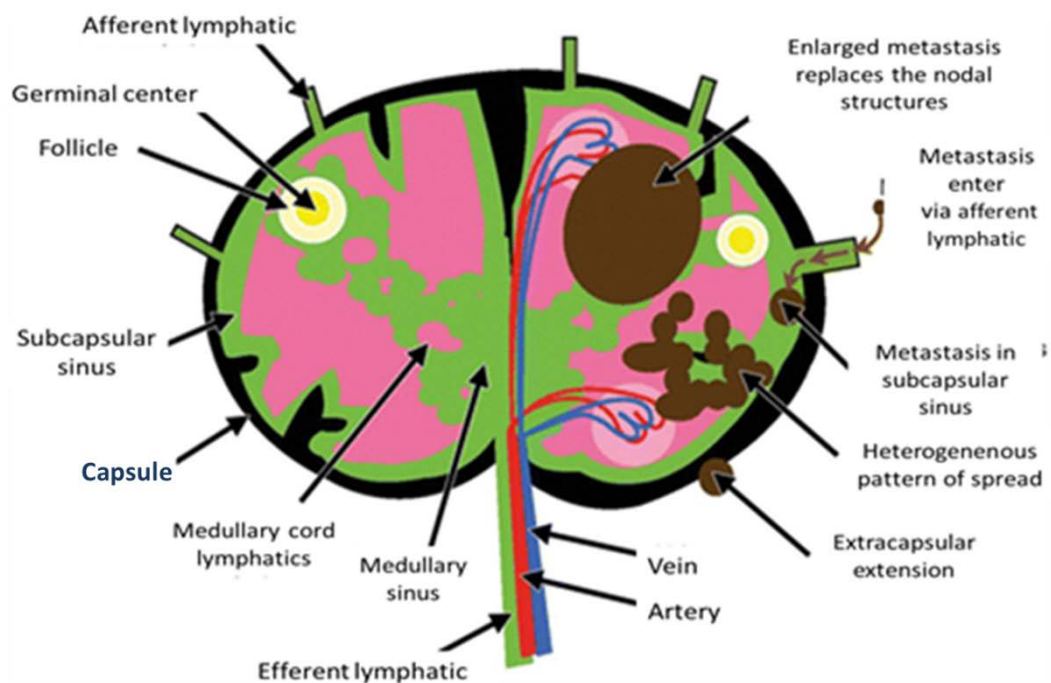
Figure 1.4 Metastasis route in node

Primary locations of nodal metastasis. Metastasis can cause isolated, partial or total replacement of the architectural microstructure of the node. (Reproduced from (36) with permission from Radiographics Inc, North America).

7

1.4 Nodal Staging

The stage of the disease at the time of diagnosis can reflect not only the growth rate but also the extension of the neoplasm in the tissue. Cancer treatment is usually based on the type of cancer and its stage. The most common system used to assign cancer stage is the tumour-nodal-metastasis (TNM) system, which was developed by the Union for International Cancer Control (UICC) and the American Joint Committee on Cancer (AJCC)(38).

The TNM classification is based on the extent of the primary tumor (T), the spread of cancer to the regional lymph nodes (N), and the presence of metastasis (M) to distant nodes. It is used to define the severity and progression of cancer in patients. If no cancer cells are found in the lymph nodes, N is assigned a value of 0. If cancer cells are found in nearby or distant nodes, N is assigned a number (1, 2 or 3) in line with the progression pattern. Cancer with lower TNM numbers is usually considered easier to treat, therefore having better survival chances. For example, T1N0M0 would be cancer found at an early stage before it has spread. T1 means a small tumor; N0 means no node involved, and M0 means no metastasis is present (38).

The letters and numbers allocated to TNM stages are unique to different types of cancer, as each disease has distinct morphological characteristics. TNM staging for the digestive system is based on the number of regional lymph nodes containing metastases (i.e., positive nodes). In classifying N, the number of positive nodes is grouped into 0, 1–2, 3–6, and 7 or more, as shown in Figure 1.5. In contrast, for the breast region, the TNM staging is based on the presence of isolated tumour cell (ITC) clusters in the nodes. This refers to the presence of small clusters of cells not greater than 0.2 mm, or cells not exceeding 200 cells in a single histologic lymph node cross section, as shown in Figure 1.6(38).
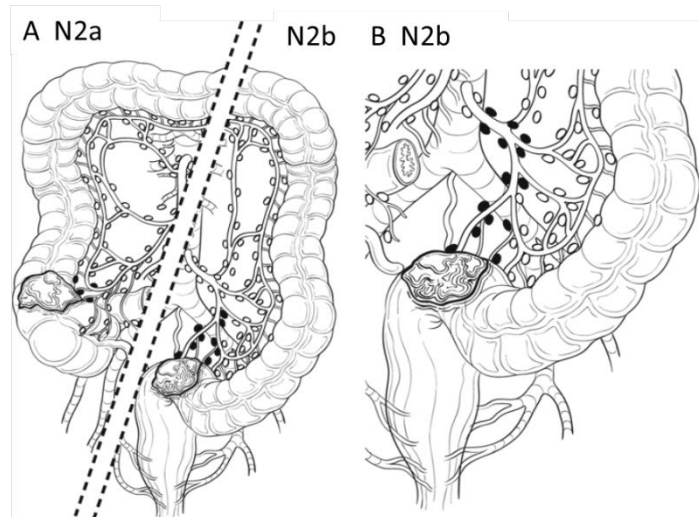
Figure 1.5 TNM staging for the digestive system in the large intestine

TNM staging for mesenteric cancer is indicated by the number of nodes affected by cancer (black coloured node). For example, if cancerous cells are found in 4 to 6 lymph nodes, the TNM stage is N2a. If 7 or more lymph nodes are found to be cancerous, the stage is N2b. (Reproduced with permission from (34) Springer, London).
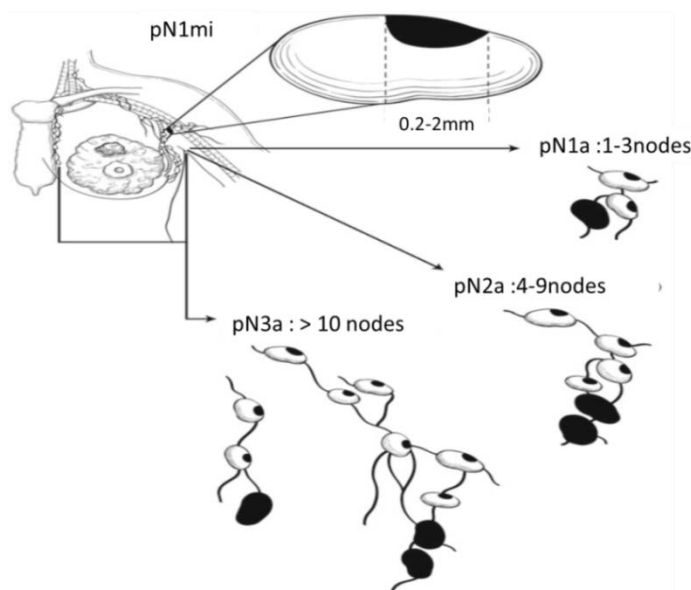
Figure 1.6 TNM staging for breast cancer

The TNM staging for breast cancer depends on the number of nodes affected by cancer cells and the presence of isolated tumour cells (ITC). If metastases occur in 1-3 axillary lymph nodes, the stage is pN1a. If metastases occur in 4-9 axillary lymph nodes, the stage is pN2a. If metastases occur in ten or more axillary lymph nodes, the stage is pN3a. (Reproduced with permission from [10] , Springer, London).

In clinical practice, the TNM staging is commonly determined based on measurement of the nodal size. However, related studies have consistently reported that measurement of the nodal size is often an inaccurate and unreliable method of determining nodal disease (39-41). Although histology sectioning is regarded as the gold standard, microscopic identification of pathological disease in the node remains a challenge (34). Clinical imaging has shown potential in not only detecting nodal diseases but also distinguishing between normal and cancerous nodal tissue (42). In the following sections, the advantages and disadvantages of clinical imaging and histology sectioning methods are discussed.

1.5 Clinical Screening and Diagnosis of Nodal Disease

A wide range of approaches — invasive, non-invasive, or a combination of both — is available to assist clinical assessment of nodal disease. Imaging prior to invasive approaches can help to identify the exact location of nodes and improve diagnostic accuracy.

Conventionally, two types of invasive procedures are used to assess nodal status: sentinel lymph node biopsy (SLNB), and axillary lymph node dissection (ALND). An invasive procedure involves surgical removal of the nodal tissue. The tissue is then sent to a histology lab to determine its histopathological condition. The histopathological assessment requires the tissue samples to be sectioned into 5 µm thickness and then viewed under a microscope. Microstructural changes, such as the presence of neoplasia and reactive lymph nodes, are the main criteria used by the histopathologist to determine the pathological condition of the tissue.

The sentinel nodes are the first few lymph nodes into which the tumour cells will drain from the primary tumour. It is therefore hypothesised that the sentinel lymph node is the primary target organ of the cancer cells metastasising from the tumour. SLNB was developed as an alternative procedure to the traditional ALND (34). Axillary dissection, which involves extracting a group of lymph nodes, requires hospitalisation, general anaesthetic and one to two weeks of postoperative care. The SLNB procedure on the other hand involves taking one or two targeted lymph nodes and does not require hospitalisation or general anaesthetic, although it can be time-consuming to identify the exact location of the lymph nodes. SLNB is capable of replacing ALND since more than 70% of patients with no positive nodes (N0) undergoing ALND are found to be free from metastatic disease (43).

The accuracy of SLNB is, however, limited. False negative results can occur if the wrong node is removed and nodes containing metastases remain unrecognised. False negatives can also be due to sampling errors on the part of pathologists and inexperienced surgeons, which may in turn result in blockage or alteration of the normal flow of the lymph [22]. A related study has shown that sentinel node biopsy following injection of the radiotracer Technetium-99m had nearly 98% accuracy in predicting the lymph node's status in 160 patients (44). In contrast, another study reported lower values for sensitivity, specificity and accuracy of SLNB (92%, 88%, and 91% respectively), compared to ALND using Technetium-99m (45). This suggests that SLNB might be insufficient to evaluate lymph node metastases. SLNB has also demonstrated low sensitivity in differentiating macrometastases and micrometastases of lymph nodes in breast carcinoma, with 88% and 72%, respectively (46). The effectiveness of lymph node dissection and biopsy, however, remains controversial due to the morbidity associated with the surgical procedures involved and poor imaging assessment prior to surgery. Therefore, a reliable and accurate imaging assessment of the lymph nodes before a surgical procedure is considered essential (47).

Improved sensitivity and specificity in imaging has potential to replace invasive nodal assessment of cancer patients. Magnetic resonance imaging (MRI), for instance, is valuable for identification of nodal diseases as it is considered a safe and reliable method of soft tissue assessment and avoids the morbidity effects of the surgical approaches.

1.6 Role of Imaging in Lymph Node Assessment

Although histopathological analysis remains the gold standard for diagnosing lymph node invasion, the accuracy of this approach has been questioned, as noted above. Therefore, several imaging modalities have been investigated as an alternative. Computed tomography (CT) enables the assessment of small internal body organs and structures, including the lymph node. However, CT has limited applications in nodal cancer imaging due to its low sensitivity and poor contrast resolution for soft tissue (42). Fluoro-deoxyglucose positron emission tomography (FDG-PET), which has the ability to show cancerous regions as areas with increased glucose uptake, is also used. FDG uptake can be non-specific since most of the cell types in the body, other than the tumour cells, actively use glucose. FDG also accumulates in the bladder and may obscure the detection of lymph nodes in the pelvic area (42).

MRI has become a powerful, widely used tool for non-invasive clinical diagnosis owing to its fair spatial resolution (at lower field strength), higher degree of soft tissue contrastand depth of penetration. The evaluation of nodal status by means of traditional MRI techniques has concentrated mainly on assessment of nodal anatomicalfeatures. Unfortunately, these physical features have not been able to reliably distinguish benign from metastatic nodes, even at high spatial resolution imaging (39,48,49).

MRI has the ability to provide images with excellent anatomical detail and soft tissue contrast but it is currently relatively insensitive for detection of lymph node diseases. Accordingly, a range of techniques has been developed in MRI to improve its sensitivity and specificity in relation to nodal disease assessment. These include the introduction of dynamic contrast-enhanced MRI (DCE), the development of a MR contrast agent known as ultrasmall superparamagnetic iron oxide (USPIO), and the development of DWI. The advantages and limitations of each technique are discussed below.

Dynamic contrast-enhanced MRI (DCE-MRI)

Dynamic contrast-enhanced MRI is an imaging technique that requires multiple T2 or T1 weighted images before and after injection of the contrast agent. The most commonly used contrast agents are based on gadolium and most of the contrast agents are paramagnetic (or super-paramagnetic, or ferromagnetic); as a result they shorten both T1 and T2 of water protons, which in turn would result in negative contrast on T2-weighted images. (50,51). The presence of a contrast agent within blood vessels and tissues affects the signal intensity of MRI. The physiologic state of tumor vascularity can be assessed in the images as a result of distinct contrast enhancement of malignant and normal tissue that gradually decreases over time (52). At present, DCE-MRI is widely used to distinguish primary benign from malignant tissue but has limited application in evaluating secondary disease in the lymph nodes (53,54).

Both suspicious and non-specific enhancement of lymph nodes can lead to misleading interpretations as a result of the higher sensitivity and lower specificity of DCE-MRI compared with conventional MRI (41). A homogeneous signal intensity was found in both normal and malignant lymphoma. This makes it more challenging to determine the pathology of nodes based on contrast enhancement (55). Furthermore, DCE-MRI has not been shown to be superior to T1W or T2W in detecting malignancy in nodes (54,56).

Ultrasmall superparamagnetic iron oxide (USPIO)

Another advance in MR imaging is the development of a MR contrast known as ultrasmall superparamagnetic iron oxide (USPIO), which major potential application in imaging lymphatic system, bone marrow, brain, heart and other organ-targeted imaging(57). Improved detection of lymph node metastases with USPIO-enhanced MR imaging was reported in both clinical applications (58-60) and preclinical studies on animals (61) allows the identification of malignant nodal infiltration independent of lymph node size. However, there continues to be an overlap between benign and malignant lesions, and the specificity of T2 weighted images collected before and 24 hours after the contrast injection continues to be low, ranging from 67% to 72%. Another limitation is that USPIO has not yet been clinically approved for human beings. Hence there is need for a diagnostic imaging that offers similar or higher sensitivity and specificity than contrast-enhanced MRI. DWI has produced promising results in assessing both primary and secondary cancer and is a potential tool for assessing nodal disease, as it shows similar tissue contrast accuracy to DCE (62).

Diffusion and multiparametric MRI

The recently introduced "diffusion-weighted with whole body suppression" technique (DWIBS) has the potential to improve the detection of malignancy in lymph nodes (63). DWIBS uses a grayscale inverted reformatted image reconstruction to identify and visualise any pathological abnormalities in the tissue (64,65).

A multiparametric in vivo imaging combining T2W with DWI and DCE on prostate cancer appears to indicate a relatively higher accuracy in combination of T2W with DWI compared to DCE-(66). Another study of multiparametric imaging on the prostate also shows that DWI had the highest sensitivity for tumour localisation (31.1 % vs. 27.4 % vs. 44.5 % for T2W, DCE and DWI, respectively; $p < .05$), with more aggressive or more advanced tumours being more easily detected with this imaging modality (67). Until recently, no multiparametric imaging had been carried out on node tissue. The investigation of multiparametric studies on nodal tissue can help to determine which method (T2W/DCE/DWI) yields optimum nodal tissue contrast. The following section elaborates on DWI as the emerging MR imaging technique that has shown potential in detection and characterisation of lymph node diseases.

1.7 Basic Diffusion-weighted Imaging (DWI)

As previously noted, the current gold standard in clinical techniques for nodal disease assessment require invasive tissue sampling. Non-invasive techniques such as DWI have potential not only in cancer detection but also in providing additional information on microstructural changes that can be used to better predict disease progression. These advantages can help clinicians to optimise treatment planning and monitor treatment responses in cancer patients.

Diffusion MRI is sensitive to the random motion of water molecules in the tissue. Cancer is broadly characterised by changes in tissue microstructure. Therefore, any microstructural changes that occur in cancer, and which eventually affect the motion of water molecules, can potentially be detected and characterised by DWI.

In the absence of obstacles, a water molecule can move freely in a given space. The motion of freely diffusing water molecules is referred to as free diffusion or self-diffusion, in which molecular displacement follows a Gaussian distribution. The mean squared displacement $<r^2>$ of the freely diffusing water molecules over a specified time is defined in the equation:

$$< r^2 > = 6Dt$$

[1.1]

where D is the diffusion coefficient and t is the time interval. The SI unit for the diffusion coefficient is m/s, instead that the values of D are usually given in mm^2/s (68,69). The diffusion coefficient of freely diffusing water molecules is temperature dependent. At a temperature of 20^0C the diffusion coefficient is approximately 2×10^{-3} mm^2/s was measured in bulk water, which represents a mean displacement of about 25 µm in a diffusion time of 50 ms (69). At a body temperature of 37^0C the diffusion coefficient is 3×10^{-3} mm^2/s (68,70),with a mean displacement range of 17-25 µm over the typical diffusion time range of 50-100 ms used in clinical DWI (68).

1.7.1 Restricted and hindered diffusion

Diffusion properties observed in bulk water are more straightforward than the diffusion properties in tissue. Water diffusivity in tissue is influenced by the presence of cell membranes, macromolecules, and other cell microstructures that cause restricted and hindered diffusion.

Restricted diffusion refers to the trapping of water molecules inside a closed compartment. The freely-diffusing molecules experience restricted diffusion when they interact with the boundaries of cell membranes. The effects of restricted diffusion on freely diffusing molecules are highly dependent on the shape of the restricting volume (eg., spherical, cylindrical or parallel walls) (71). There is no single equation that can describe all possible configurations of diffusion in water (72).

Hindered diffusion is a term used to describe the delay in the passage of water molecules that results from the presence of obstacles. In contrast to restricted diffusion, water molecules in hindered diffusion are able to diffuse over a long distance, although more slowly than they would in the absence of hindering structures. Therefore, the mean diffusion distance remains linear with the square root of diffusion time but the diffusion coefficient is reduced.

1.7.2 Apparent diffusion coefficient (ADC)

The typical diffusion coefficient of water measured in in-vivo experiments falls within the range 2-3 $\times$ 10^{-3} mm^2/s (69). The observed diffusion coefficients of water in tissue are relatively lower than the typical free water diffusion due to restricted and hindered diffusion. Diffusion coefficients value may be affected by processes other than brownian motion typical for free diffusion (e.g. slow capillary flow and other types of molecular incoherent motion), thereforecan be described simply as an 'apparent' diffusion coefficient (ADC). The ADC is calculated from two or more images with different diffusion weightings or b-values (68,70). Specifically, the ADC can be calculated as:

$$ADC = \frac{\ln\ (\ S_1/S_0\ )}{b_1 - b_0}$$
[1.2]

where S_1 is the signal intensity at b_1, and S_0 is the signal intensity at b_0, and b_1 and b_0 are the diffusion weighting values. S_0 is usually the non-diffusion weighted signal, although for cancer the consensus is to use a b_0 larger than 100 to avoid perfusion effects (73). Typical b-

values used for in-vivo imaging are within the range of 50 to 1000 s/mm^2. However, for ex vivo imaging, the *b*-values can be extended to 5000 s/mm^2 or higher (74). *b*-values are expressed as:

$$b = (\gamma \cdot \mathrm{g_D} \cdot \delta)^2 \cdot (\Delta - \delta /3)$$ [1.3]

where γ is the nuclear gyromagnetic ratio, $\mathrm{g_D}$ is gradient amplitude, δ is gradient duration, and Δ is the interval between the onset of two consecutive gradient pulses. It should be noted that the *b*-values equation above is true for specific pulse sequence. The complex interactions identified between water and tissue microstructures leading to the observed ADC are not completely understood. However, various studies report that cellularity, extracellular volume fraction (ECVF) (75), membrane permeability (76), and tortuosity (77) play an important role in determining diffusion behaviour in tissue (68).

A single ADC is insufficient to characterise the diffusion process in anisotropic tissue at the voxel scale. This is because ADC does not account for differences in water mobility in different spatial directions. A variant of DWI known as diffusion tensor imaging (DTI) is used instead of ADC to obtain information on diffusion in different spatial directions. Measurement in DTI requires a minimum of six distinct diffusion directions. Here, the ADC is replaced by a symmetric 3×3 matrix (69,70).

$$D = \begin{bmatrix} D_{xx} & D_{xy} & D_{xz} \\ D_{yx} & D_{yy} & D_{yz} \\ D_{zy} & D_{zy} & D_{zz} \end{bmatrix}$$ [1.4]

where,

$$D_{xy} = D_{yx} , \ D_{yz} = D_{zy} , \ D_{xz} = D_{zx}$$

The diffusion tensor has six independent variables that are described by eigenvalues and eigenvectors which characterise the magnitude and direction of 3D diffusion in a voxel. Of all the diffusion metrics derived from the tensor, mean diffusivity (MD) is the most frequently used parameter forcancer imaging studies . MD is an average of eigenvalues, λ . MD is comparable to ADC in DWI. Instead of ADC values, mean diffusivity values were used in this study because this has the advantage of averaging the diffusivity measurement over six gradient directions.

$$MD = (\lambda_1 + \lambda_2 + \lambda_3)/3 \qquad [1.5]$$

Multiple independent diffusion measurements are obtained by applying diffusion encoding gradients in a different spatial direction (69,70).

Anisotropic diffusion

Anisotropy is a measure of how much diffusion deviates from being isotropic. In anisotropic diffusion, the diffusion coefficient is not the same in all directions. The presence of obstacles and structure geometry can contribute to diffusion anisotropy. Fractional anisotropy (FA) is the most frequently used parameter derived from the distribution of eigenvalues to characterise the presence of a preferred diffusion direction (68,70,78). FA describes the variation of diffusion over measurement directions and characterises the shape of the diffusion ellipsoid:

$$FA = \sqrt{\frac{3}{2}} \frac{\sqrt{(\lambda_1 - \bar{\lambda})^2 + (\lambda_2 - \bar{\lambda})^2 + (\lambda_3 - \bar{\lambda})^2}}{\sqrt{\lambda_1{}^2 + \lambda_2{}^2 + \lambda_3{}^2}} \qquad [1.6]$$

FA values range from 0 for isotropic diffusion to 1 for completely anisotropic diffusion (68-70). A highly anisotropic human tissue, white matter in the brain, for example has a FA value of between 0.7 to 0.8 (69,70).

1.8 Image Acquisition in DWI

The pulsed gradient spin echo (PGSE) MRI sequence developed by Stejskal and Tanner in 1965 is commonly used in image acquisition for DWI because of its sensitivity to molecular motion (79). Specifically, a diffusion-weighted pulse sequence was constructed by adding a pair of diffusion-sensitising gradients, also known as motion-probing gradients, to a T2 weighted spin echo sequence. Molecular motion results in a loss of signal intensity due to an incomplete rephasing of water proton spins which are capable of changing positions between and during the application of the two diffusion sensitising gradients. The three most common types of spin echo acquisition used for DWI are basic PGSE, fast spin echo (FSE), and echo planar imaging (EPI). FSE and EPI are used as read-out part of the sequence. FSE is also rather rarely used for imaging diffusion; EPI is by far most common for in vivo applications, whereas the spin-echo is often used for ex vivo applications due to its long acquisition time.

The advantages and limitations of each diffusion sensitive spin echo method are described in this sub-section (68,80).
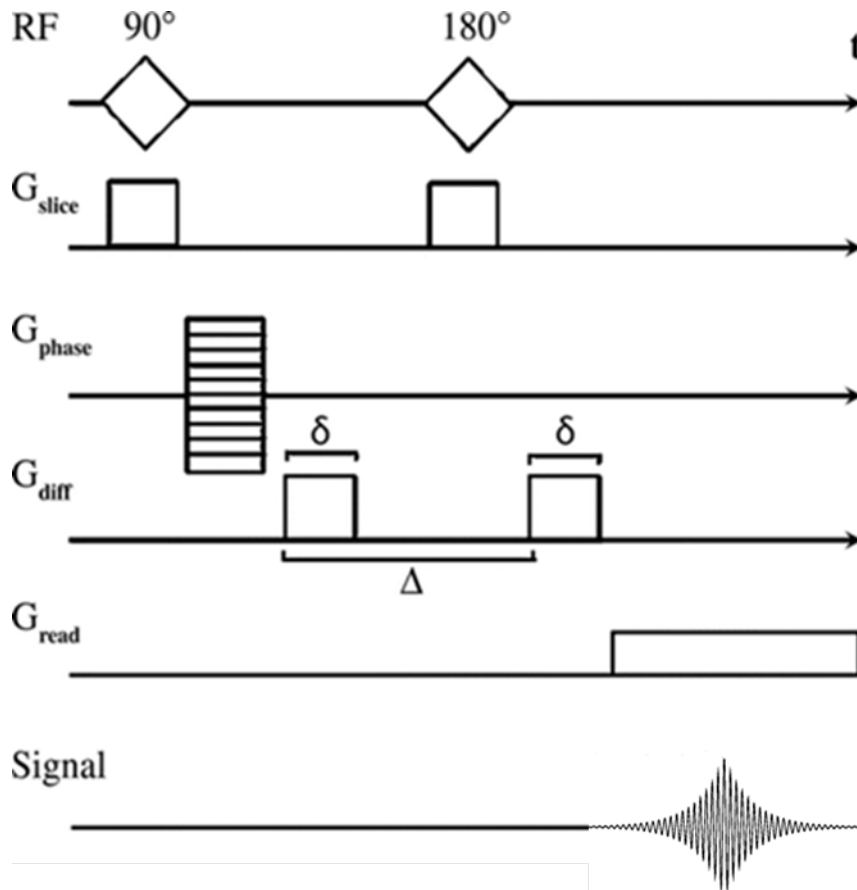
Figure 1.7 Pulsed gradient spin echo (PGSE) sequence used for diffusion MR imaging

Two diffusion-encoding gradient (G_{diff}) pulses are added to the standard spin echo sequence of MR imaging in order to introduce a phase shift. Phase shift is a change in the phase of a waveform. The phase shift in diffusing spin is proportional to molecular displacement along the gradient direction. δ = duration of the diffusion-encoding gradient, Δ =interval between the onset of the diffusion gradients , G_{phase} = phase-encoding gradient, G_{slice} = section-selective gradient, G_{read} = readout gradient, RF = radiofrequency pulse, t = acquisition time. (Reproduced with permission from (81)with permission from RadioGraphics, USA).

The standard PGSE is the most straightforward implementation of the pulse sequence in acquisitioning MR data. In this pulsed gradient sequence, two gradient pulses are applied. An excitation pulse, typically of 90^0, is applied, followed by the first diffusion weighting gradient. Next, the 180^0 RF refocusing pulse is applied, followed by the second diffusion weighting gradient, as shown in Figure 1.7. A gradient magnetic field in a magnetic spin echo experiment cause a signal attenuation due to the molecular diffusion to the spins. The diffusion gradient (G_{diff}) pulse cause a spatially varying additional magnetic field, and thus spatially varying Larmor frequencies. The first diffusion at 90^0 pulse gradient dephase the spins. If the spin are stationary (no diffusion), the second diffusion gradient at 180^0 RF refocusing pulse in opposite sign exactly rephrase the spins. In the case of diffusion spins, however , rephrasing is incomplete since the spins have moved between the first and second diffusion gradient; thus , a diffusion –dependent signal attenuation is iobserved as "vector sum"(69). In the standard PGSE, each line in k-space is acquired in a different repetition which requires longer data acquisition for the whole k-space and are prone to motion artifacts.. PGSE is especially suitable for preclinical imaging applications and animal studies, where the subjects can be immobilised for extended time scanning (68,81).

Another pulse sequence used in diffusion MRI is the fast spin echo (FSE) method. This is a modified version of the traditional spin echo sequence that allows significantly faster scan times with less sensitivity to subject motion. A single RF excitation pulse is introduced, followed by a series of RF refocusing pulses that produces one spin echo per each refocusing pulse. qqqqqq The possible disadvantages of FSE are blurring effect, edge enhancement and ghosting effect. It should be noted that a significant amount of RF power might need to be delivered to the patient in order to activate the multiple refocusing RF (68).

Echo planar imaging (EPI) is the most commonly used pulse sequence for acquiring images in DWI. The entire diffusion image is acquired after one RF excitation has been completed. The sequence is designed to acquire the entire k-space but usually with lower number of points, which can significantly reduce the data acquisition time. Although EPI is insensitive to motion, it is prone to severe image artefact and is sensitive to eddy current effects (68,69,78).

1.9 Thesis Structure

Chapter 1 provides the background to the study by describing the anatomy and physiology of the lymph node and explaining nodal disease, nodal imaging, and concepts of DWI.

Chapter 2 presents a comprehensive review of literature on diffusion–weighted MRI in the lymph node and modelling techniques for non-neural tissue. The findings of studies reviewed in this chapter informed the theory and methods of the present study.

Chapter 3 deals with the characterisation of microscopic structures of nodes by means of DWI. The correlation between mean diffusivity (MD) and cellularity metrics of nodal tissue is described.

Chapter 4 presents the results of the study investigating the relative information content of biophysical models, including the combination of isotropic, anisotropic and restricted components in node tissue.

Chapter 5 summarises the research findings, draws conclusions, and offers suggestions for future work in the area.

2. Literature Review

2.1 Diffusion-weighted MRI of Lymph Nodes

DWI was initially used for neurological imaging but has in recent years been increasingly used in non-neurological imaging, including the detection of prostate and breast diseases. Recent reviews have recommended the inclusion of nodal assessment as part of routine primary tumour assessment (73). The application of ex vivo DWI imaging to the detection of solid cancer shows great promise in differentiating cancerous from non-cancerous tissue (2,8,9). Based on these findings, several studies were carried out to assess the performance of in vivo DWI imaging in secondary disease in nodal tissue(15,16,41,48)

The findings from studies using DWI to distinguish nodal diseases have been inconsistent (Table 2.1). Some DWI studies of in-vivo nodal disease have found lower ADC values in metastatic nodes than in benign nodes, indicating reduced water mobility in the cancer tissues (41,82-86). On the other hand, several studies have found relatively higher ADC values in metastatic nodes than in benign nodes, indicating increased water mobility in the cancer tissues(15,16), while a few other studies have found no significant differences in ADC values between malignant and benign nodes (39,48,49). Such inconsistent findings underscore the lack of understanding of the biophysical basis of tissue diffusion contrast in DWI imaging of nodal tissue.

Table 2.1 DWI Studies of Nodal Disease						
Study	**Field strength (T)**	*b* - values (s/mm²)	**Nodal Source**	**Nodal Pathology**	**ADC Mean ± SD (x 10^{-3} mm²/s)**	*p* - value
Sumi et al. (15)	1.5	0, 500, 1000	Head and Neck	Metastatic	0.41±0.11	<0.001
				Lymphoma	0.22±0.06	
				Benign	0.30±0.06	
Kamitani, et al.(16)	1.5	0, 1000	Axillary	Metastatic	1.08±0.18	0.004
				Benign	0.92 ±0.22	
Chung et al. (41)	1.5	0, 1000	Axillary	Metastatic	0.69[a] (0.60–0.80)	<0.001
				Benign	1.04[a] (0.9–1.20)	
Nakai et al. (48)	1.5	0, 800	Pelvic	Metastatic	1.4±0.40	0.28
				Normal	1.3±0.24	
Fornasa et al. (82)	1.5	0, 800	Axillary	Metastatic	0.88[a] (0.30–1.20)	<0.001
				Benign	1.5[a] (0.60–2.50)	
Scaranelo et al. (83)	1.5	50, 300, 700, 1000	Axillary	Benign	0.39-1.50[b]	<0.05
				Malignant	0.33 - 2.843[b]	
Luo et al. (84)	1.5	0, 800	Axillary	Metastatic	0.986±0.17	<0.05
				Benign	1.375±0.147	
Rechichi et al. (85)	1.5	0, 1000	Pelvic	Metastatic	0.87±0.15	0.010
				NonMetastatic	1.07±0.20	
Abdel Razek et al. (86)	1.5	0, 1000	Head and Neck	Metastatic	1.09±0.11	<0.05
				Lymphoma	0.97±0.27	
				Benign	1.64±0.16	
Heijnen et al. (49)	1.5	0, 500, 1000	Rectal	Malignant	1.0±0.22	0.10
				Benign	1.2±0.24	
Roy et al. (39)	1.5	0, 1000	Pelvic	Malignant	0.9±0.2	0.44
				Benign	0.9±0.2	
[a] Study does not include standard deviation						
[b] Study does not show mean ADC and standard deviation						

For the characterisation of nodal diseases in-vivo, DWI relies heavily on measurement of nodal anatomical features that appear on conventional MR images, including T1 and T2 weighted images. The characterisation of nodal diseases based on nodal anatomical features should be interpreted with caution, however, as these may not reflect the diffusion property of the tissue. Related studies report that distinguishing metastatic from normal nodes based on physical features appearing on MR images remains challenging (41,47,51). The measurement of physical features on MR images includes assessment of nodal size, presence of fatty hilum, and the length-width ratio of lymph nodes (53). It has been suggested that irregular contour and cortical thickness provide better physical features from which to identify metastatic nodes (87). Based on the physical feature of nodal size on DWI images, studies have reported up to 60% reduced sensitivity in detection of metastatic nodes(16,48). Therefore, caution needs to be exercised in characterising nodal disease based on physical features appearing on DWI imaging.

The characterisation of nodal diseases in DWI based on measurement of nodal anatomical features has continued to prove challenging. Studies have been conducted to investigate the ability of nodal anatomical features, specifically lymph node size, on DWI images to characterise nodal disease (40,88,89). Two main criteria of lymph node size have been identified: uncertainty of nodal volume and selection of region of interest (ROI). Small ROI samples were reported to be most likely to exclude the necrosis while including most of a viable solid tumour and, therefore, yielding a lower ADC value (88). On the other hand, large ROI suffered from larger variance and higher standard deviation, which were likely to reflect heterogeneity in the tumour due to evidence of solid foci, necrosis, and fibrosis in the tumour volume. Although the nodal volume measurement was reproducible, the ADC measurements showed a higher dependency on the ROI selected. This may lead to inaccurate ADC measurement, which increases uncertainty about the ability of nodal physical features underlying the tissue property. A recent study reported that small lymph nodes may harbour malignancy whereas enlarged nodes may be reactive (39). The enlarged lymph nodes are likely to be identified as malignant and are therefore responsible for false positives in the overall lymph node assessment (51). A low Pearson correlation coefficient showed that less than 40 % of the ADC values in metastatic nodes were explained by their volume (40). No correlation was reported between lymph node size and the presence of metastases (41). Further, the nodal physical features such as roundness and regional grouping of lymph nodes, extracapsular tumour spread or the presence of necrosis are equally indicative of nodal

23

malignancy (41,47,51,53,90). Although the presence of necrosis is found to be the strongest indicator for metastatic disease, surprisingly necrosis has been shown to occur in benign nodes as well (91).

A related in vivo study showed a low Pearson correlation for ADC values and metastatic and hyperplastic lymph node volume, with correlation values of 0.38 and 0.46, respectively (40). Increased tumour growth and the presence of necrosis were found to cause a increased in ADC values. At the end of the experiment, however, only two out of 24 lymph nodes were identified as having necrosis. Therefore, it is questionable whether the increased ADC values at the later period were due to necrosis as only about 30 - 40% of lymph node volumes were used to determine the ADC values (40).

Characterisation of nodal diseases using nodal anatomical features appearing on DWI images (i.e., lymph node size) failed to differentiate metastatic from normal nodes (89). Metastatic lymph nodes were found in each size category. Using the short-axis diameter, the results were as follows: less than 3 mm (68 metastatic lymph nodes); 3-5 mm (13), 5-8 mm (5) and more than 8 mm (2). The study also found insignificant differences between histopathologically malignant and benign lymph nodes with $p = 0.167$ (89). The study concluded that the size of the lymph node is a weak determinant for DWI in differentiating malignant from benign lymph nodes.

Compared to physical features, analysis of microstructural changes in the tissue has provided more reliable and consistent results for detection and discrimination of solid cancer in DWI. Related studies on prostate and breast tissue have shown a distinct diffusivity value in cancerous and normal tissue microstructures (2,8). However, no such studies have been reported in the literature for nodal tissue. This suggests that microstructural changes in the tissues do show distinct diffusivities in different tissue types. Findings on prostate and breast tissue indicate the need for a similar study on lymph node tissue to broaden our understanding of biophysical changes and their relationship to DWI tissue contrast.

'Cellularity' is often cited as the major cause of the variation in diffusivity reported in the literature. However, no previous study has measured cellularity in nodal diseases. It is important to note that an important gap in our understanding of DWI imaging is better understanding in the relationship between the diffusion signal and the underlying biophysical propertiesof the tissue. Yet the relationship between microstructural changes of known

histopathology using microscopic examination and the diffusion tissue contrast in DWI signal isnot well understood. One possible approach is to identify the microstructural change in nodal disease and determine its correlation with the diffusivity value using microimaging. Alternatively, a multi biophysical model of the diffusion could be developed exclusively for nodal disease. The monoexponential model, however, was reported as inaccurate in determining the diffusivity behaviour of water molecules in tissue. The following sections elaborate the correlation of ADC with cellularity and the development of a diffusion imaging model.

2.2   ADC and Cellularity

Most previous studies have reported that ADC changes observed in lymph node tissue were related to tissue cellularity, apart from the presence of necrosis and fibrosis (47,51,82,84,92). Cellularity is a measure of the total number of nuclei over a square unit of tissue area. Lower ADC values were consistently reported in malignant tissue because of its hypercellularity: the increased number of cells reduce the extracellular space, thus restricting the water diffusivity in malignant tissue. Benign lesions were associated with higher ADC values as the result of their hypocellularity, in which the number of shrunk nuclei is reduced, thus increasing the extracellular space resulting in higher diffusivity.

Relevant findings, however, have been inconsistent and contradictory. In several studies, relatively higher ADC values were observed in malignant nodal tissue in comparison with benign tissue, and it was presumed that cellularity was the main cause of this differentiation. Such a conclusion points to a lack of understanding of cellularity, since cellularity alone is considered insufficient to explain the variation in diffusivities from in-vivo imaging (93). Several studies were carried out to determine the correlation between ADC changes and the cellularity of the tissue being examined, as listed in Table 2.2.

Table 2.2 Reported Correlations between ADC and 'Cellularity' in DWI Studies

Disease	Study	Correlation coefficient (r [a])	p
Brain Cancer	Sugahara et al. 1998 (94)	$r = -0.77$	0.007
Brain Cancer	Gupta et al. 2000 (95)	$r = -0.67$	0.07
Brain Cancer	Gauvain et al. 2001 (96)	$r = -0.68$	0.014
Breast Cancer	Guo et al. 2002 (97)	$r = -0.53$	<0.001
Renal Cancer	Manenti et al. 2008 (13)	$r = -0.73$	<0.01
Breast Cancer	Yoshikawa et al. 2008 (98)	$r = 0.05$	0.8121
Breast Cancer	Hatakenaka et al. 2008 (99)	$r = -0.45$	<0.01
Prostate Cancer	Zelhof et al. 2009 (100)	$r = -0.50$	<0.0001
Prostate Cancer	Gibbs et al. 2009 (101)	$r = -0.70$	<0.0001
Prostate Cancer	Wang et al. 2009 (102)	$r = -0.65$	<0.05
Lymphoma	Wu et al. 2013 (103)	$r = 0.10$	0.58
Brain Cancer	Surov et al. 2015 (104)	$r = -0.70$	0.001
Breast Cancer	Onishi et Al. 2015 (105)	$r = -0.80$	<0.001

[a] Pearson product-moment correlation coefficient (r)

A number of studies on brain diseases have reported correlation between cellularity and ADC changes (94-96,104). However, histopathological criteria in neuronal diseases are known to differ from those in non-neuronal diseases as they are anatomically and physiologically different in the human body. It would be inaccurate to draw inferences from DWI imaging of neuronal cases for non-neuronal cases. Further research is therefore warranted on the application of DWI, particularly in non-neuronal diseases. In line with this, several studies have investigated non-neuronal diseases. Studies on adenocarcinoma (a type of cancer formed in glandular structures like the prostate and the breast) to determine the correlation between tissue cellularity and ADC values were only able to produce inconclusive findings

(97-102,105). Nevertheless, their results have provided a better understanding of diffusivity behaviour, which has implications for other non-neuronal diseases such as nodal disease.

Most cellularity measurements on solid cancer have reported a significant negative correlation between ADC values and tissue cellularity (97-102,105). Microstructural changes observed in cancerous tissue have been found to show a significant correlation with ADC variation, as reported in prostate studies (101,102,106). One study reported a significantly lower cell density in the normal peripheral zone than in the prostatic carcinoma, which was nearly double the cellularity in normal prostate tissue (101). The study suggested that the ADC reduction in prostatic carcinoma was due to the replacement of the normal acinar structure with more tightly packed cancer cells. Another recent study revealed that the cell density of normal prostate tissue is highly heterogeneous (106). Another study with similar findings reported that the loose stroma in prostate cancer is replaced with densely packed malignant epithelial cells (102). These studies indicate that, apart from cellularity, the microstructural changes in cancerous tissue cause variations in ADC values as reported in DWI imaging.

Besides cellularity and the microstructural changes in tissue, the amount of stromal and epithelial in the tissue was also found cause variations in ADC values.   Therefore, further analysis of prostate tissue components in ADC was conducted (107,108). According to a related study, the amount of stromal and epithelial contribution was more significant than that of cellularity in distinguishing cancer from healthy tissue (107).

Specifically, the study argued that, although solid tumour growth was the most predictive histological feature on MRI, the prognostic significance of this feature remains unknown (107). A similar study also reported an evidence of the presence of desmoplastic stroma and solid tumour growth in each tumour (108). The later study also suggested that epithelium and loose stroma can be used as an alternative to nuclear cell counting. The proportions of cellular components in prostatic cancer in comparison with normal prostate tissue were 24 % and 14 % of nuclei and 23 % and 16 % of cytoplasm, respectively. A significantly lower percentage of luminal space (14 %) was reported in cancer as compared to normal prostate tissue (30 %) (108). Each of the components pointed to significant differences in proportion and percentage in normal and cancerous tissues, which might help to explain the reported variation of ADC values.

In addition to the component analysis of prostate tissue, several studies have reported insignificant differences between ADC values and cellularity of prostate tissue (40,89,103). For nodal disease, a study on 32 patients with diffuse large B-cell lymphoma (DLBCL) found that the ADC of DLBCL was quite similar to that of lobular lymphoma (103). The study suggested that histological features such as cell size, cellular organisation and extracellular matrix may contribute equally to the tissues' diffusivities. These are other possible explanations for the variation in ADC values which indicate that it is not solely due to cellularity.

Brain tumour specifically in gliomas tissue, however, reported a higher cellularity value than prostate tissue (94). Such a difference suggests that each tissue's histological characteristics possess unique cellularity values. On the other hand, no study to date has investigated the cellularity of the lymph node and its association with ADC values.

As previously mentioned, other than cellularity, the presence of necrosis and fibrosis does affect the measurement of ADC values. A study involving 21 patients with varying percentages of necrosis in hepatocellular lesions reported significant differences between ADC and necrotic tumours with $p < .05(12)$. The study argued that the increased ADC values in necrotic tissue were due to tissue damage or disruption of the cellular membrane that allowed water to diffuse more freely than in the tumour tissue without necrosis.

Another study involving 23 chronic hepatitis patients and seven healthy volunteers demonstrated a negative correlation between ADC and the stage of fibrosis (109). Although these studies reported that the presence of necrosis and fibrosis in the tumour tissue correlated with the ADC values, the underlying biophysical change in the diffusion tissue contrast is still not well understood. Further, these studies assumed that necrosis and fibrosis were altering the cellularity of the tumour tissue and damaging the cell membrane, increasing water diffusivity and apparently reducing the detected diffusion signal. Therefore, there is an urgent need to determine the specific cellularity properties of lymph node tissue.

Cellularity measurement

The idea that 'cellularity' is the biophysical basis of ADC variation is an extrapolation from studies of brain imaging, but this appears to lack a sound biophysical foundation. The cellularity metrics that are most commonly used are nuclear count and nuclear area(93,110). Nuclear count is the total number of nuclei per unit area in a histological section while nuclear area is a percentage of total nuclei per unit area of the histological section. Nuclear area can be given either as absolute value or as a percentage.

The methods most commonly used to measure cellularity in the literature on DWI are shown in Table 2.3. Two main methods are employed: manual counting and auto segmentation. Manual counting depends on the visibility of the nuclei under the microscope and is limited to the current field of view. Auto segmentation is a software-based counting method with a relatively larger field of view. As listed in Table 2.3most of the methods were lack in details. The need for a more specific and detailed method has led to a shift from manual nuclei counting to automated nuclei segmentation. Manual counting is time-consuming, prone to error and highly dependent on the operator's skills. The introduction of auto nuclei segmentation has provided a more accurate and reliable method of cellularity measurement.

The most important aspect of cellularity measurement is nuclei detection. Different types of nuclei exist in human tissue; lymphocytes are particularly important for lymph node tissue. Therefore, the ability to identify small lymphocytes from the mixture of cells in nodal tissue is crucial for automated nuclei segmentation.

Automated nuclei segmentation has gained wide acceptance among pathologists for quantitative analysis of pathological images because it is more efficient and provides enhanced accuracy. However, the detection and segmentation of nuclei is more challenging for clustered and overlapping nuclei. An optimum visualization of the nuclei at the microscopic level can be obtained by using an appropriate staining method. The use of hematoxylin and eosin (H&E) staining protocol has been widely accepted for quantitative assessment, since it has proven to provide better visualisation and differentiation of the nuclei from other -microcomponents in the tissue.

Table 2.3 Reported Methods of Cellularity Measurement in DWI Studies			
Study	**Disease**	**Method/Tool**	**Cellularity Metric**
Sugahara et al. 1998 (94)	Brain Cancer	Manual Counts	Nuclear Area
Gupta et al. 2000 (95)	Brain Cancer	Manual Counts	Nuclear Count
Gauvain et al. 2001 (96)	Brain Cancer	Manual Counts	Nuclear Count
Guo et al. 2002 (97)	Breast Cancer	Manual Counts /Adobe Photoshop	Nuclear Area
Manenti et al. 2008 (13)	Renal Cancer	Auto Segmentation	Nuclear Count
Yoshikawa et al. 2008 (98)	Breast Cancer	Auto Segmentation /Scion Image Beta Software	Nuclear Count
Hatakenaka et al. 2008 (99)	Breast Cancer	Manual Counts / microscope	Nuclear Area
Zelhof et al. 2009 (100)	Prostate Cancer	Auto Segmentation / Matlab Software	Nuclear Area
Gibbs et al. 2009 (101)	Prostate Cancer	Auto Segmentation / Matlab Software	Nuclear Area
Wang et al. 2009 (102)	Prostate Cancer	Manual Counts / microscope	Nuclear Area
Wu et al. 2013 (103)	Lymphoma	Auto Segmentation/ BioImage XD Software	Nuclear Count
Surov et al. 2015 (104)	Meningioma	Auto Segmentation/Analyze Particle Tool	Nuclear Area, Nuclear Count
Onishi et al. 2015 (105)	Breast Cancer	Manual Counts / microscope	Nuclear Area

A range of auto-segmentation software is presently available in advanced image processing programs, which are capable of segmenting the overlapping and clustered nuclei (111). A machine learning technique employed in the software, for example, represents an important advance in quantitative histology assessment. The machine learning technique is considered user-friendly and can generate a more accurate quantitative measurement for both clinical cancer assessment and research purposes. The profile obtained from the quantitative histology assessment at microscopic level has huge potential to explain the underlying microscopic changes in cancerous and non-cancerous tissue. In future,a digital histopathology might be - part of routine cancer assessment with shorter time of analysis compared to the

manual histopathology. However, the translation of this research into clinical practice requires more time and rigorous research.

Besides measurement of tissue cellularity, the underlying biophysical changes affecting the diffusion tissue contrast can be examined using multi biophysical modelling. The development of diffusion imaging modelling is discussed in the following section.

2.3   Modelling of DWI Signal Attenuation

In free diffusion, displacement of the water molecules follows a normal distribution with a time dependent standard deviation.. In the tissue, the displacement of water molecules is affected by the densely packed cells. Therefore, DWI signals in the tissue are sensitive to microstructural changes at the cellular level and the displacement deviates from the normal distribution. The analysis of DWI signal behaviour is of utmost importance for both preclinical and clinical studies. Analytical models have been proposed to describe the behaviour of DWI signals in the tissue to provide quantitative information on the underlying tissue microstructures.

The analytical models are divided into two categories: signal and biophysical. Signal models aim to provide reliable mathematical descriptions of DWI signals but they offer only limited biophysical insights. Biophysical models are based on the diffusion properties of each structural biophysical within a tissue and aim to provide parameters directly linked to the specific tissue structures. Biophysical models have been proven successful in brain imaging and have recently gained increased attention for non-neuro imaging. In the following section, models of water diffusion in the tissue are reviewed.

Signal models

The DWI signal for bulk water molecules is described using monoexponential function analysis. Monoexponential function analysis is based on a normal Gaussian distribution of molecular displacement, in which the signal intensity of diffusing water molecules decays exponentiallywith increasing b-values. Simple monoexponential function analysis, also known as the ADC model, was discussed in Chapter 1:

$$S = S_0 \exp(-b.ADC) \qquad [2.1]$$

31

Monoexponential function analysis is widely accepted for DWI in clinical studies, including studies on node tissue. Some studies have highlighted the potential usefulness of DWI in the assessment of lymph node aggressiveness, with b-values ranging from 800–1500 s/mm^2 (15,16,82)

However, water molecules are not able to diffuse freely in space owing partly to the presence of multicomponents in a tissue. Water diffusivity is restricted due to the interaction between water molecules and the multiple components in the tissue, which causes deviation of the DWI signal from monoexponential behaviours. Some studies have suggested using non-monoexponential function analysis to characterise water diffusivity in the tissue, particularly biexponential function analysis (112,113), stretched exponential function analysis (114) and diffusion kurtosis function analysis (115), to further investigate the water diffusion behaviour of tissue in DWI imaging.

Biexponential function analysis shows a better fit to the data for in-vivo studies on prostate tissue, with biexponential function analysis on extended b-values quantifying the diffusion signal intensities into fast and slow components of water diffusivity for prostate tissue (112,113). Biexponential function analysis is depicted in the equation:

$$S = S_0 \left[(1 - f) \, e^{-b \, D_s} + f e^{-b D_f} \right] \qquad [2.2]$$

where D_s and D_f are the slow and fast diffusion coefficients, respectively, and f is the fraction of the fast component. Biexponential function analysis can be used to determine the slow and fast diffusivities components by using a range of b-values going up to high b-values with a maximum of at least 2000 s/mm^2, as well as for modelling perfusion/tissue fractions, in which case small b-values are also required in the measurements.The fast component is used to describe biophysical components of extracellular spaces (ECS), whereas the slow component is used to describe intracellular spaces (ICS) in the tissue (112,113). According to the literature, however, the origin of the fast and slow diffusion coefficient pools is not well understood (116).

In-vitro experiments on single cells in a range of b-values going up to high b-values with a maximum of 6500 s/mm^2, show an over-simplistic use of biexponential function analysis to determine intracellular and extracellular space in the cells (117-119). The biexponential fitting of DWI signals in erythrocyte cells demonstrated inaccurate counts because the fitting model was unable to account for significant water exchange between ICS and ECS

compartments in diffusion times of 7-35 ms (117). The nucleus of neuronal cells demonstrated predominantly monoexponential signal decay with only a slightly biexponential nature, whereas the cytoplasm appeared to have a predominantly biexponential signal decay with increasing *b*-values. It is believed that the slowly diffusing component originated from the intracellular space. The nucleus had reduced structural complexity in comparison with the cytoplasm, making the nucleus more favourable for monoexponential decay (118). Another study in heart tissue (i.e., myocardial cells) showed a decline in signal intensity when plotted as a function of diffusion gradient *b*-values and is considered best fitted to biexponential function analysis. This is partly because heart tissue has a larger volume of vascular tissue than the brain (14-22 % vs. 5 %). The signal from heart tissue consist of perfusion and diffusion components and contribute to the fast diffusion coefficient. The fast diffusion component accounted for 82 % of the total signal of the myocardial cells (119).

Single cell studies using biexponential function analysis have revealed a significantly different proportion of the slow diffusion coefficient, D_s, and the fast diffusion coefficient, D_f, in range of *b*-values going up to high *b*-values with a maximum of 6500 s/mm^2 experiments (117-119). Most importantly, these studies have produced evidence of deviation from monoexponential diffusion signal behaviour at the cellular level, which may contribute to a better understanding of the non-monoexponential diffusion decay reported in both normal and cancerous tissue. Therefore, there is a need to investigate diffusion signal behaviour at the microscopic level using biexponential functional analysis of the microimaging MR unit as well as other models, including stretched function analysis and kurtosis function analysis.

Stretched function analysis was initially developed to account for the possibilities of continuous distribution of the diffusion coefficient arising from multiple compartments. An experiment involving eight rats in a 3T MR scanner with extended *b*-values (range 0-6500 s/mm^2) reported a better fit of the diffusion signal in the rat brain with stretched decay function analysis than with biexponential function analysis (114). The stretched model is depicted in the following equation:

$$S = S_0 \ \exp(-(b.DDC)^\alpha)$$ [2.3]

In stretched models, unlike biexponential function analysis. no assumptions are made in relation to the number of intravoxel proton pools. Two parameters, the alpha (α) and distributed diffusion coefficient (DDC), are usually used to characterise the diffusion process.

The study demonstrated heterogeneity in water diffusion through an experiment using a phantom solution of 1.5 ml 10% ethanol measured by parameter α. In particular, a low α was reported in the central cortex and a high α in the upper portion of the cortex. The parametric map of DDC and α of stretched function analysis also identified a significant contrast between the white matter and the cortex region (114). The results from this experiment shows that diffusion contrast can be observed using stretched function analysis.

Then,diffusion kurtosis function analysis was introduced to characterise high b-value DWI signal attenuation behaviours (120). The deviation of measured signal intensity from Gaussian distribution was calculated using two parameters: the kurtosis diffusion coefficient (D_k) and the kurtosis coefficient (K).

$$S = S_0 \exp(-b\, D_k + \frac{1}{6}\, b^2\, D^2\, K) \qquad [2.4]$$

Unlike biexponential function analysis, kurtosis and stretched function analysis does not include any components element in characterising diffusion signal behaviour. A study involving 6 healthy adult volunteers scanned with a 3T MR unit using extended b-vales (range 0-2500 s/mm^2) reported a substantial deviation of the signal from Gaussian diffusion in gray matter and white matter of the brain using kurtosis diffusion analysis. In particular, the apparent diffusion kurtosis in the frontal white matter was about 70 % higher than in the cortical grey matter, reflecting a higher degree of structure in white matter than in grey matter. Similar findings were reported in the same study using a phantom made of sucrose solution and asparagus puree. Besides the tissue structure, there was other evidence to suggest that macromolecule concentration does have an important role to play in relation to the diffusion behaviour in tissue (115,120).

In a simple experiment on the phantom in stretched function analysis (114) and kurtosis function analysis (115) , substantial evidence was found; K and α values demonstrated the heterogeneity property of the tissue that may result in non-monoexponential behaviour of the diffusion signal. Clinical imaging studies also had reported potential of differentiating non-cancerous from cancerous prostate using biexponential function analysis (113), stretched function analysis (121) and kurtosis function analysis (122).

Biophysical models

Biophysical models aim to provide sensitivity to microstructural changes in tissue. The parameters in biophysical models are directly related to properties of the tissue structure. One of the early attempts to model DWI signals in tissue in-vivo using this approach was called intravoxel incoherent motion (IVIM). The IVIM model, which was proposed by LeBihan et al. (123), divides the tissue into vascular and nonvascular components and is represented by a biexponential function analysis:

$$S = S_0 (1 - f)e^{-bD} + fe^{-bD^*}$$
[2.5]

where D^* is the perfusion coefficient that describes incoherent movement of blood in microvasculature, f is the perfusion fraction signifying the fraction of signal from perfusion, and D is the true molecular diffusion. Biexponential function analysis were used to determine the slow and fast diffusivities components only and IVIM used the same basic equation of biexponential function alaysis to further determine vascular components in the tissue. IVIM modelling requires measurements with small b values to estimate the perfusion fraction. Three recent studies have demonstrated that the IVIM model is useful for discrimination of nodal diseases (124,125) and prediction of treatment response in nodes (126). Significantly lower D (diffusion coefficient) and D^* (perfusion coefficient) were reported in metastatic lymph nodes in comparison with non-metastatic lymph nodes. In contrast, in the study using extended b-values (range 0-800 s/mm^2) no significant differences were reported in f (perfusion fraction) (124). Interestingly, another related study using extended b-values (range 0-2000 s/mm^2) reported significantly higher D and f values in metastatic lymph nodes than those of normal lymph nodes and significantly lower D^* in metastatic lymph nodes (125). IVIM analysis has also shown that the f in lymph nodes might be helpful for prediction of treatment response in head and neck carcinomas (126).

Recently, the VERDICT (Vascular, Extracellular and Restricted Diffusion for Cytometry in Tumors) model was proposed to model DWI signals in tissue in-vivo using three compartments (127). Beside VERDICT, there are other multi-compartment models for cancer imaging such as IMPULSED (imaging microstructural parameters using limited spectrally edited diffusion) model and POMACE (Pulsed and oscillating gradient MRI for assessment of cell size and extracellular space) model (128). VERDICT is a framework which combines an optimised acquisition protocol with multiple b-values and diffusion times and a multi-

biophysical tissue model. VERDICT characterises diffusion signals in three distinct microstructural environments: restricted diffusion inside cells, hindered diffusion outside cells and blood vessels, and isotropic restricted pseudo-diffusion inside blood vessels. The model estimates parameters such as cell diameter, intracellular diffusivity, intracellular volume fraction, extracellular extravascular volume fraction, extracellular extravascular diffusivity, pseudo diffusivity and vascular volume fraction. The signal is the sum of contributions from the three individual compartments, denoted by:

$$S = \sum_{i=1}^{3} f_i S_i \qquad [2.6]$$
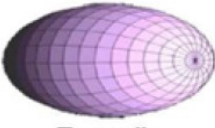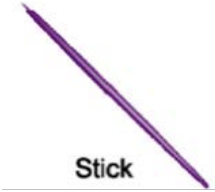
where S_i is the signal from each parameter and f_i is the fraction of signal of that component. The VERDICT model has recently been used to model colorectal (127,129) and prostate cancer (129). The model is capable of differentiating cancerous from normal tissue. It also provides parameter estimation, which corresponds to specific tissue histology of the prostate (129). These pioneer biophysical model studies have demonstrated their superiority to signal models in cancer detection and ability to infer tissue microstructure.

The present study used fixed tissue samples without perfusion effect. Therefore, two important effects may have to be taken into consideration in modelling water diffusion in non-neural tissue:

1) Restricted diffusion of water molecules inside cells.
2) Hindered diffusion of water molecules in the extracellular space.

During DWI imaging, cells might have experienced water exchange through the cell membranes. The exchange of water through the membrane of the cells depends on the cell type. No water exchange between compartments was assumed in the present ex vivo imaging study as samples used were fixed tissue. Five single biophysical models from white matter (130) were implemented in the present study in order to model restricted and hindered diffusion in lymph node tissue. The single biophysical models were as listed in Table 2.4, where :

1. 'Ball', an isotropic tensor. The model has only one parameter, diffusivity D.

2. 'Zeppelin', a cylindrically symmetric tensor. The model has the principle eigenvectors, parallel diffusivity $D_{\|}$, and perpendicular diffusivity $D_{\perp}$.

3. 'Tensor', a conventional single-component DTI model. The model provides the following parameters: parallel diffusivity $D_{\|}$, two perpendicular diffusivities $D_{\perp 1}$, $D_{\perp 2}$, and three orthogonal eigenvectors ε, $\varepsilon_{\perp 1}$, $\varepsilon_{\perp 2}$.

4. 'Stick', which assumes diffusion within an idealised cylinder of zero radius. The model has a direction n and diffusivity D as parameters.

5. 'Sphere', which describes restricted diffusion inside an impermeable spherical pore with a non-zero radius Rs.

Table 2.4 Biophysical Models for Non-neural Tissue

Model	Form[a]	Degrees of freedom
Ball	$D = DI$	D
Zeppelin	$D = \alpha\varepsilon\varepsilon^T + \beta I, D_{II} = \alpha + \beta, D_\perp$	$D_{II}, D_{\perp1}, \theta, \phi$
Tensor	$D = D_{II}\varepsilon\varepsilon^T + D_{\perp1}\varepsilon_{\perp1}\varepsilon_{\perp1}^T + D_{\perp2}\varepsilon_{\perp2}\varepsilon_{\perp2}^T$	$D_{II}, D_{\perp1}, D_{\perp2}, \theta, \phi, \alpha$
Stick	$S = e^{-bD(nG)^2}$	D, θ, ϕ
Sphere	GPD approximation. $R_s > 0$	D, R_s

a) **D** is the diffusion tensor. **I** is the identity tensor. θ, ϕ, α are tensor angles.

2.4 Diffusion Microimaging

Obtaining a good correlation between in vivo diffusion signal and histopathological status of the tissue is extremely difficult. The accuracy of in-vivo imaging is hampered by low signal-to-noise ratio (SNR) and low spatial resolution due low field strength. However, these problems can be reduced using ex vivo diffusion imaging at a high field which offers better signal-to-noise ratio (SNR) and higher spatial resolution. In other words, the comparisonbetween biophysical features of tissue and the diffusion signal can be improved and better explained by using ex vivo imaging. Although ex vivo imaging is very important and useful, it is only an estimate of what one can expect in vivo, so caution is needed when extrapolating ex vivo results into in vivo situation.

As mentioned earlier, a related study on diffusion microimaging showed a good correlation between in-vivo and ex vivo DTI of prostate tissue and its histopathological status. Specifically, the study reported distinguishable ADC values in cancerous and noncancerous tissue in the peripheral zone (PZ) region of the prostate (131). The reported ADC values were lower in the ex vivo experiment than the in-vivo experiments. The study observed no significant diffusion anisotropy differences between cancerous and non-cancerous prostate tissue in both ex vivo and in-vivo imaging. The network of fibromuscular connective tissue leads to the observed diffusion anisotropy. Interestingly, the study also reported of no histological evidence of increased density of fibromuscular tissue in cancerous tissue (131). The distinguishable ADC values reported in prostate tissue in this study shows that diffusivity values is better than using diffusion anisotropy to differentiate cancerous and noncancerous tissue.

A recent ex vivo DTI study reported a distinct mean diffusivity (MD) of the ducts/lumen, stroma, and epithelia in normal prostate tissue (8). In that study, mean diffusivity was used instead of ADC values to accommodate the contribution of diffusion signals resulting from six gradient directions (78). The study also showed low diffusivity in the epithelial layer, moderate diffusivity in the stroma, and fast diffusion in ducts. The ultra-highspatial resolution that was achieved by using a 16T MRI scanner (40 µm isotropic) provided the advantage of reduced partial volume effects. The diffusion anisotropy appeared higher in the stromal tissue than in the epithelia. These results are consistent with previous work (8).

Although the study on diffusion microimaging has shown distinct mean diffusivity in sub-structures of prostate tissue using ex vivo DTI imaging at a higher field, no similar work has been reported for lymph node tissue to date. A recent study of ex vivo DWI on lymph node tissue using a 7T MRI unit reported distinguishable ADC values in benign and metastatic nodes. The study suggested that the discrimination of metastatic from nonmetastatic nodes based on assessment of nodal anatomical features was challenging (90). Nevertheless, ADC values were not reported in the microstructures of the lymph node. In this regard, it is more likely that the study was not able to report the specific ADC values on the microstructure of the lymph nodes owing to the poor tissue contrast on ADC maps from the DWI imaging. Therefore, ex vivo DTI imaging of the lymph nodes tissue is needed to better understand the biophysical bases of the diffusion contrast and determine the correlation between the diffusion signal and the histopathological status of the lymph node.

2.5   Problem Statement

The underlying biophysical origin of diffusion contrast in cancerous and normal tissue remains poorly understood. The development of DWI for lymph node assessment depends on understanding how water diffusion is affected by the changes in tissue structure that characterise the presence of cancer. An improved understanding of the biophysical basis of diffusion contrast on the tissue can help to guide the development of available MRI methods to provide more reliable insights into, for instance, cancer localisation and differentiation of nodal disease. This in turn will facilitate patient management via a more precise and effective treatment.

2.6   Hypothesis and Aims

This study aims to define the biophysical basis of contrast in DWI of the lymph node. Specifically, it investigates the hypothesis that the clinically observed decreased ADC of cancerous lymph nodes can be explained by increased cellularity. It also investigates the theoretical information content of single and multi-biophysical models that include combinations of isotropic, anisotropic and restricted components in lymph node tissues. Models were ranked using the Akaike information criterion (AIC), which compared models based on its theoretical information. The modelling will identify compartments that are considered necessary for accurately describing DWI signals in lymph node tissues.

The objectives of the study are to:

1. Characterise the microscopic structure of nodes and investigate the correlation between mean diffusivity (MD) and cellularity metrics using DWI on high-resolution 16.4 Tesla MRI
2. Investigate the theoretical information content of single- and multi- biophysical models of DWI signal attenuation measured over an extended range of b-values and multiple diffusion times with the combination of isotropic, anisotropic and restricted components.

3. Correlation of Cellularity Metrics with Mean Diffusivity

3.1 Introduction

The development of the full potential of DWI methods for lymph node cancer assessment depends on better understanding how water diffusion is affected by the changes in tissue structure that characterise the presence of cancer. Recent reviews of related literature have highlighted the importance of nodal assessment and thus suggested the inclusion of nodal assessment as part of routine primary tumour assessment (73). The major cause of cancer-related death was reported to be the spread of cancer cells, or metastasis, to nearby tissues inside the body, including the lymph node tissue (23). The application of DWI in the detection of solid cancer shows potential for differentiating cancerous from non-cancerous tissue (2,8,9). Previous studies carried out on breast and prostate tissue demonstrated distinct diffusivities of the gland tissue microstructures (2,8). A similar study on lymph node tissue would represent the first step toward understanding the biophysical characteristics of the tissue underlying the variations in diffusivity of cancerous lymph node tissue reported in the literature.

Cellularity is commonly assumed in the literature to be the main factor responsible for variation in water diffusivity. The generalisation of much published research on DWI based on this assumption is problematic. Moreover, recent studies have demonstrated that microstructures in glands of prostate tissue, including epithelium, stroma and lumen space, show a stronger correlation with the ADC than the commonly cited 'cellularity' does with ADC (93). To the best of our knowledge, no previous study has been conducted to investigate ADC and cellularity in lymph node tissue. Instead of ADC values, mean diffusivity (MD) values were used in this study because this has the advantage of averaging the diffusivity measurement over six gradient directions. MD is comparable to ADC in DWI.

This chapter reports on a study in which formalin fixed lymph node tissue was imaged using a 16.4T MR system to measure the MD and determine the correlation of measured diffusivities with cellularity metrics. Formalin-fixed tissue in ex vivo imaging experiment has been demonstrated to be a stable model for investigating microscopic diffusion properties of

tissue (132). The study quantified the cellularity metrics and tissue composition changes associated with pathological conditions of the lymph node tissue, including metastatic, normal, and lymphoma cases. It also investigated the hypothesis that the clinically observed decrease in ADC values in lymph node cancer can be attributed to increased cell density.

3.2 Methods

3.2.1 Materials

Lymph node tissue samples were collected from humans and animals, as shown in Table 3.1.

Human tissue samples

The study was conducted with institutional ethical approval from Strathfield Private Hospital (Sydney, New South Wales) and Concord Hospital (Sydney, New South Wales) and written consent from all participating patients. A copy of the institutional ethical approval can be found in the Appendix.The lymph node tissue was collected from breast cancer and inflammatory bowel disease surgery. The lymph nodes were immersed in 10% neutral buffered formalin post-surgery to preserve the specimens.

Axillary node tissue was collected from breast cancer patients aged 50-60 years (mean 55 years). A total of six lymph node tissue samples were collected between April 2014 and April 2016 from five patients as part of routine surgery. A minimum of one lymph node was resected from each patient. The mean short axis diameter of the specimens was 5 mm (range 3-8 mm) and the mean long axis diameter was 5 mm (range 3-10 mm).

Mesenteric node tissue was collected from patients aged 50-60 years (mean 55 years). Between August 2015 and April 2016 a total of eight lymph node tissue samples were collected from five patients. A minimum of one and maximum of five nodes were obtained from each patient. The mean short axis diameter was 5 mm (range 3-8 mm). The mean long axis diameter was 5 mm (range 3-10 mm).

Animal tissue samples

Dog lymph node tissue was collected from Vetnostics (Sydney, New South Wales) Australia. A copy of ethics approval for tissue collection from the institution was attached in

"Appendix" of this thesis. The lymph nodes were immersed in 10% neutral buffered formalin post-surgery. Between August 2015 and April 2016 a total of six lymph node samples were collected from six dogs. The mean short axis diameter was 5 mm (range 3-10 mm). The mean long axis diameter was 8 mm (range 3-15 mm).

Table 3.1 Lymph Node Specimen Summary						
No	Subject	Pathology	Number of nodes	Number of cores imaged	Number of Histolgy slices	MR images with histo match
1	Human	Metastatic Axillary	2	3	23	11
2	Human	Metastatic Axillary	1	1	6	3
3	Human	Metastatic Axillary	1	1	5	7
4	Dog	Metastatic	1	1	5	5
5	Human	Normal Axillary	1	2	14	7
6	Human	Normal Axillary	1	2	8	7
7	Human	Normal Mesenteric	1	1	6	2
8	Human	Normal Mesenteric	1	1	5	2
9	Human	Normal Mesenteric	1	1	6	2
10	Human	Normal Mesenteric	2	2	14	4
11	Human	Normal Mesenteric	2	2	13	7
12	Dog	Lymphoma	1	1	6	5
13	Dog	Lymphoma	1	1	3	3
14	Dog	Lymphoma	1	1	4	4
15	Dog	Lymphoma	1	1	3	2
16	Dog	Lymphoma	1	1	3	2
Total			19	22	124	73

3.2.2 Tissue preparation

Excess fat around the node was carefully removed using a surgical scalpel blade. For each node, a 3 mm diameter core sample was extracted from the tissue using a core punch. For smaller nodes, the resulting sample was not a neat cylinder. For larger nodes; two core samples were obtained, if possible. The cores were glued to a plastic strip (cut from a laboratory chemical weigh boat) using cyanoacrylate "superglue" to fix the position of the core during imaging and histology sectioning. Tissue cores of not more than 15 mm in total length were fitted inside the sensitive region of the MRI RF coil. A minimum of three tissue cores were placed on a plastic strip (Figure 3.1).

Figure 3.1 Tissue cores glued to plastic strip for imaging

The glued samples were inserted into a 2 mL screw-top plastic vial and immersed in phosphate-buffered saline (PBS) containing 0.2% v/v Magnevist (Bayer Healthcare Pharmaceuticals, Berlin, Germany) and stored at least overnight at room temperature to wash out the formaldehyde. The PBS solution provides a known diffusivity background and the contrast agent reduces T1 to ~0.5 s, which enables a shorter TR and, thus, faster imaging. Samples in the vials filled with PBS solution were then mailed overnight to the Centre for Advanced Imaging, University of Queensland (CAI-UQ), for 16.4 T imaging.

3.2.3 MR imaging

The following MRI setup was performed by either Dr Gary Cowin or Dr Nyoman Kurniawan at CAI-UQ.

The tissue cores on the plastic strip were transferred into a 5 mm diameter NMR tube filled with PBS-Magnevist solution for imaging. The sample was degassed under vacuum to remove any air bubbles which would create magnetic susceptibility artefacts. Imaging was

performed on a Bruker (Kalsruhe, Germany) AV700 magnetic resonance microimaging system, which consists of a 16.4 T vertical bore magnet with a spectrometer running Paravision 4 and a 5 mm bird cage radiofrequency coil. The scanner was equipped with a Micro 2.5 Gradient Set (2.5 mT/m). Imaging was performed at a monitored room temperature (22^oC). For diffusion-weighted imaging, a 3D spin echo diffusion tensor imaging (DTI) sequence was employed with the parameters listed in Table 3.2. The typical imaging time was 36 hr (range: 25-72 hr).

Table 3.2 DWI Acquisition Parameters	
FOV (mm^3)	20.5 × 5.1 × 5.1
Matrix size	512 × 128 × 128
Voxel size (μm^3)	40 × 40 × 40
SNR	23 − 28
TR (ms)	400, 500
TE (ms)	20
δ (ms)	2
Δ (ms)	12
b-value (s/mm^2) 6 directions	1000
a) Nominal b-value. Effective b-values were used for measurement of mean diffusivities.	

The signal-to-noise ratio (SNR) was measured from reference images at $b = 0$ and it was 23-28 in the parenchyma of the lymph node tissue. The SNR was measured from the ratio of the signal S, relative to the noise level N. The signal was taken as the mean DWI pixel intensity in a 'tissue only' region of interest (ROI) and noise as the standard deviation of the difference between the two reference images in the same region.

3.2.4 Histopathology: Morphology segmentation

Following the MR microimaging, the tissue cores were prepared for light microscopy. The tissue sectioning was guided by a visual assessment of the likely tissue type as seen in the MR images. The two dimensional (2D) DWI images and the 2D mean diffusivity images were used to guide the tissue sectioning, as presented in Figure 3.2 The samples were

sectioned and stained with haematoxylin and eosin (H&E) at the Lowy Cancer Research Institute, University of New South Wales, with the kind assistance of Dr Carl Power.
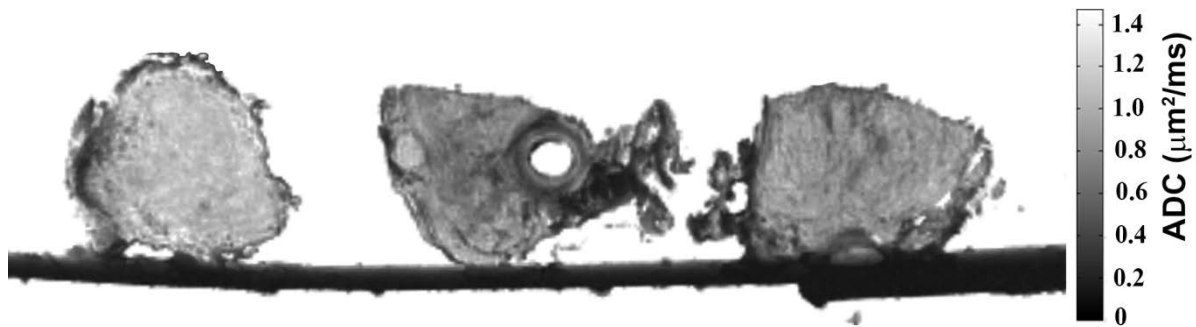
Figure 3.2 Lymph node tissue images on sagittal plane

DWI images on sagittal plane was used as pre-defined guide in the histo-sectioning process. Histopathology examination of the H&E stained slides was carried out by a histopathologist (Dr Geoff Watson) at the Department of Tissue Pathology and Diagnostic Oncology, Royal Prince Alfred Hospital (RPAH) in Sydney, New South Wales. The sub-structures, border of each sub-structure, and the cancer type of the tissue were identified and marked on colour prints of tissue sections.

H&E stained slides were digitally scanned at 40× magnification with a spatial resolution of 0.25 microns per pixel using a digital brightfield microscope (Aperio Scan Scope, Leica Biosystems Imaging Inc., Wetzlar, Germany). Images from the digital scanner were stored online via Aperio eSlide Manager (version 12.2) software in scope virtual slide (SVS) format. The SVS image files were viewed offline using Aperio Image Scope software (v12.10.5029). The "Zoom Navigation" and "Extract Image Region" tools were utilised to select subimages containing only the 3 mm core tissue. Typically, the scanned 3 mm diameter tissue sections were 11000 × 14000 pixels. The subimages were saved in lossless Portable Network Graphics (PNG) format for cellularity measurement.

3.2.5 MRI and Histology Image Alignment

A digital photograph of the specimen on the plastic strip was taken prior to MR imaging to aid the alignment of MR images with corresponding histopathology sections. Photographs were taken in two different views: perpendicular and parallel to the tissue cores. Any distinguishable physical characteristics of the tissue cores were noted. The qualitative assessment of the MR images was based on the identification of microstructures on DWI. A

region with homogeneous signal intensity on the MD map was categorised as a sub-structure of the tissue. The MR images were processed in MeVisLab (Mevislab Medical Solutions, Bremen, Germany) to perform 3D volume rendering, which assisted the tissue sectioning. Single and multiple image views were assessed using custom Matlab code (Mathworks, Natick, Massachusetts, USA) to assist the alignment between the MR image and its corresponding histological section.

Diffusion-weighted images transverse to the tissue core axis (same as MR axis) were aligned with histology slices from approximately the same planes (Figure 3.3). In most cases, the MR imaging planes were not matched to the histopathology section planes. To account for modest histological slicing and mounting distortions, a code was written in MATLAB R2012b (MathWorks, MA) to obtain an oblique slice in MR images. This can be done by firstly determined which of MR imaging plane that need to be rotated (x, y or z planes), then defined the degree of rotation angle and next used the rotated MR images to matched with the H&E section images. Once the angle of rotation is determined, multiples DWI images were displayed at certain separation depth to match with histopathology images. For example 15 pieces of MR images with (50 - 200 µm) separation depth were viewed at an angle of 5 degree of rotation. Adjacent MR slices were also checked for discrepancy and to minimize partial volume effects. Then, visual inspection of the rotated images were repeated for next consecutive MR images sequences until a satisfied closeness of match between MR images and H&E stained slices match were determined. The closeness of match was of MR images with H&E stained slices were used in the analysis.

ROIs were defined inside extensive well-defined lymph node microstructures in normal and cancerous regions mapped on the corresponding histological sections. A total of 73 MR images were considered to be sufficiently closely matched to the histological sections of the tissue samples from 16 subjects to enable reliable assessment of MR-histology correlations. The matched MR images included normal lymph node (n=31), metastatic lymph node (n=26), and Non-Hodgkin lymphoma (n=16).
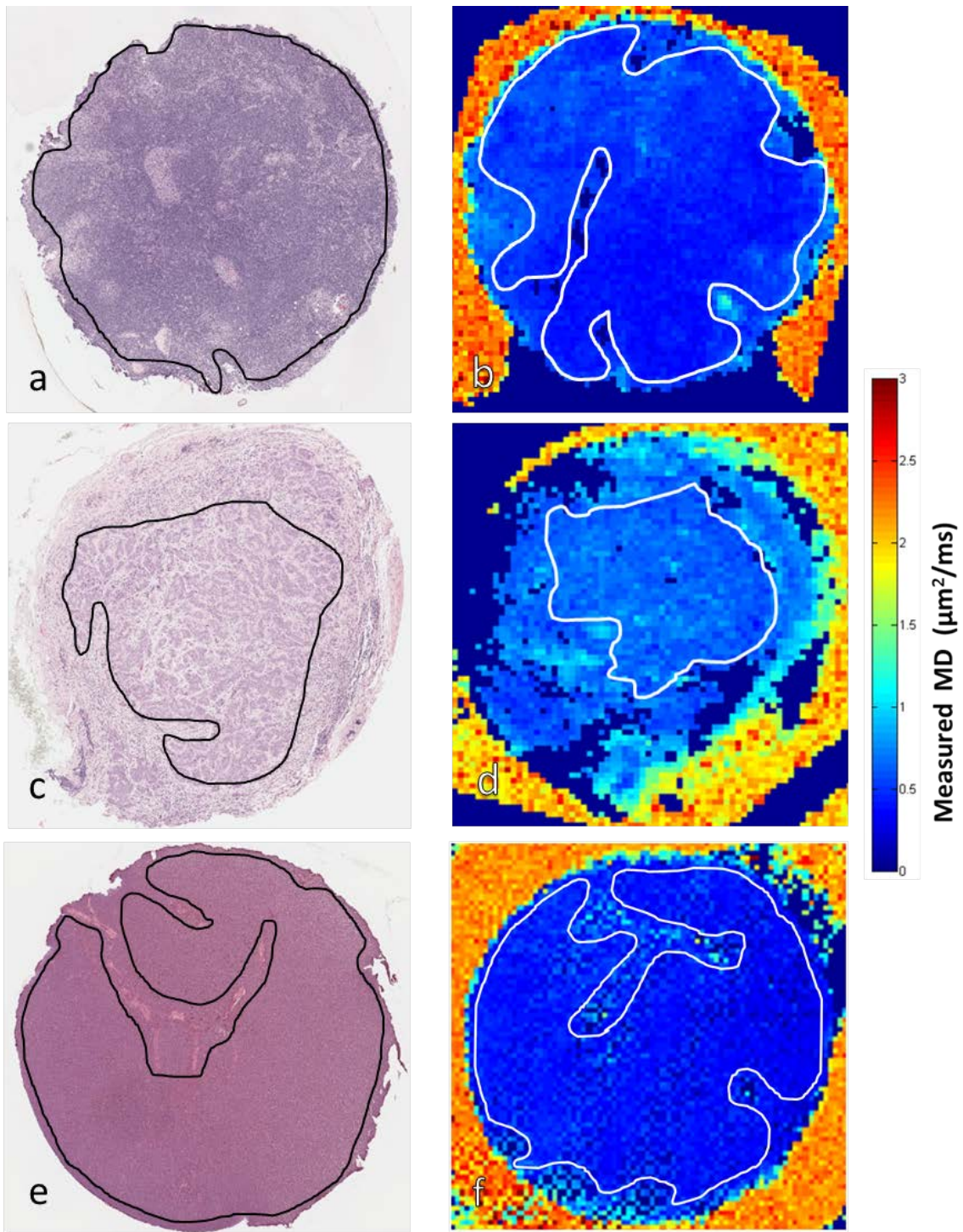
Figure 3.3 ROI selection in histology slices and MD map

Representative examples of ROI selection in H&E sections (a,c,e) and corresponding MD map (b,d,f) for lymph node tissue. A typical approximate ROI is defined in the parenchyma region as normal (a), metastatic (c) or lymphoma (e) node tissue. The ROIs drawn on MD

images in areas most representative of underlying tissue structures parenchyma region. The boundary of ROIs were defined to avoid any error due to chemical shift artifact.

3.2.6 Measurement of mean diffusivity (MD)

Mean diffusivity (MD) was measured using Matlab (Mathworks, Natick, Massachusetts, USA). Details of the Matlab coding can be found in the Appendix). Diffusion tensor model was fitted voxelwise and calculation of MD was performed in ROIs drawn manually in MR slices. MD in sub-structures of the tissue was measured as:

$$MD = (\lambda_1 + \lambda_2 + \lambda_3)/3 \hspace{3cm} [3.1]$$

where λ_1 , λ_2 and λ_3 are the eigenvalues of the diffusion tensor matrix. ROIs for MD calculation were defined based on MR slices that showed distinct anatomical features and closely matched the corresponding histological sections. ROIs were manually drawn on MD images around tissue sub-structures. A color printed images of H&E stained tissue under light microscopy view from Aperio Image Scope software were used as reference. ROI voxel calculations were based on selection of imaging slices that most clearly permitted unequivocal manual selection of a large area of voxels composed primarily tissue sub-structures (parenchyma and capsule). The boundary of tissue sub-structure and histopathological status of the tissue on the selected ROIs were confirmed by an expert pathologist (Dr Geoff Watson) and drawn on the color printed images of H&E slices. Each sub-structure was visually matched to the appropriate ROI in MD images using the drawn map on histology images as guides. The ROI boundary on MD images was defined to avoid any error due to chemical shift artefact. This ensured region correspondence between pathologic and MRI analysis. Adjacent MR slices were checked to minimize partial volume effects. ROIs in both MD images and histology section were align at the approximately same image plane and slices as described in Section 3.2.5. An example of ROI selection on MD image is shown in Figure 3.3.

For each MRI-histology image pair the same ROI selection method was repeated on the adjacent MR slices. MD was measured as an averaged diffusivity value of the same ROI from three adjacent MR slices. For ROIs adjacent to fat, the boundary was defined to avoid any chemical shift artefact. Normal tissue ROIs were selected to exclude inflammation and hyperplastic tissue. Metastatic lymph node ROIs were defined to exclude reactive and normal tissue.

3.2.7 Measurement of cellularity metrics

Slide scan images (n=303) were obtained from 16 subjects. A region containing exclusively microstructures of lymph node, capsule, or parenchyma were identified and selected in each scanned slide image. A total of 117 slide scan images were identified as normal lymph node, 138 as metastatic lymph node, and 48 as Non-Hodgkin lymphoma. Measured cellularity metrics included nuclear count and nuclear area. The measurements were performed using Image Pro Premier (Media Cybernetic, Rockville, MD) with semi-automatic segmentation. The 'Smart Segment' tool was utilised to segment the nuclei based on colour intensity, morphology and background. The 'Split' function, which is based on a circular boundary condition, was employed to distinguish nuclei that appeared joined. Nuclear counting was then performed with the 'Count' tool. A minimum nucleus area of 10 pixels (nuclear diameter ~7 μm) was selected to exclude the counting of spurious small objects. The 'Create mask' tool was used to create a mask with nuclei in yellow against a black background. The subimages as explained in section 3.2.4 saved in PNG format and were imported to Image Pro Premier software for cellularity metric measurements. The measurement of cellularity metrics on each defined ROI on subimages was repeated three times and the averaged value was reported. An example of the automated segmentation results is shown in Figure 3.4.
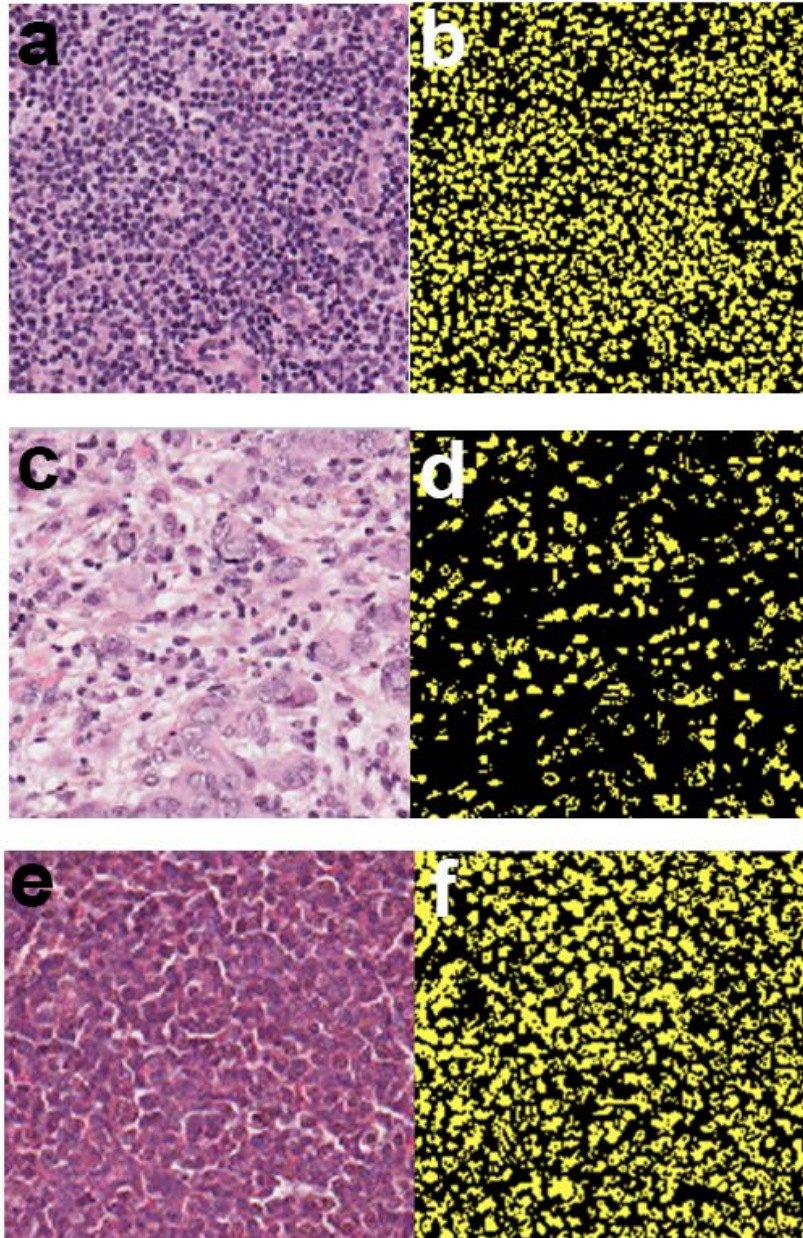
Figure 3.4 Semi-automated nuclear segmentation

Nuclei were segmented for estimation of cellularity metrics using semi-automated segmentation software. The LEFT column shows H&E stained section images for normal node (a), metastatic node (c), and Non-Hodgkin lymphoma (e). The RIGHT column shows corresponding nuclei segmentation (b), (d), (f) for each section.

3.2.8 Statistical analysis

SPSS, version 21.0 (IBM Corporation, Armonk, New York, USA), was used for statistical analysis. Data normality was confirmed by Shapiro-Wilks test with $p > .05$. The differences between means were assessed by Kruskal-Wallis with *post hoc* Dunn-Bonferroni test for multiple groups. To adjust the clustering effect due to repeated measures, the mean value of the measured metric for each tissue type was used in the analysis.

Pearson's correlation coefficient was used to measure the correlation between MD and cellularity metrics. Spearman's rank was used to assess the correlation between MD with the cellularity metric in three different tissue types (metastasis, normal, lymphoma). Fisher r-z transformation (z-score) was used to determine significant ($p < .05$) difference between correlations.

3.3 Results

3.3.1 Lymph Node Microstructures

DWI displayed tissue contrast corresponding to distinct sub-structures in lymph node tissue including capsule, parenchyma, and artery (Figure 3.5). Microstructures that were present in DWI images corresponded closely to histology features seen on light microscopy of the same tissue slices. In the DWI images of normal and metastatic lymph node tissue (Figure 3.5b and 3.5e), the parenchyma biophysical was hyperintense relative to the surrounding tissue microstructures. In the corresponding MD images (Figure 3.5c and 3.5f), the parenchyma biophysical showed distinctly lower diffusivity than the adjacent capsule.
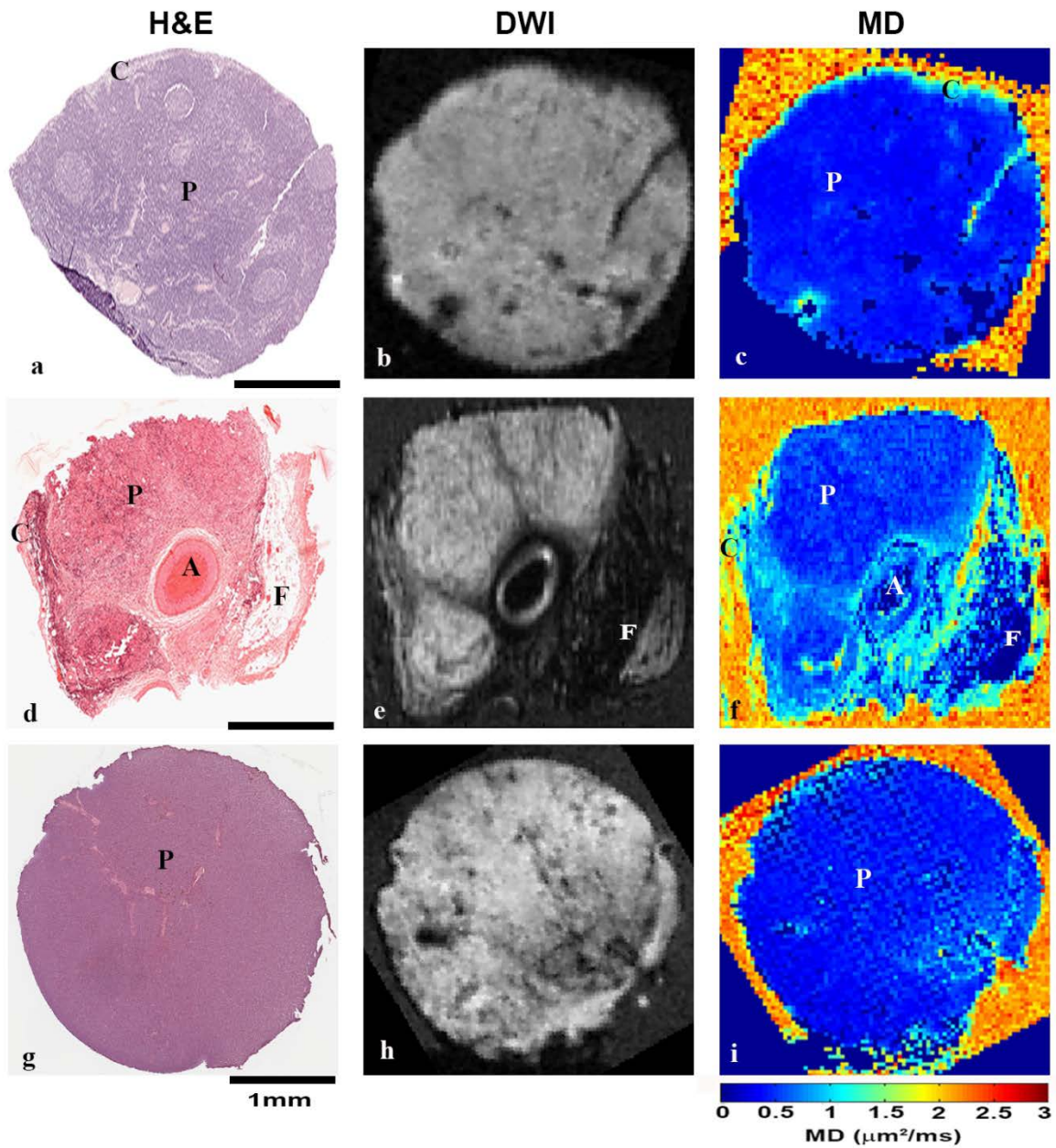
Figure 3.5 Diffusion properties of lymph node microstructures

Representative H&E-stained sections, DWI images, and MD maps of lymph node tissues. a–i: H&E histology section of normal lymph node tissue (a) shows the capsule (C), parenchyma (P), and fat (F). d–f: H&E histology section of metastatic lymph node tissue (d) depicts capsule (C), parenchyma (P), and artery (A). g–i: H&E histology section of lymphoma (g) shows parenchyma (P). In d, e, f there were fat (F) present in the nodal tissue. The features seen in the tissue in the H&E histology section corresponded directly with those seen on the DWI images (b, e, f) and MD maps (c, f, i) in approximately the same plane.
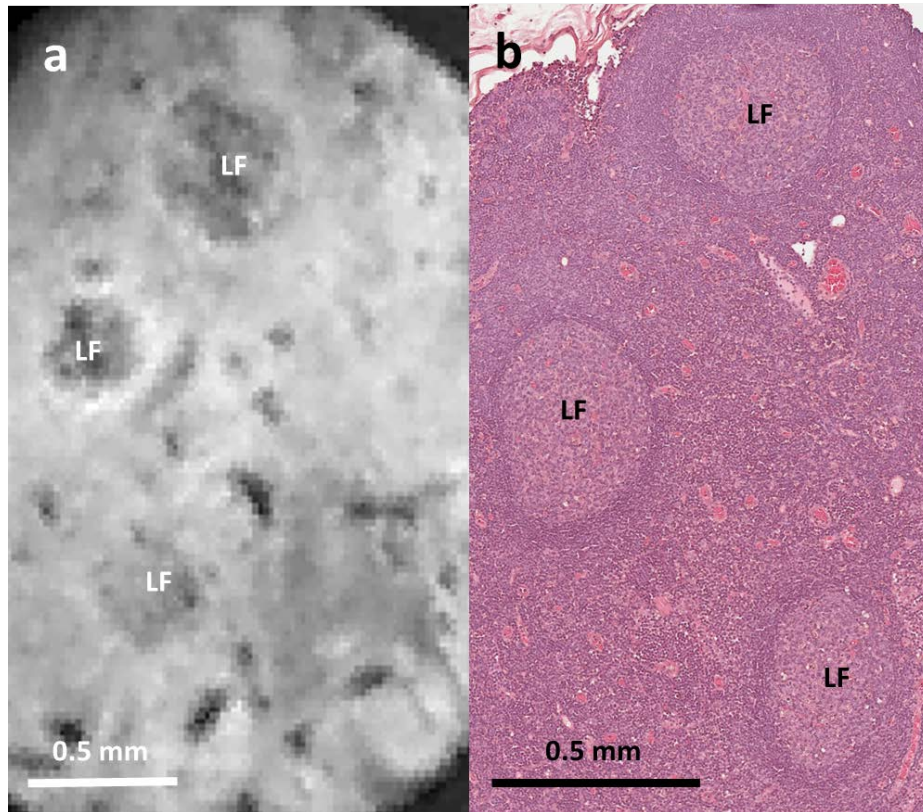
Figure 3.6 Normal lymph node with folicular hyperplasia

Normal tissue sample in Figure 3.6 shows hyperplasia of lymphoid follicles (LF) in DW images (a) and the approximate tissue sectioning in H&E stained slide (b). The rim of the lymphoid follicles as seen in the H&E stained slide contains a higher density of cells and closely corresponded to distinct hyperintense signal on DWI images.

3.3.2   Image alignment accuracy

The MRI-histology image alignment accuracy was not quantified. ROIs in both MD images and histology section were align at the approximately same image plane and slices as described in section 3.2.5. Multiples MD images were subjectively assessed at depth separation from 50 - 200µm to match with one histological section. Adjacent MR slices were checked for discrepancy and to minimize partial volume effects. ROIs in both images are inapproximate as in 16.4T diffusion-weighted MR images had a voxel size used (40 µm isotropic) while the thickness of the histology section is 5 µm. However, the method used allowed the matching of MRI to lymph node sub-structure details and histopathology with sufficient confidence for an ROI-based analysis.

3.3.3 Mean diffusivity (MD) analysis

Twenty samples of lymph node tissue were collected from 16 subjects. In this study, 107 histology sections were analysed, of which 21 sections were excluded due to poor staining and folding of tissue on the slide. Diffusion parameters were analysed and measured using Matlab. The MR images were displayed using MIPAV for 3D volume rendering and Matlab for 2D images.

Shapiro-Wilks test showed that MD for metastatic and normal tissue deviated from normal distribution with $p > .05$. For lymphoma, the MD showed normal distribution with $p <.05$. The results of Shapiro-Wilks test showed a non-normal distribution of the overall data in this study. Therefore, the subsequent statistical analysis was based on non-parametric testing.

In this study, the two main sub-structures of lymph node tissue, parenchyma and capsule, were included for measurement of mean diffusivities. The difference of MD in sub-structures of the three pathological lymph node tissue types was assessed using a Kruskal–Wallis test. Any significant differences of MD among the tissue types were then assessed using *post hoc* Mann–Whitney analysis. Results of the Kruskal–Wallis test and *post hoc* Mann–Whitney analysis are presented in Table 3.3. Distinct diffusivity was found in node sub-structures, while higher diffusivity was found in the capsule region than in parenchyma.

A summary of the MD in each identified lymph node sub-structure is presented in Table 3.3. The MD was significantly lower ($p <.05$) in cancerous tissues in comparison to normal tissues. Distinct diffusivities were also found in lymph node sub-structures. Higher diffusivity was found in the capsule in comparison to parenchyma in normal and metastatic lymph node tissues. Parenchyma in normal lymph node tissues had higher MD (0.71 ± 0.17 μm^2/ms) than metastatic parenchyma (0.52 ± 0.08 μm^2/ms) and lymphoma (0.47 ± 0.19 μm^2/ms). Capsule in normal node tissues showed a higher MD (1.15 ± 0.16 μm^2/ms) than capsule in metastatic tissues (1.07 ± 0.17 μm^2/ms).

A significant difference was seen in MD values of lymph node sub-structures in the three different tissue types using Kruskal–Wallis test with $p <.05$. The Kruskal-Wallis test indicated a statistically significant difference of MD values in parenchyma in the three tissue types, $\chi^2(2) = 6.129$, ($p = 0.047$) with a mean rank of MD 34.44 for metastasis, 40.96 for normal and 25.44 for lymphoma. The *post hoc* Mann–Whitney analysis showed differences in MD of sub-structures in normal and lymphoma tissue types ($p >.05$).

The bar graph in Figure 3.7 shows the summary of MD measured for lymph node sub-structures for all subjects. It has to be noted that not all subjects showed the presence of lymph node sub-structures in this study. Only five subjects had both measurements on parenchyma and capsule. The bar graph shows that the capsule of the lymph nodes generally appears to show higher MD compared to parenchyma in all subjects. Parenchyma of normal lymph node shows higher MD compared to normal and lymphoma tissues. An exceptionally high MD in parenchyma of normal tissue was identified in two subjects (5&6).

Table 3.3 Summary of Mean Diffusivity (MD) in Lymph Node Sub-structures

Microstructure	Tissue type	MD (µm²/ms) [a]	ROI (voxels) [b]
Parenchyma	Normal Tissue	0.71 ± 0.17	78 (46,218)
Parenchyma	Metastatic Tissue	0.52 ± 0.08	75 (26,412)
Parenchyma	Lymphoma Tissue	0.47 ± 0.19	54 (24,245)
Capsule	Normal Tissue	1.15 ± 0.16	6 (686)
Capsule	Metastatic Tissue	1.07 ± 0.17	54 (10,953)

Kruskal Wallis test
(significant difference between MD in lymph node microstructures)

	Chi-Square	Degrees of freedom	p	Mean rank[c] Normal Tissue	Metastatic Tissue	Lymphoma Tissue
Parenchyma	6.129	2	0.047	40.96	34.44	25.44
ROI				25	28	16
Capsule	0	1	1	10.5	10.5	-
ROI				2	18	-

***Post hoc* Mann- Whitney test**
(significant difference between measurad MD in lymph node microstructures)
95% confidence intervals

Microstructure	Tissue type pairwise	U	p
Parenchyma	Metastasis - Normal	282	0.226
Parenchyma	Metastasis - Lymphoma	146	0.149
Parenchyma	Normal - Lymphoma	125	0.016
Capsule	Metastasis-Normal	18	1

a. mean ± standard deviation reported
b. number of voxels used in the data set after adjusting for clustering effect due to repeated measures. Total number of voxels analysed in brackets.
$p < .05$ for all cases.
c. Mean rank is the group with the greatest number of the score (highest or lowest). Scores in the test are ranked from lowest to highest (133).
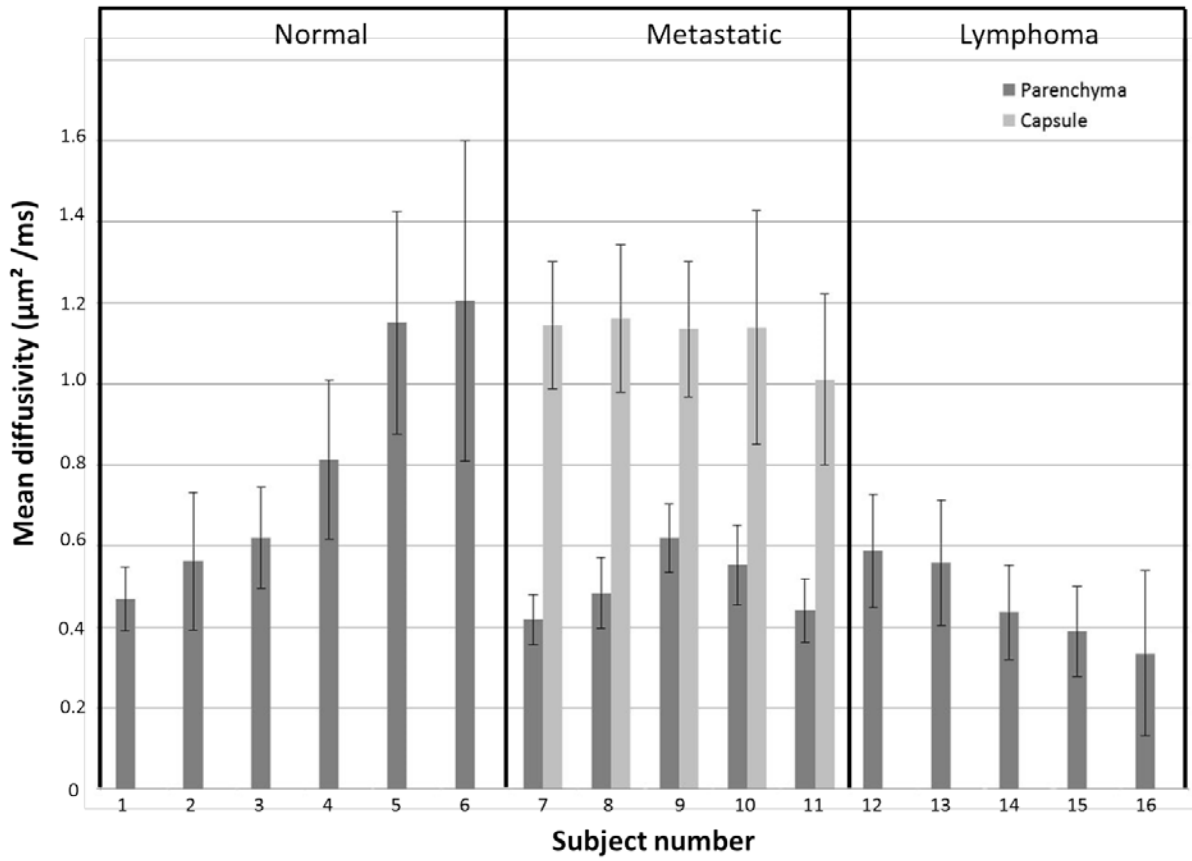
Figure 3.7 Summary of mean diffusivities measured from ROIs shown in each subject.

Mean diffusivities for parenchyma and capsule of lymph nodes were measured on a total of 16 subjects. The error bar represents the standard deviation of each measurement.

3.3.4 Cellularity metrics analysis

Kruskal-Wallis H-test with *post hoc* Dunn-Bonferroni revealed a significant difference between cellularity metric and types of lymph node tissue. The results shows that nuclear count had $\chi^2(2) = 42.488$ with a $p < .05$ and a mean rank of 52.54 for normal, 16.64 for metastatic and 33 for lymphoma tissue. The results for shows nuclear area had $\chi^2(2) = 42.799$ with a $p < .05$ and a mean rank of 53.61 for normal, 18.52 for metastatic and 28.19 for lymphoma tissue.

It should be noted that aligning MR images with the corresponding histology tissue slices can be challenging, especially when the tissue has not been cut perpendicular to the MRI axis. Misalignment may still occur even though pre-cut tissue slices with equivalent depth had been provided as a guide to the operator. There were some uncertainties in aligning the ROIs used for measurement of MD with the corresponding ROIs defined in the histological sections. This problem is not unique to the method described here, and such uncertainties would have been greater in earlier studies comparing ADC measured in-vivo with cellularity metrics (100,108,134). The alignment method in the present study was done qualitatively, it would be desirable to use a spatial transformation in Matlab code using 3D rotation and linear interpolation to obtain oblique MR slices to match more closely with the histology tissue slices for future work.

3.3.5 Correlation of cellularity metrics with mean diffusivity

Table 3.4 summarises the measurements of mean diffusivity (MD) and cellularity metrics, which included measurements of nuclear count and nuclear area. The Shapiro–Wilks test was used to test the data for normality, and outliers in the data were identified through inspection of the boxplots. The Shapiro–Wilks test showed a MD distribution with a $p < .05$ for metastatic and normal tissues, and $p = 0.293$ for lymphoma tissue. Nuclear counts for all tissue types showed distribution with $p < .05$. Nuclear area distribution for normal tissue had a $p < .05$, while for metastatic and lymphoma tissue $p < .05$. The study concluded that MD and cellularity metrics in the three types of tissue nodes were not normally distributed. Therefore, the assumption of normality was voided and the statistical tests that followed were based on non-parametric tests.

A Kruskal-Wallis test was performed to determine if there were any differences of MD and cellularity metrics in the three types of lymph node tissue (normal, metastatic, lymphoma). Kruskal-Wallis H-test with *post hoc* Dunn-Bonferroni revealed a significant difference in the MD between these three tissue types $\chi^2(2) = 6.129$, $p = 0.047$, with a mean rank of 40.96 for normal, 34.44 for metastatic and 25.44 for lymphoma tissue.

Figure 3.8 shows the scatter graphs of cellularity metrics with MD for ex vivo lymph node tissue for *b*-value of 1000 μm^2/ms. A Pearson's correlation was used to assess the correlation between cellularity metrics and MD; the results are summarised in Table 3.4. Nocorrelation was observed between the two independent variables, MD and nuclear count, with $r = 0.368$, n =69 at 95 % confidence intervals. As regards the MD and nuclear area, there was a weak positive correlation, with $r = 0.231$, n =69 at 95 % confidence intervals .

Pearson's correlation test was used instead of Spearman's correlation test to determine if there any correlation between measured mean diffusivity values with cellularity metric in general over ROIs (n=69). Then, a Spearman's correlation test was used to assess a more specific correlation if present between cellularity metrics and MD in the three different tissue types.. The results are summarised inTable 3.5, which shows the significance of difference in Spearman's correlation coefficient with MD (pairwise comparison). All pairwise comparisons showed poor or weak correlation in the normal, metastatic and lymphoma tissue, with $p > .05$. Therefore it was concluded that MD and cellularity metrics were not correlated in the three different tissue types.

	MD (μm^2/ms) [a]	ROI (n)	Nuclear Count (per mm^2) [a]	Nuclear Area (%) [a]	ROI (n)
Normal Tissue	0.71 ± 0.17	28 (84)	11,071 ± 442	22.6 ± 1.4	28 (117)
Metastatic Tissue	0.52 ± 0.08	25 (75)	5021 ± 447	9.5 ± 0.7	25 (138)
Lymphoma Tissue	0.47 ± 0.19	16 (48)	7637 ± 724	11.9 ± 1.0	16 (48)

Table 3.4 Summary of DWI and Cellularity Metrics from Selected ROIs and Measured Correlations

Kruskal-Wallis with *post hoc* Dunn-Bonferroni test
(significant difference between MD and cellularity metrics in three types of lymph node tissue)

	Chi-Square	Degrees of freedom	*p*	Mean rank[c] Normal Tissue	Metastatic Tissue	Lymphoma Tissue
MD	6.129	2	0.047	40.96	34.44	25.44
Nuclear Count	42.88	2	0	52.54	16.64	33
Nuclear Area	42.8	2	0	53.61	18.52	28.19
ROI				28	25	16

Pearson's correlation (r) with MD[b]
(95% confidence intervals)

		Nuclear Count	Nuclear Area
ROIs	69	0.368 (0.107, 0.553)	0.231 (0.018, 0.422,)

a. mean ± standard deviation reported
b. *p* < .05 for all cases.

Spearman's correlation (*r*) between MD[b] and cellularity metrics in tissue type
(normal, metastatic, lymphoma)
(95% confidence intervals)

	Normal Tissue	Metastatic Tissue	Lymphoma Tissue
Nuclear Count	0.098 (-0.327,0.556)	0.145 (-0.334,0.518)	0.171 (-0.449,0.640)
Nuclear Area	-0.349 (-0.638,0.051)	0.256 (-0.210,0.617)	0.476 (-0.065,0.816)
ROIs	28	25	16

a. mean ± standard deviation reported
b. p > .05 for all cases.
c. Mean rank values are used to compare MD and cellularity metrics values in differernt types of lymph node tissue.
d. The highest mean rank value is highlighted (grey cells).

| Table 3.5 Significance of Difference between Spearman's Correlation Coefficient (r) and MD					
Fisher r-z transformation Non-significant differences shaded					
			Normal Tissue	**Metastatic Tissue**	**Lymphoma Tissue**
Nuclear Count	**Normal Tissue**		-	z = -0.16 p = 0.873	z = -0.22 p = 0.826
	Metastatic Tissue		-	-	z = -0.08 p = 0.936
	Lymphoma Tissue		-	-	-
Nuclear Area	**Normal Tissue**		-	z = -2.25 p = 0.024	z = -2.58 p = 0.010
	Metastatic Tissue		-	-	z = -0.64 p = 0.522
	Lymphoma Tissue		-	-	-
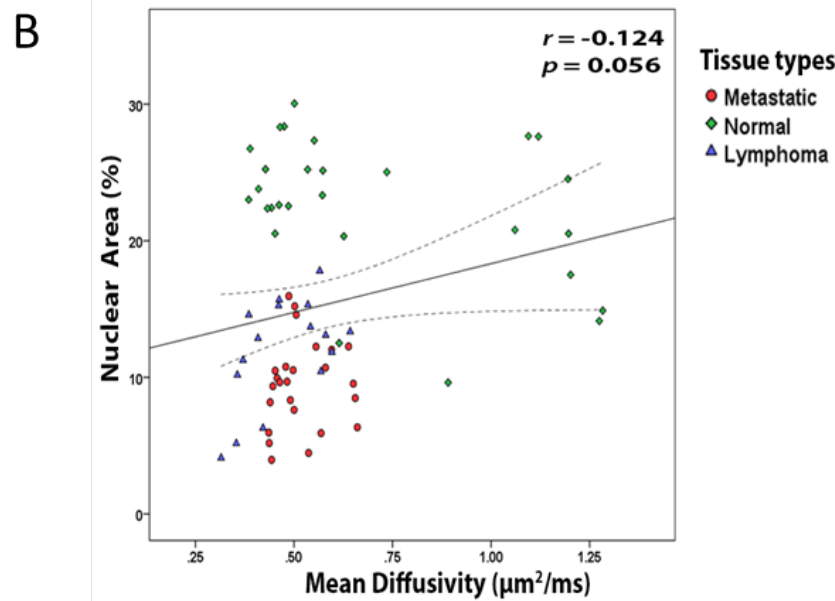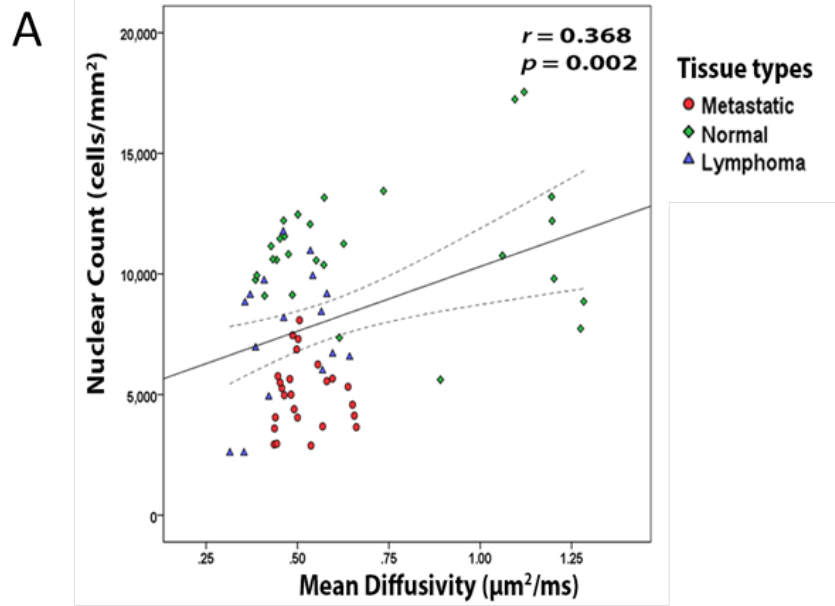
Figure 3.8 Correlation of cellularity and MD in lymph node tissue

Correlation of cellularity metrics (A) nuclear count and (B) nuclear area with MD for ex vivo lymph node tissue. Dotted lines represent 95% confidence interval.

3.4 Discussion

3.4.1 Diffusion compartmentation

This study aimed to investigate the microscopic diffusion properties of lymph node tissue and determine the correlation between diffusivities and cellularity. To the best of our knowledge, it is the first DWI study of lymph node tissue using a spatial resolution approaching cellular scale. The high resolution DWI employed here permits the identification of distinct diffusion properties of lymph node sub-structures. The microstructural changes that alter the relative partial volumes of distinct diffusion components, whether in normal or cancerous lymph node tissue, would be expected to cause significant diffusivity differences when observed in clinical DWI with large voxel volume scale.

Distinct glandular microstructures that are seen in prostate and breast tissues, such as epithelium and lumen, are not present in the lymph node. This is expected as, unlike prostate and breast tissue, lymph node tissue is not a gland tissue. The lymph node is an organ that filters foreign bodies. The microstructures present in the lymph node are unique, differing from those in glandular tissue. The main component of lymph node tissue is parenchyma, which is mainly comprised of small lymphocyte cells supported by a fine stromal meshwork. The capsule is a small portion of stroma that protects the parenchyma from external harm of foreign agents.

The lymph node microstructures that were seen in the DWI and MD images closely matched the structures of histological sections of the same samples seen under light microscopy. There was evidence of distinct diffusivity differences in microstructures of normal and cancerous lymph node tissues. Findings from the present study were consistent with the recent report of distinct diffusivities in prostate and breast tissue sub-structures (2,9).

With regard to the normal parenchyma, the DWI of lymph node tissues revealed variation in MD values although the tissues are normal. It is noteworthy that during tissue preparation, tissue samples showed differences in their physical appearance. Differences in the hardness of the tissues were noted. A soft tissue showed low diffusivity values between 0.4 - 0.6 $\mu m^2/ms$, whereas the diffusivities of a dense normal tissue could reach up to 1.2 $\mu m^2/ms$. A high MD was found in normal lymph node tissue from two subjects. Histopathological

assessment of these two normal lymph node tissues showed the presence of multiple hyperplasia of lymphoid follicles (LF) in the normal tissue, as presented in Figure 3.6. The rim of the follicles in the normal tissue, which shows as a hyperintense area in DW images, indicates highly restricted or hindered water diffusion in this region. The hyperintense DWI region corresponds directly to the rim of the folicles in the normal tissue seen under light microscopy. Under microscopic view, the rim of the follicles in the normal tissue was found to contain a higher number of nuclei. Tissue histopathological analysis have shown evidence of distinctive MD values in two types of normal tissue. Therefore, the differentiation of nodal disease based on DWI at clinical spatial resolution without histopathological analysis should be intrepreted with more caution to avoid mis-diagnose.

The characterisation of lymph node diseases using DWI at clinical spatial resolution ranging from 0.5 m$\mathbf{m^3}$ to 3.0 m$\mathbf{m^3}$ is of radiologic interest. The present study has demonstrated that differentiation of metastatic from nonmetastatic lymph node tissues that solely based on diffusivity values is challenging, although the study was conducted at spatial resolution approaching cellular level. At the current level of understanding, the translation of diffusion imaging at cellular level to the clinical spatial resolution requires more vigorous and intense research.

Qualitatively, the alignment method used in the present study showed a sufficient confidence for an ROI-based analysis to satisfactorily fulfill the purposes of the study. The alignment between MR images and corresponding histology sections was in only approximately the same plane due to tissue geometrical distortions. It was particularly challenging to align the histology sectioning images with the corresponding MRI images in the same plane when the tissue samples were not neat solid cylinders. It would be desirable to quantitatively measure the alignment between MR images and corresponding histology sections.

3.4.2 Cellularity metrics

Cellularity metrics were measured in 107 histological images from 16 subjects. The number of histological images being analysed was three times greater than in a previous study on cellularity in lymph node tissue (103), which only focused on one type of lymph node tissue. The present study, by contrast, explored diffusivity in three types of lymph node tissue—normal, metastatic and lymphoma. In this study, the nuclear count for lymphoma tissue was

three times higher than that found in the previous study (103). The lower number of nuclear count in the previous study might explained by definition of cellularity used in the studies. Cellularity was measured as number of cells per images view ($\times$20 objective) in previous study , while in the present study cellularity was measured number of cells per unit of area of maximum of 3 mm in diameter in each histological slices. To date, no study has investigated the nuclear area in lymph node tissue.

The measurement of cellularity metrics in this study focused on the parenchyma of the lymph node tissue. This is because most of the cell interactions take place in the parenchyma, which contains a higher concentration of lymphocyte cells (32,33). Therefore, the measurement of cellularity in the parenchyma is likely to provide a better representation of biophysical activity in the lymph node tissues compared to other sub-structures.

Using the Spearman's correlation test, this study found correlation between measured MD and cellularity metrics in each types of nodal tissue including normal, metastatic and lymphoma. The results clearly indicated no correlation between cellularity metrics and mean diffusivities in the three lymph node tissue types. The no correlation between cellularity metrics and mean diffusivities is in agreement with a previous study (103). The results are similar to the findings from recent ex vivo study on prostate tissue, which showed that diffusivity correlated better with gland components than with cellularity (93).

The results from this study are also in agreement with those from a previous study on prostate tissue, in which normal tissue had a lower nuclear count than cancerous tissue (93). Nonetheless, this study found that the measured cellularity was higher in lymphoma compared to the previous study. A similar number of measured cellularity was also found in both normal and lymphoma tissues. Although lymphoma is a disease, the nuclear count per unit of area was higher than in the metastatic tissue. A possible explanation is that lymphoma has distinct clinicopathological criteria; it contains cells that are morphologically and immunologically similar to the nuclei in normal tissue. The neoplastic cells in the lymphoma predominantly consist of small- to medium-sized cells of B-lymphocyte origin (135). On the other hand, metastatic tissue is composed of large-sized neoplastic cells that are confined in a nested cluster (31). Therefore, the nuclear count was higher in lymphoma than in metastatic tissue, as shown in Table 3.4.

In general, the nuclear count for lymph node tissue is twice the count in prostate tissue (93). Consequently, segmentation for nuclear counting is challenging and should be conducted more carefully for lymph node tissue. In other words, a greater number of cells should be measured on the 3mm diameter tissue. The software tended to take a longer time to complete the segmentation of the entire area. Due to the higher numbers of pixels to be measured, further modification of the segmentation would likely result in failure of the analysis procedure . Future work should assess the entire histological tissue slice to minimise preparation error or staining error. The absence of these errors in the region of interest would increase the efficiency of the nuclei segmentation procedure for cellularity measurement.

It is recommended that a high-resolution widescreen monitor be used to provide high contrast image viewing for cellularity measurement. Viewing conditions are important to a successful segmentation process. Better viewing conditions may fascilitate and simplify the selection of high contrast nuclei from the background in the histology tissue section.

In the present study, the alignment between MR images and corresponding histology sections was crucial. Better alignment is necessary to ensure that the diffusion contrast corresponds closely to the microstructures of the tissue sample. Alignment can be improved by providing a depth histology section (pre-determine location to guide sectioning process) before the tissue cores are cut. The depth given prior to sectioning will provide an indicator for improving alignment of the MR images with the diffusion contrast of the tissue. It is noteworthy that some of the tissues were not sectioned perpendicular to the image planes. This created significant challenges in aligning the histology sections to the MR images.

3.4.3   Correlation of cellularity metrics with mean diffusivity in pathologic lymph node tissue

The results show that, in both cancerous and normal lymph node tissue, correlations between cellularity and MD were non-existent. In this context, it is worth mentioning that the histological grading system is based on tissue architecture rather than cell density per se. Thus, the common attribution of reduced MD to 'higher cellularity' is not inherently

consistent with the histological grading system although MD tends to decrease with metastatic nodes.

Increased cellularity is regularly cited in the literature as the main cause of reduced ADC values. Recently, however, the assumptions used to support this argument have been challenged because they lack biophysical evidence that increased cell density causes the decrease in ADC values in prostate tissue(93). In histology, cellularity is defined as the number of cells counted per unit of area (with the assumption of fixed low intracellular diffusivity and membrane permeability). The cells are assumed to displace and reduce the signal contribution of a pool of freely diffusing extracellular water. It should be noted that the earlier assumptions are more complex for biological tissue. Biological tissues contain heterogeneous microcomponents, which will eventually affect the overall water diffusivity in the tissue. It is worth noting that for metastatic nodes, the cells are much larger than the nucleus, so the nuclear area is not a good proxy for cellular area.

3.5 Conclusion

Distinct diffusivity tissue components were seen in lymph node sub-structures and no significant difference was shown in cellularity metrics (nuclear area and nuclear count). The correlations of mean diffusivity with cellularity metrics in the three types of lymph node tissues were non-existent. This study represents the first step in understanding the biophysical characteristics of the tissue biophysical properties underlying the variation in diffusivity values reported in the literature for lymph node tissue.

4. Diffusion Modelling and Model Ranking with Information Criteria

4.1 Introduction

The ADC is commonly used in clinical DWI studies to compare non-cancerous and cancerous lymph node tissue. The ADC approach assumes a Gaussian water displacement probability but this assumption is invalid in the heterogeneous environment of biological tissue. Previous literature shows a wide variation in reported ADC values between cancerous and non-cancerous tissue (15,83,84). This highlights the limitation of the simple ADC model in describing tissue changes based on its histological features. Recently, a three- biophysical model called VERDICT (Vascular, Extracellular, and Restricted Diffusion for Cytometry in Tumours) has been used to model tissue components based on their histological features (127). To describe the non-vascular water pools, VERDICT modelling of prostate tissue includes unrestricted and restricted isotropic components (129), but diffusion anisotropy has been neglected. Recently, VERDICT was also successfully used to distinguish benign from malignant tissue in colorectal (127) and prostate tissue (129).

A recent ex vivo study on prostate tissue using VERDICT demonstrated higher information content using Akaike Information Criterion (AIC) ranking of anisotropic and restricted multi-component models in comparison to the ADC model and other unrestricted models (4). This finding suggests that the application of more sophisticated models may improve the performance of DWI in clinical studies. Motivated by the successful implementation of biophysical models in prostate tissue, this chapter describes a similar investigation in lymph node tissue. Biophysical modelling is not yet widely employed instudies of non-neural tissue.

This study investigated the non-perfusion components of the VERDICT model by comparing the theoretical information content of biophysical models that include anisotropic components. The objective was to compare the theoretical information content of single and multi -biophysical models of DWI signal attenuation, measured over an extended range of *b-*

values and multiple diffusion times in lymph node tissue. In the present study, it is assumed that there is no water exchange between the compartments.

4.2 Methods

4.2.1 Materials

Lymph node tissue samples were collected from humans and animals.

Human tissue samples

The study was conducted with ethical approval from Concord Hospital (Sydney, New South Wales), and written consent from all participating patients. A copy of the institutional ethical approval can be found in the Appendix. The lymph node tissue was collected from inflammatory bowel disease surgery and the specimens were immersed in 10% neutral buffered formalin post-surgery to preserve the specimens. Mesenteric node tissue was collected from patients aged 50-60 (mean 55) years. Between April 2014 and April 2016, a total of two normal lymph node tissues were collected from two patients; a minimum of one and maximum of five lymph nodes were resected from each patient. The mean short axis diameter of the specimens was 5 mm (range 3-8 mm). The mean long axis diameter was 5 mm (range 3-10 mm).

Animal tissue samples

Dog lymph node tissue was collected from Vetnostics(Sydney, New South Wales) and the specimens were immersed in 10 % neutral buffered formalin post-surgery. A copy of the institutional ethical approval can be found in the Appendix Between August 2015 and April 2016, one metastatic lymph node sample were collected from a dog. The mean short axis diameter was 5 mm (range 3-10 mm). The mean long axis diameter was 8 mm (range 3-15 mm).

4.2.2 Tissue preparation

Excess fat around the lymph node was carefully trimmed using a surgical scalpel blade. The tissue samples were glued to a plastic strip, as shown in Figure 4.1. The glued samples were inserted into a screw-top plastic vial and immersed in phosphate-buffered saline (PBS) containing 0.2 % v/v Magnevist (Bayer Healthcare Pharmaceuticals, Berlin, Germany). They were then stored at least overnight at room temperature to wash out the formaldehyde. The PBS solution provides a known diffusivity background and the contrast agent reduces T_1 to ~0.5 s, which enables a shorter TR and, thus, faster imaging. The samples were then taken to the Lowy Cancer Research Institute, University of New South Wales, for imaging at 9.4T.

Figure 4.1 Tissue samples on plastic strip for imaging at 9.4T

Three lymph node tissue samples collected from three subjects were set for imaging at 9.4T: top is metastatic node (blue dyed), middle and bottom are normal nodes.

4.2.3 MR imaging

The following specimen preparation and MRI setup was performed by Dr. Andre Bongers at Lowy Cancer Research Institute, UNSW.

The imaging was performed on a 9.4T Bruker Biospec system (Karlsruhe, Germany), which is equipped with 72 mm quadrature RF coils and BGA-12S HP gradients with maximum strength of 660 mT/m and slew rate of 4570 T/m/s. For diffusion-weighted imaging, a 3D spin echo sequence was employed and imaging was performed at a monitored room temperature (22°C). Parameters are listed in Table 4.1.

The diffusion signal attenuation was measured in three orthogonal directions. The 6-direction data with single b-value and single δ/Δ value were acquired to enable the fitting of anisotropic components. All the diffusion-weighted measurements were preceded by the acquisition of two reference '$b = 0$' images. The intrinsic signal-to-noise ratio (SNR) was measured from the ratio of the signal S, which is the mean signal intensity in a large region of interest (ROI) manually drawn inside a the nodal slice, relative to the noise level N, which is the standard deviation of the difference between the ROI voxel values in the two reference '$b = 0$' images(136).

Table 4.1 DWI Acquisition Parameters	
FOV (mm^2)	35×35
Matrix size	64×64
Voxel size (mm^3)	0.5×0.5×0.5
SNR	70
TR (ms)	2000
TE (ms)	22, 29, 49, 89
δ (ms)	5
Δ (ms)	10, 20, 40, 80
b-value (s/mm^2) 6 directions	800[a], 1600[a]
b-value (s/mm^2) 3 directions	100, 311, 603, 965, 1391, 1873, 2411, 3000
a) Nominal *b*-value. Effective *b*-values were used for model fitting.	

4.2.4 Histopathology: Morphology segmentation

Following MR microimaging, the tissue cores were prepared for light microscopy. The tissue samples were sectioned and stained with haematoxylin and eosin (H&E) at the Lowy Cancer Research Institute, University of New South Wales, with the kind assistance of Dr Carl Power. Histopathology examination of the H&E stained slides was performed by a histopathologist (Dr Geoff Watson) at the Department of Tissue Pathology and Diagnostic Oncology, Royal Prince Alfred Hospital (RPAH). The sub-structures, border of each sub-structure and the cancer type of tissue were then identified and recorded on A4 paper colour prints of tissue sections.

H&E stained slides were digitally scanned at 40× magnification with a spatial resolution of 0.25 microns per pixel using a digital brightfield microscope (Aperio Scan Scope, Leica Biosystems Imaging Inc., Wetzlar, Germany). Images from the digital scanner were stored online via Aperio eSlide Manager (version 12.2) software in scope virtual slide (SVS) format. SVS image files were viewed offline using Aperio Image Scope software (v12.10.5029). The "Zoom Navigation" and "Extract Image Region" tools were utilised to select subimages containing only the 3 mm core tissue. Typically, the scanned 3 mm diameter lymph node tissue sections were 11000×14000 pixels. The subimages were saved in lossless Portable Network Graphics (PNG) format for cellularity measurement.

4.2.5 Model description

The eleven models used in this study were combinations of isotropic, anisotropic and restricted components. The models were tested on three lymph node samples comprising normal and metastatic lymph node tissue.

The lymph node tissue was modelled with a combination of up to three components, which were described according to the taxonomy used for brain tissue DWI in [23]. Five candidate components were identified (see Table 2.4 in Section 2.3): 1) a Tensor, which is a conventional DTI model providing two commonly used parameters, FA and MD (137); 2) a Zeppelin, which is a cylindrically symmetric tensor that also provides FA and MD; 3) a Ball, which is an isotropic tensor and equivalent to the ADC model; 4) a Sphere, which describes

76

water molecules diffusing inside an impermeable pore with a non-zero radius; and 5) a Stick, which assumes that water diffusion is in an idealised cylinder with zero radius. In total, eleven models were considered, as listed in Table 4.2. Single component models were used to describe ADC(Ball), biexponential (Bi-Ball) and DTI (Tensor). DTI can be used to measure parameters that refer to experimental but not a model. For instance, Zeppelin models appears to look like a DTI model but with cylindrical symmetric . A mixture or multi-components models were used to describe biophysical properties underlying diffusion contrast of the tissue which includes hindered and restriction components. Multi-components models with anisotropic and unrestricted (with the Zeppelin components), while isotropic and restricted (with the Sphere components).

Table 4.2 Fitted Models			
Name	**Components**	**Fitted parameters**[a]	**No. parameters**
Ball (ADC)	Ball	D	1
Bi-ball	Ball + Ball	$f_1\, D_1\, D_2$	3
Ball-sphere	Ball + Sphere	$f_1\, D_1\, D_2\, R$	4
DTI	Tensor	$D_{||}\, D_{\perp 1}\, D_{\perp 2}\, \theta\, \phi\, \alpha$	6
Ball-zeppelin	Ball + Zeppelin	$f_1\, D_{||}\, D_{\perp}\, \theta\, \phi\, D$	6
Zeppelin-sphere	Zeppelin + Sphere	$f_1\, D\, R\, D_{||}\, D_{\perp}\, \theta\, \phi$	7
Ball-tensor	Ball + Tensor	$f_1\, D_{||}\, D_{\perp 1}\, D_{\perp 2}\, \theta\, \phi\, \alpha\, D$	8
Bi-ball-zeppelin	Ball + Ball + Zeppelin	$f_1\, f_2\, D_1\, D_2\, D_{||}\, D_{\perp}\, \theta\, \phi$	8
Bi-zeppelin	Zeppelin + Zeppelin	$f_1\, D_{||1}\, D_{\perp 1}\, \theta_1\, \phi_1\, D_{||2}\, D_{\perp 2}\, \theta_2\, \phi_2$	9
Tensor-sphere	Tensor + Sphere	$f_1\, D_{||}\, D_{\perp 1}\, D_{\perp 2}\, \theta\, \phi\, \alpha\, D\, R$	9
Ball-stick-sphere	Ball + Stick + Sphere	$f_1\, f_2\, D_1\, D_2\, \theta\, \phi\, D_3\, R$	8

a) Signal normalised before fitting ($S_0 = 1$). Sum of signal fractions $f1 + f2 + fn = 1$. D is diffusivity, $D_{||}$ is tensor parallel diffusivity, and $D_{\perp}$ is tensor perpendicular diffusivity. θ, ϕ and α are tensor angles. R is sphere radius.

4.2.6 Model fitting and ranking

The fitting and ranking of the models was performed by a Dr. Sisi Liang at Victoria University, Melbourne (138).

The study used multiple *b*-values and multiple diffusion times to produce a rich MR data set, as well as to ensure stable fitting (127). Multiple diffusion times were applied to the 3-direction MR data to allow the estimation of a restriction radius. Single *b*-value and single δ/Δ were applied to the 6-direction MR data to allow the fitting of anisotropic components. Each of the models listed in Table 4.2was fitted to the 3- and 6-directions MR data using a Levenberg-Marquard minimisation algorithm in the open source software CAMINO (139). Fitting of the models was carried out based on the minimisation of an objective function. Minimisation of an objective function uses an offset-Gaussian noise model to account for the inherent Rician distributed noise in the magnitude MRI data. (127). The objective function is measured as the sum of squared errors:

$$SSE = \sum_{n=1}^{M} \left(S_n(\delta, \Delta, G) - \widetilde{S_n}(\delta, \Delta, G) \right)^2 \qquad [4.1]$$

where M is the number of measurements, $S_n(\delta, \Delta, G)$ is the signal predicted by the model and $\widetilde{S_n}(\delta, \Delta, G)$ is the signal of the nth measurement. For the sphere component, radius R was constrained so that $0.1 \leq R \leq 20$ μm. The radius was constrained to biophysically meaningful values.

The Akaike Information Criterion (AIC) was employed to rank the models and provide objective quantitative estimation of the models' relative information content. AIC is an estimation of the expected or relative distance between the candidate model and the unknown true system. For hypothesis testing, AIC ranking does not require arbitrary selection of measurement cut-offs. The best model is selected based on the estimation that is closest to the unknown reality. A lower AIC ranking indicates higher model information, that is, less information loss and expected superior performance in model prediction. In DWI of tissue the general definition of the AIC (1):

$$AIC = \left(\frac{SSE}{\sigma^2} \right) + 2p \qquad [4.2]$$

where SSE is the sum of squared errors, σ is the noise standard deviation estimated from a pair of reference images and *p* is the number of model parameters. AIC has a trade-off between bias and variance. AICc is the second-order variant derived from AIC. AICc is recommended when the number of measurements, *n*, is comparable to the number of model parameters, *p*.

$$AICc = \left(AIC + \frac{2p\,(p+1)}{n-p-1} \right)$$ [4.3]

A model is used as an inference for empirical data that are generated from the unknown full reality (1). In this sense, the data helps to determine the proper complexity of the model and justify the effects of estimated parameters for each modelling. It should be noted that small data sets favour simpler models, while large data sets tend to support more complex models. Since the inference is restricted to the specified data set, model comparison across different data sets using AIC is not recommended. Moreover, data sometimes do not support only one 'best' model.

It is worth noting that model selection informs us of inferences from the observed data support, not what full reality might be. Therefore, in some cases several models might show as almost equally best for analysis of the empirical data. The inability to select a single best model is not a weakness of AIC. Rather, it reflects the fact that the data used for modelling are indecisive due to the effect of including estimated parameters in the overall data (1).

4.2.7 ROI selection

A total of 1203 voxels from three lymph node samples were selected for the model ranking analysis. The voxels were obtained from a single slice of MR image that represent the biggest area for ROI of three lymph nodes. The voxels were from manual definition of a mask which excluded non-tissue background data.

4.3 Results

The histopathological examination of the tissue samples showed that samples were metastatic and normal lymph node tissue (Figure 4.2). The normal lymph node tissues were composed

of typical small cells, while metastatic lymph node tissue was composed of distinctive large neoplastic cells.
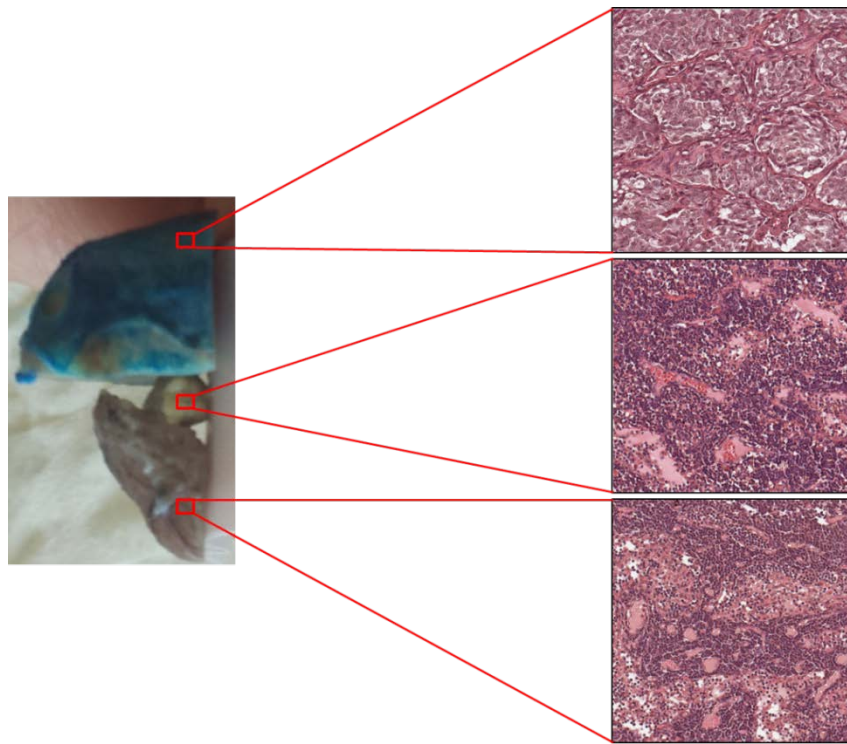
Figure 4.2 Histopathological analysis of lymph node tissue samples

Histology assessment of the three tissue samples shows a metastatic lymph node for top sample (blue dye) and normal lymph node for middle and bottom tissue samples.

Figure 4.3 presents the colour-coded anatomical distribution of the highest ranked models in three lymph node samples and positional variation using AIC rankings for the 11 models. The single- biophysical models, ADC and DTI, were ranked the lowest in all lymph node tissue samples. On the other hand, three multi- biophysical models, which consist of anisotropic and restricted diffusion (Zeppelin-sphere, Ball-stick-sphere and Ball-sphere models) were ranked highest in the majority of voxels of the tissue samples. Ball-sphere model, a model that combines isotropic and restricted diffusion, was ranked close to the three multi- biophysical anisotropic and restricted models. The multi- biophysical models that include anisotropic components were found to contain more information than isotropic models. In addition, multi

-biophysical models that account for diffusion restriction contained a greater amount of information than unrestricted models.

In addition, the results demonstrate that multi-biophysical anisotropic and restricted (Ball-stick-sphere, Zeppelin-sphere and Tensor-sphere) models extract more information from rich data than single- biophysical (ADC and DTI) models and multi-biophysical models that do not account for diffusion restriction. Rich data employed for model ranking were acquired from imaging of tissue samples with multiple b-values and multiple diffusion time. The results are consistent with those from a recent ex vivo study of prostate (4) and lymph node tissue (5).

A

B

Zeppelin- sphere
Ball-stick-sphere
Tensor-sphere
Ball-sphere
Ball-zeppelin
Bi-ball-zeppelin
Ball-tensor
Bi-zeppelin
Tensor(DTI)
Bi-ball
Ball

1   Rank   11
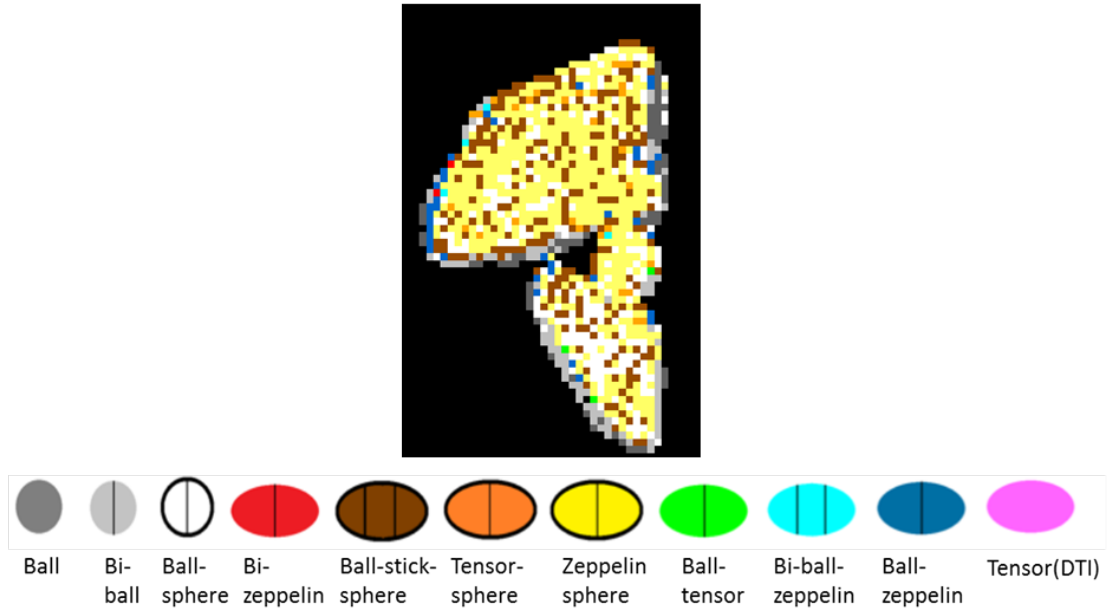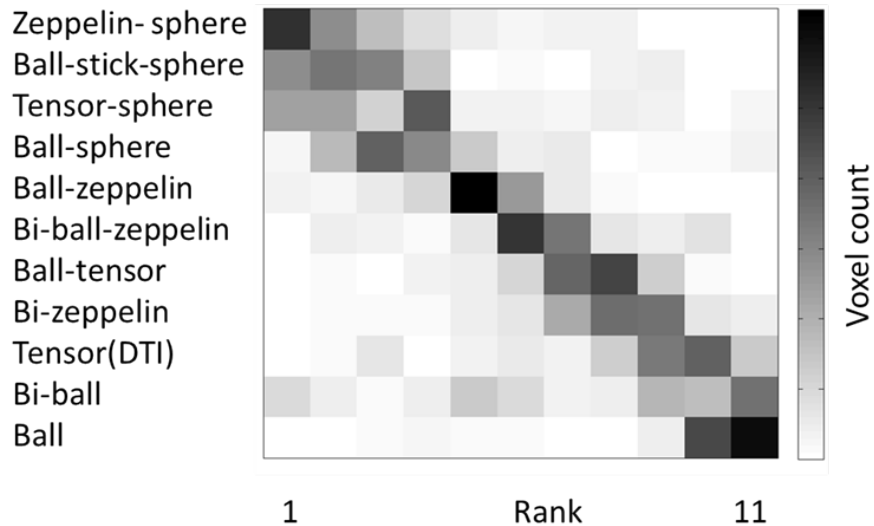
Figure 4.3 Variation of model rankings in three lymph node samples

A) The anatomical distribution of the highest ranked model in a single slice of three lymph nodes. Voxel colour indicates model according to the single and multi- biophysical models. Zeppelin-sphere (yellow) and Ball-stick-sphere (brown) models ranked highest in most voxels in lymphoma and normal lymph nodes. B) Variation in model rank positions. The grey scale indicates the number of times each model ranked at each position. The model is based on subjective assessment of the trends. Data are from 1203 voxels in a single slice of lymph node.

4.4 Discussion

This study provides further information about the non-vascular diffusion environment in ex vivo lymph nodes imaging by comparing 11 different biophysical models. As shown in the fitting models based on AIC, signal diffusion decay in lymph node tissue is non-Gaussian due to tissue complexity.

In clinical DWI studies of lymph nodes for cancer detection, the ADC model has been the most commonly used approach (15,83,84). The inconsistent ADC values reported in the literature highlighted the limitation of the ADC model for DWI imaging of the lymph node. Recently, two studies investigated the feasibility of using the intravoxel incoherent motion (IVIM) model to diffferentiate normal from cancerous lymph node tissue (124,125). These studies showed inconsistent differences between some IVIM model parameters (diffusion coefficient and perfusion fraction) of normal and cancerous lymph nodes. Moreover, the findings revealed the inadequacy of the ADC and IVIM models for diffusion modelling of complex biological tissue. Neither the ADC model nor the IVIM model account for a restricted diffusion component.

The results of the present study showed that multi-component models that account for diffusion restriction provide more information-rich descriptions of multi diffusion times and multi-*b* values in DWI measurements in lymph node tissue than ADC and other unrestricted models. The relatively poor performance of the ADC model and the superior performance of multi-component models in this study suggest that more sophisticated DWI protocols and models may improve lymph node disease imaging. Findings from the present study were consistent with the recent report of multi-component models in in colorectal (127), prostate tissue (4,129) and nodal tissue(5).

The overall AIC ranking in lymph node tissue revealed that single component models, Ball (ADC) and DTI models, had the lowest AIC score. Notwithstanding, the combination of single component model or Bi-ball (biexponential function analysis) also shows the lowest AIC score. Findings from the present study suggest that a more sophisticated model, such as VERDICT, may be more accurate and reliable for DWI- based imaging of lymph node disease. The model ranking of multi-component models that included anisotropy and restricted components using VERDICT demonstrated superior performance to the single

component models. The inclusion of restricted components in this study supported earlier findings on the dependency of molecular diffusion in biological tissues on various restrictions and hindrances (140,141).

Cellularity for the lymph node tissue samples was measured as described in Chapter 3. The mean nuclear count for metastatic lymph node was 3860 ± 568 cells/mm^2, while the normal lymph node was $10,697 \pm 366$ cells/mm^2. The mean nuclear count for normal nodes was twice that of metastatic nodes. Histologically, the metastatic lymph node is composed of a relatively homogenenous population of atypical large cells. Therefore, fewer cells were measured per unit of area in metastatic lymph node tissue than in normal node tissue. The correlation of cellularity with the multi-component analysis could not be assessed because the analysis was based on a small number of samples for each type of node tissue.

A recent related study that investigated the correlation of cellularity with multi-component analysis revealed similar trends in histology and VERDICT cellularity maps of prostate tissue. High cellularity corresponded to cancerous prostate tissue, while lower cellularity was found in benign prostate tissue. The cancerous tissue identified in histology corresponded to regions of high cellularity in VERDICT cellularity maps, while lower cellularity was found in normal prostate tissue (142). It should be noted that the measurement of cellular metrics in lymph node tissue, as seen in Chapter 3, showed contradictory results with those measured in prostate tissue. The cellularity measured in normal lymph node tissue was higher than that in cancerous lymph node tissue. However, the study did not specify the number of samples used. Future work should assess this relationship to understand the changes in diffusion and multi-component analysis with a large number of samples. It is also recommended for future work to include the actual DWI images to allow assessment of the data quality.

The results from the present study showed that the inclusion of restricted and anistropic elements is important in describing the diffusion properties of the tissue. These provide basic scientific evidence that can inform the future development of clinical imaging methods.

4.5 Limitations

This study has several limitations. The results were obtained from a small number of samples for each type of node tissue. Future research should assess the performance of biophysical models in a large number of samples for each type of node tissue.

This study was based on ex vivo diffusion imaging of formalin-fixed tissue that was obtained from a surgical procedure. Formalin was needed to preserve the tissue and stabilise it by protein cross-linking thus permitting long imaging time for ex vivo higher spatial resolutions imaging. Formalin-fixed tissue in ex vivo imaging experiment has been demonstrated to be a stable model for investigating microscopic diffusion properties of prostate tissue (132). DWI using formalin-fixed tissue has shown significant reduction of ADC in all tissue types as compared to results from in-vivo studies (131,132). Nevertheless, the relative diffusion properties of cancerous and normal tissue in ex vivo imaging are similar to those seen in clinical in-vivo prostate imaging.

The analysis of multicomponent modelling in this study was based on diffusion microimaging measurements of formalin-fixed normal and diseased lymph node tissue at 22°C with a shorter diffusion time than is typically used in-vivo. At present, there is only one study investigating multicomponent modelling of fixed tissue in ex-vivo imaging at 37°C(5). Due to the temperature differences for in-vivo imaging, it is important to note that the results of diffusion imaging of fixed tissue should be interpreted with extra caution and also there may be perfusion effect that need to be specified.

The 11 models used in this study assumed that there is no water exchange between the compartments as samples were formalin-fixed tissues . Previous experiments on cultured cells demonstrated that cell membrane permeability may have a significant effect on the model parameters, depending on the diffusion time (143). Hence, future work should include the permeability parameter to account for water exchange between compartments.

4.6 Conclusion

DWI of lymph node tissue in an extended range of b-values and multiple diffusion times demonstrated that multi-component restricted models extract more information than single-component models and multi-component models that do not include diffusion restriction. These findings highlight the importance of including restricted diffusion compartments in modelling diffusion for lymph node tissue.

5. Conclusions

5.1 Summary

In 2018, nearly 3,735,350 new cancer cases were diagnosed in the United States, and there were 609,640 cancer-related deaths (18). Metastasis — the spread of cancer cells to nearby tissue — is the leading cause of cancer-related death (23). One of the earliest events in this process is metastasis to the regional lymph node, and enlargement of the lymph node is a common feature of many solid tumours (17,26). Histopathological analysis, which involves biopsy and invasive tissue sampling, remains the gold standard for diagnosing lymph node disease. However a non-invasive technique, DWI has shown potential for cancer detection and differentiation of cancerous from non-cancerous tissue (2,8,9). The signal from DWI imaging is quantitatively measured using the apparent diffusion coefficient (ADC) value. Considerable overlap of ADC values has been reported in studies using DWI imaging to distinguish nodal diseases (15,16,39,41,48,49,82-86). These findings highlight the lack of understanding of the biophysical basis of tissue diffusion contrast in DWI imaging of nodal tissue.

The present study aimed to define the biophysical basis of contrast in DWI imaging of the lymph node. To the best of our knowledge, this is the first investigation of DWI imaging of lymph node tissue using resolution approaching cellular scales. The first study, presented in Chapter 3, examined the hypothesis that the clinically observed decreased ADC in cancerous lymph nodes could be attributed to increased cellularity. Three types of lymph node tissue — lymphoma, normal, and metastatic — were employed in the study. It was found that the sub-structures seen in DWI images corresponded closely to the histological features seen on the light microscopy of the same tissue slices. The findings also showed distinct diffusivities values of lymph node sub-structures (capsule, parenchyma, and artery). This is consistent with the recent reports of distinct diffusivities in prostate and breast tissue sub-structures (2,9). The present study also found a no correlation between mean diffusivity and cellularity metrics in the three types of lymph node tissue.

The inconsistency of ADC values reported in literature also highlights the limitations of the ADC model for DWI imaging of the lymph node. Recently, a three component model, VERDICT, which characterises water diffusion in intracellular, vascular and extracellular-extravascular compartments, has shown success in distinguishing benign from malignant colorectal (127) and prostate (129) tissue. Interestingly, a recent ex vivo study on prostate tissue using VERDICT demonstrated higher information from anisotropic and restricted multi-components models than from ADC and other unrestricted biophysical models (4). This suggests that the application of more sophisticated models may improve the performance of DWI in clinical studies. Motivated by the successful implementation of biophysical models in prostate tissue, we conducted a similar investigation for lymph node tissue.

This second study, presented in Chapter 4, investigated the theoretical information from single and multi- biophysical models of diffusion in lymph node tissue to identify which model extracted the most information from the measurement data. AIC was employed to rank the models and provide objective quantitative estimation of the models' information (1). The study used high SNR data, which were obtained by imaging three lymph node tissue samples on a 9.4T MRI system. Multiple *b*-values and multiple diffusion times were utilised in image acquisition to produce a rich MR data set. Eleven models were tested with combinations of isotropic, anisotropic and restricted components. The study revealed that single component models, Ball (ADC) and DTI models, were lowest in overall AIC ranking of lymph node tissue.The multi-component models that combined anisotropic and restricted diffusion, namely, Zeppelin-sphere, Ball-stick-sphere and Ball-sphere, ranked highest in the majority of the voxels of tissue samples. The multi-component models that included anisotropic components contained more information than isotropic models. Multi-component models that accounted for diffusion restriction demonstrated higher information than unrestricted models. These findings are consistent with those from a recent ex vivo study on prostate tissue using VERDICT (4) as well as a recent study on multi- biophysical models in lymph nodes(5). It was concluded that a multi- biophysical model which includes both anisotropic and restricted components may provide more accurate and reliable DWI-based imaging of lymph node disease.

In summary, investigation of the biophysical basis of contrast in DWI of the lymph node demonstrated a distinct diffusion in lymph node sub-structure with no correlation to

cellularity. In addition, multi- biophysical models were found to extract more information from the measurement data in lymph node tissue than simple single biophysical models (ADC and DTI). These findings represent an important first step in enhancing our understanding of the biophysical basis underlying diffusion changes in the tissue.

5.2 Advances in Knowledge

The main advances in knowledge resulting from this study can be summarised as follows:

- DWI images displayed tissue contrast corresponding to distinct sub-structures in the three types of lymph node tissue tested (normal, metastatic, and lymphoma cases).

- Two distinct sub-structures (parenchyma and capsule) were found in DWI of lymph node tissue. These sub-structures, which are present in DWI images on the three types of lymph node tissue, corresponded closely to histology features seen on the light microscopy of the same tissue slices.

- Presence of multiple hyperplasia of lymphoid follicles (LF) in the normal tissue shows a prominent follicular hyperintense area in DW images, indicating highly restricted or hindered water diffusion in the follicles components.

- Higher diffusivity was found in the capsule region in comparison to parenchyma in normal and metastatic lymph node tissues.

- Parenchyma in normal lymph node tissue had the highest mean diffusivity (0.71 ± 0.17 μm^2/ms) compared to cancerous lymph node tissue, metastatic (0.52 ± 0.08 μm^2/ms) and lymphoma (0.47 ± 0.19 μm^2/ms). Higher mean diffusivity was also found in capsule sub-structure in normal tissue (1.15 ± 0.16 μm^2/ms) compared to metastatic lymph node tissue (1.07 ± 0.17 μm^2/ms).

- Kruskal-Wallis test indicated that there was a statistically significant difference in the MD of parenchyma in the three different tissue types, $\chi 2(2) = 6.129$, ($p = 0.047$) with a mean rank of MD 34.44 for metastasis, 40.96 for normal and 25.44 for lymphoma.

- *Post hoc* Mann–Whitney analysis showed differences in MD of sub-structures in all tissue types ($p > .05$).

- There was fair positive correlation between the two independent variables, MD and nuclear count with $r = 0.368$, n =69at 95 % confidence interval. As regards MD and nuclear area, no correlation with $r = 0.231$, n =69, $p > .05$ was observed. Overall, the result of Pearson's correlation showed no correlation between MD and cellularity metrics.

- Multi-component models that included anisotropic components demonstrated relatively higher information than isotropic models from multi diffusion times and multi-b values DWI measurement data in lymph node tissue ex vivo.

- Multi-component models that accounted for restricted diffusion extracted more information from multi diffusion times, multi-b values and DWI measurement data in lymph nodes ex vivo than single-component (ADC and DTI) models and multi-component unrestricted models.

In summary, a distinct diffusion contrast was found in sub-structures of normal and diseased lymph node tissue. Further, cellularity metric measurement on sub-structures of normal and diseased node tissue revealed nocorrelation between MD value and cellularity metric. Hence, it was concluded that the application of a more sophisticated model, which includes both anisotropic and restricted components, is important for describing the presence of microstructure complexity in node tissue. This is because such a model appears capable of providing greater accuracy and reliability for DWI based imaging of lymph node disease. It should be noted that caution should be exercised in generalising the findings on DWI imaging to other tissue types as differences in tissue morphology and physiology may affect water diffusivity.

5.3 Implications

The results from this ex-vivo study cannot be directly extrapolated for in-vivo imaging. However, findings from ex-vivo diffusion imaging in our study show clear evidence of distinct tissue structure features in modelling with distinct diffusivities values. This distinction is unique in lymph node tissue as well as in prostate and breast tissue. The findings from our current study could provide an evidence base for future improvements in DWI methods in distinguishing diseases particularly in clinical imaging of lymph nodes.

Findings from the present study could also be used as a reference in verifying biophysical properties underlying diffusion contrast for other types of non-neuronal tissue such as renal and liver diseases. A profile data of diffusion contrast can then be created by undergoing similar study to other types of tissue and diseases.The results of this study can also inform future improvements in DWI methods to allow optimum utilization of clinical DWI for cancer imaging. An optimization to the current DWI clinical method can be tailored with respect to the new clinical base evidence of distinct diffusion contrast specific to the types of tissue being imaged.

5.4 Limitations

This study has several limitations. Although it was based on analysis of a large number of regions of interest, the samples were small in number. For each type of node tissue, results were obtained from a small number of samples. However, results for the combined data indicated that inter-subject differences were small relative to the differences between the normal and diseased tissue being examined. Due to small number of samples used in the present study, it is recommended for future work to assess the correlation of diffusivities with cellularity and the performance of biophysical models in a large number of samples for each type of node tissue.

This study is based on ex-vivo diffusion imaging of formalin-fixed tissue obtained from post-surgical procedure. Formalin is needed to preserve the tissue.. Formalin-fixed tissue has proven to be a stable model for investigating microscopic diffusion properties of the prostate (132). In addition, significant reduction in ADC values was revealed in DWI imaging using

formalin-fixed tissue compared to in-vivo tissue (131,132). However, the results of the present study demonstrated similar diffusion properties in in-vivo imaging of normal and cancerous tissue to those seen in ex-vivo imaging. Ex-vivo imaging was also advantageous in this study due to its high spatial resolution, lower operation cost and long time image acquisition. Rich MRI data can be acquired from ex-vivo imaging, thus allowing more in-depth exploration of biophysical changes at microscopic level of the tissue.

The analysis of distinct diffusivity and multi-component modelling in this study was based on diffusion microimaging measurements of formalin-fixed normal and diseased lymph tissue at 22°C with a shorter diffusion time than is typically used in-vivo. At present, no data are available to confirm the analysis of distinct diffusivity and multicomponent modelling of fixed tissue in-vivo imaging at 37°C. Therefore, the interpretation of diffusion imaging of fixed tissue should be treated with extra caution with respect to temperature differences for in-vivo imaging.

Cellularity metric measurements for lymph node were on average twice those seen on prostate tissue (93). The morphometric analysis was carried out using a semi-automatic segmentation method, which includes a subjective assessment. Hence, a huge amount of time was needed to identify and count the number of nuclei from the background images. While a comparison with manual segmentation suggested the resultant bias was minor, it would be desirable to utilise an automated segmentation technique in the future to minimise reliance on subjective assessment.

Overall, the analysis in this study is crucially dependent on the alignment between MR images and corresponding histology sections. Better alignment is important to ensure that the diffusion behaviour precisely corresponds to the microstructures of the tissue sample. This can be achieved by proposing the depth for the histology sectioning before cutting the tissue cores. The depth given prior to sectioning will provide a marker to aid alignment of the MR images at a similar plane to the tissue sections. It is noteworthy that some of the tissues were not sectioned perpendicular to the image planes. This created a significant challenge in alignment between the histology section and the MR images.

Alignment between MR images and the corresponding histology tissue slices is challenging when the tissue is not cut perpendicular to the tissue plane. Although we had proposed pre-

cutting tissue slices with equivalent depth as guidance to the operator, there was some uncertainty in the alignment between the ROIs used for measurement of diffusivity and the corresponding ROIs defined in the histological sections in Chapter 3. This problem is not unique to this particular method, and such uncertainties would have been greater in previous studies carried out to compare ADC measured in-vivo with cellularity metrics (100,108,134). The alignment method in the present study was done qualitatively, it would be desirable to use a spatial transformation in Matlab code using 3D rotation and linear interpolation in order to obtain an oblique MR slice to match the histology tissue slice for future work.

This study employed the simple and clinically ubiquitous mono-exponential diffusion model that assumes Gaussian dynamics. However, it should be noted that the diffusion in tissue is not free and signal attenuation is not well-modelled as a mono-exponential (72,144,145). Non-Gaussian models, such as the biexponential and kurtosis models, fit the signal decay better but the parameters derived from these models do not relate to specific tissue structures or compartments (146). Instead of ADC values, mean diffusivity values were used in this study because this has the advantage of averaging the diffusivity measurement over six gradient directions.

The 11 models that were employed for multi-component models analysis in this study assumed that there was no water exchange between compartments. Investigation on cultured cells, however, has demonstrated that cell membrane permeability affects the model parameters at varying diffusion times (117,147). Consequently, future work may need to develop multi-component models that account for water exchange between compartments.

5.5 Future Work

As highlighted in the previous section, analysis in this study was based on a small number of samples for each type of node tissue. It is recommended that large numbers of samples for each type of node tissue be used in future work to assess the correlation of diffusivities with cellularity and the performance of biophysical models.

It is also important to extend this study by comparing diffusivities in lymph node tissue with clinical in-vivo results. It should be noted that the analysis of distinct diffusivity and multicomponent modelling in this study was based on ex vivo diffusion microimaging measurements of formalin-fixed normal and diseased lymph node tissue at 22°C. At present, no data are available to confirm the analysis of distinct diffusivity in similar MR magnitude *in-vivo* at 37°C. It would be of interest to investigate the difference that may arise from ex vivo imaging at room temperature in fixed tissue.

Before proceeding with cellularity measurement, segmentation requires subjective assessment. Subjective assessment is dependent on good image viewing conditions. Use of a monitor screen with wide panel and high resolution is therefore recommended. Viewing conditions should facilitate the selection of small nuclei size and background in the histology tissue section, which is crucial in measurement of cellularity metrics.

Maintaining a better alignment between MR images and the corresponding histology tissue slices is challenging, especially when the tissue is not cut perpendicular to the tissue plane. For future work, it would be desirable to use a spatial transformation in Matlab code using 3D rotation and linear interpolation to obtain oblique MR slices to match with the histology tissue slices.

The eleven models employed for the multi-component model analysis assumed no water exchange between compartments where fixed tissues samples were used in the present study. Multicomponent models that account for water exchange between compartments need to be developed in future work. It is recommended for future work to plot a graph to determine the relationship between of diffusion signal and *b*-value showing the measurements and the model fit for the worst (ADC) and best model (Zeppelin-Sphere). It is also recommended for future work to examine the cause of variation of the model parameters in the best model

between cancerous and non-cancerous tissue. . It is also recommended for future work to include the actual DWI images to allow assessment of the data quality.The development of reliable and accurate DWI depends on solid understanding of the biophysical basis underlying diffusion contrast in tissue. It is equally important for providing reliable information – for example, on cancer localisation and volume estimation - that is crucial in cancer patient management. Better cancer imaging will eventually lead to effective cancer detection and, ultimately, more effective treatment with less harmful side effects to patients.

Bibliography

1. Burnham KP, Anderson DR. Model selection and multimodel inference: A practical information-theoretic approach. New York: Springer; 2002.

2. Norddin N, Power C, Watson G, Cowin G, Kurniawan ND, Gluch L, Bourne RM. Microscopic diffusion properties of fixed breast tissue: Preliminary findings. Magnetic Resonance in Medicine 2015;74(6):1733-1739.

3. Bourne RM, Kurniawan N, Cowin G, Stait-Gardner T, Sved P, Watson G, Price WS. Microscopic diffusivity compartmentation in formalin-fixed prostate tissue. Magnetic Resonance in Medicine 2012;68(2):614-620.

4. Liang S, Panagiotaki E, Bongers A, Shi P, Sved P, Watson G, Bourne R. Information-based ranking of 10 compartment models of diffusion-weighted signal attenuation in fixed prostate tissue. NMR in Biomedicine 2016;29(5):660-671.

5. Ianus A, Santiago I, Alexander DC, Shemesh CMN. Comparison of diffusion MR models in lymph nodes at ultra high field. SMRT 27th Joint Annual Meeting ISMRM-ESMRMB 2018, Paris, France, June 2018, Proceeding. Volume 5373 *Abstract*. Paris: International Society for Magnetic Resonance in Medicine (ISMRM); 2018.

6. Schaefer PW, Grant PE, Gonzalez RG. Diffusion-weighted MR Imaging of the Brain. Radiology 2000;217(2):331-345.

7. Calvar JA, Meli FJ, Romero C, Yánez MLCP, Martinez AR, Lambre H, Taratuto AL, Sevlever G. Characterization of brain tumors by MRS, DWI and Ki-67 labeling index. Journal of Neuro-Oncology 2005;72(3):273-280.

8. Bourne R, Kurniawan N, Cowin G, Sved P, Watson G. 16 T diffusion microimaging of fixed prostate tissue: preliminary findings. Magnetic Resonance in Medicine 2011;66(1):244-247.

9. Bourne RM, Kurniawan N, Cowin G, Sved P, Watson G. Microscopic diffusion anisotropy in formalin fixed prostate tissue: preliminary findings. Magnetic Resonance in Medicine 2012;68(6):1943-1948.

10. Woodhams R, Kakita S, Hata H, Iwabuchi K, Umeoka S, Mountford CE, Hatabu H. Diffusion-weighted imaging of mucinous carcinoma of the breast: evaluation of apparent diffusion coefficient and signal intensity in correlation with histologic findings. American Journal of Roentgenology 2009;193(1):260-266.

11. Koinuma M, Ohashi I, Hanafusa K, Shibuya H. Apparent diffusion coefficient measurements with diffusion-weighted magnetic resonance imaging for evaluation of hepatic fibrosis. Journal of Magnetic Resonance Imaging 2005;22(1):80-85.

12. Mannelli L, Kim S, Hajdu CH, Babb JS, Clark TWI, Taouli B. Assessment of Tumor Necrosis of Hepatocellular Carcinoma After Chemoembolization: Diffusion-Weighted and Contrast-Enhanced MRI With Histopathologic Correlation of the Explanted Liver. American Journal of Roentgenology 2009;193(4):1044-1052.

13. Manenti G, Di Roma M, Mancino S, Bartolucci DA, Palmieri G, Mastrangeli R, Miano R, Squillaci E, Simonetti G. Malignant renal neoplasms: correlation between ADC values and cellularity in diffusion weighted magnetic resonance imaging at 3 T. La Radiologia medica 2008;113(2):199-213.

14. Squillaci E, Manenti G, Cova M, Di Roma M, Miano R, Palmieri G, Simonetti G. Correlation of diffusion-weighted MR imaging with cellularity of renal tumours. Anticancer research 2004;24(6):4175-4179.

15. Sumi M, Nakamura T, Sakihama N, Sumi T, Morikawa M, Uetani M, Kabasawa H, Shigeno K, Hayashi K, Takahashi H. Discrimination of metastatic cervical lymph nodes with diffusion-weighted MR imaging in patients with head and neck cancer. American Journal of Neuroradiology 2003;24(8):1627-1634.

16.   Kamitani T, Hatakenaka M, Yabuuchi H, Matsuo Y, Fujita N, Jinnouchi M, Nagao M, Shirahane K, Tokunaga E, Honda H. Detection of axillary node metastasis using diffusion-weighted MRI in breast cancer. Clinical Imaging 2013;37(1):56-61.

17.   Leong SPL, Cady B, Jablons DM, Garcia-Aguilar J, Reintgen D, Jakub J, Pendas S, Duhaime L, Cassell R, Gardner M, Giuliano R, Archie V, Calvin D, Mensha L, Shivers S, Cox C, Werner JA, Kitagawa Y, Kitajima M. Clinical patterns of metastasis. Cancer and Metastasis Reviews 2006;25(2):221-232.

18.   Noone AM, Howlader N, Krapcho M, Miller D, Brest A, Yu M, Ruhl J, Tatalovich Z, Mariotto A, Lewis DR, Chen HS, Feuer EJ, (eds) CK. SEER Cancer Statistics Review, 1975-2015. November 2017 ed. National Cancer Institute. Bethesda, MD.2015.

19.   Torre LA, Bray F, Siegel RL, Ferlay J, Lortet-Tieulent J, Jemal A. Global cancer statistics, 2012. CA: A Cancer Journal for Clinicians 2015;65(2):87-108.

20.   Parkin DM, Boyd L, Walker LC. The fraction of cancer attributable to lifestyle and environmental factors in the UK in 2010: Summary and conclusions. British Journal of Cancer 2011;105(Suppl 2):77-81.

21.   AIHW. Australian Institute of Health and Welfare & Australasian Association of Cancer Registries 2012. Cancer in Australia: an overview 2012. Cancer series no. 74. Cat no CAN 70 Canberra: AIHW p.

22.   Pharoah PDP, Dunning AM, Ponder BAJ, Easton DF. Association studies for finding cancer-susceptibility genetic variants. Nature Reviews Cancer 2004;4:850.

23.   Wong SY, Hynes RO. Lymphatic or Hematogenous Dissemination: How Does a Metastatic Tumor Cell Decide? Cell Cycle 2006;5(8):812-817.

24.   Gupta GP, Massagué J. Cancer Metastasis: Building a Framework. Cell 2006;127(4):679-695.

25.   Fidler IJ, Kripke ML. The challenge of targeting metastasis. Cancer Metastasis Reviews 2015;34(4):635-641.

26.   Carr I. Lymphatic metastasis. Cancer metastasis reviews 1983;2(3):307-317.

27.   Sanpaolo P, Barbieri V, Genovesi D. Prognostic value of breast cancer subtypes on breast cancer specific survival, distant metastases and local relapse rates in conservatively managed early stage breast cancer: A retrospective clinical study. European Journal of Surgical Oncology 2011;37(10):876-882.

28.   Tsui K-H, Shvarts O, Smith RB, Figlin RA, deKernion JB, Belldegrun A. Prognostic Indicators for Renal Cell Carcinoma: A Multivariate Analysis of 643 Patients using Revised 1997 TNM Staging Criteria. Journal of Urology 2000;163(4):1090-1095.

29.   Greene FL, Stewart AK, Norton HJ. A new TNM staging strategy for node-positive (Stage III) colon cancer - An analysis of 50,042 patients. Annals of Surgery 2002;236(4):416-421.

30.   Krstić RV. Human microscopic anatomy: an atlas for students of medicine and biology. New York, Berlin: Springer-Verlag; 1991.

31.   Olteanu H, Harrington A. Lymph nodes. New York: Demos Medical Publishing; 2012.

32.   Ioachim HL, Medeiros LJ. Ioachim's lymph node pathology. Philadelphia: Wolters Kluwer Health/Lippincott Williams & Wilkins; 2009.

33.   Willard-Mack CL. Normal Structure, Function, and Histology of Lymph Nodes. Toxicologic Pathology 2006;34(5):409-424.

34.   Dabbs DJ. Breast Pathology: Elsevier Health Sciences; 2012.

35.   Miranda RN, Khoury JD, Medeiros LJ. Atlas of lymph node pathology. New York: Springer; 2013.

36.   Ecanow JS, Abe H, Newstead GM, Ecanow DB, Jeske JM. Axillary staging of breast cancer: what the radiologist should know. Radiographics 2013;33(6):1589-1612.

37.   Sumi M, Van Cauteren M, Nakamura T. MR microimaging of benign and malignant nodes in the neck. American Journal of Roentgenology 2006;186(3):749-757.

38.   Compton CC, Byrd DR, Garcia-Aguilar J. AJCC Cancer Staging Atlas: A Companion to the Seventh Editions of the AJCC Cancer Staging Manual and Handbook. Dordrecht: Springer; 2012.

39.   Roy C, Bierry G, Matau A, Bazille G, Pasquali R. Value of diffusion-weighted imaging to detect small malignant pelvic lymph nodes at 3 T. European Radiology 2010;20(8):1803-1811.

40.   Klerkx WM, Geldof AA, Heintz AP, van Diest PJ, Visser F, Mali WP, Veldhuis WB. Longitudinal 3.0T MRI analysis of changes in lymph node volume and apparent diffusion coefficient in an experimental animal model of metastatic and hyperplastic lymph nodes. Journal of Magnetic Resonance Imaging 2011;33(5):1151-1159.

41.   Chung J, Youk JH, Kim J-A, Gweon HM, Kim E-K, Ryu YH, Son EJ. Role of diffusion-weighted MRI: predicting axillary lymph node metastases in breast cancer. Acta Radiologica 2013;55(8):909-916.

42.   Torabi M, Aquino SL, Harisinghani MG. Current Concepts in Lymph Node Imaging. The Journal of Nuclear Medicine 2004;45(9):1509-1518.

43.   Mariani G, Moresco L, Viale G, Villa G, Bagnasco M, Canavese G, Buscombe J, Strauss HW, Paganelli G. Radioguided sentinel lymph node biopsy in breast cancer surgery. The Journal of Nuclear Medicine 2001;42(8):1198.

44.   Veronesi UMD, Paganelli GMD, Viale GF, Luini AMD, Zurrida SMD, Galimberti VMD, Intra MMD, Veronesi PMD, Robertson CP, Maisonneuve PE, Renne GMD, De Cicco CMD, De Lucia FMD, Gennari RMD. A randomized comparison of sentinel-node

biopsy with routine axillary dissection in breast cancer. The New England Journal of Medicine 2003;349(6):546-553.

45.   Moghimi M, Ghoddosi I, Rahimabadi AE, Sheikhvatan M. Accuracy of sentinel node biopsy in breast cancer patients with a high prevalence of axillary metastases. Scandinavian Journal of Surgery 2009;98(1):30-33.

46.   Shiller SM, Weir R, Pippen J, Punar M, Savino D. The sensitivity and specificity of sentinel lymph node biopsy for breast cancer at Baylor University Medical Center at Dallas: a retrospective review of 488 cases. Proceedings of Baylor University Medical Center 2011;24(2):81-85.

47.   Cheng J, Wang Y, Deng J, McCarthy RJ, Wang G, Wang H, Ye Y. Discrimination of metastatic lymph nodes in patients with gastric carcinoma using diffusion-weighted imaging. Journal of Magnetic Resonance Imaging 2013;37(6):1436-1444.

48.   Nakai G, Matsuki M, Inada Y, Tatsugami F, Tanikake M, Narabayashi I, Yamada T. Detection and evaluation of pelvic lymph nodes in patients with gynecologic malignancies using body diffusion-weighted magnetic resonance imaging. Journal of computer assisted tomography 2008;32(5):764-768.

49.   Heijnen LA, Lambregts DMJ, Mondal D, Martens MH, Riedl RG, Beets GL, Beets-Tan RGH. Diffusion-weighted MR imaging in primary rectal cancer staging demonstrates but does not characterise lymph nodes. European Radiology 2013;23(12):3354-3360.

50.   Estelrich J, Sánchez-Martín MJ, Busquets MA. Nanoparticles in magnetic resonance imaging: from simple to dual contrast agents. International Journal of Nanomedicine 2015;10:1727.

51.   He N, Xie C, Wei W, Pan C, Wang W, Lv N, Wu P. A new, preoperative, MRI-based scoring system for diagnosing malignant axillary lymph nodes in women evaluated for breast cancer. European Journal of Radiology 2012;81(10):2602-2612.

52.   Rosen MA, Schnall MD. Dynamic contrast-enhanced magnetic resonance imaging for assessing tumor vascularity and vascular effects of targeted therapies in renal cell carcinoma. Clinical cancer research : an official journal of the American Association for Cancer Research 2007;13(2 Pt 2):770s-776s.

53.   Korteweg MA, Veldhuis WB, Zwanenburg JJM, Hoogduin JM, van den Bosch MAAJ, van Diest PJ, van Hillegersberg R, Eijkemans MJC, Mali WPTM, Luijten PR. Dissected sentinel lymph nodes of breast cancer patients: characterization with high-spatial-resolution 7-T MR imaging. Radiology 2011;261(1):127-135.

54.   Kvistad KA, Rydland J, Smethurst HB, Lundgren S, Fjøsne HE, Haraldseth O. Axillary lymph node metastases in breast cancer: preoperative detection with dynamic contrast-enhanced MRI. European Radiology 2000;10(9):1464-1471.

55.   Asaumi J-i, Yanagi Y, Hisatomi M, Matsuzaki H, Konouchi H, Kishi K. The value of dynamic contrast-enhanced MRI in diagnosis of malignant lymphoma of the head and neck. European Journal of Radiology 2003;48(2):183-187.

56.   Alberda WJ, Dassen HP, Dwarkasing RS, Willemssen FE, Pool AEvd, Wilt JHWd, Burger JW, Verhoef C. Prediction of tumor stage and lymph node involvement with dynamic contrast-enhanced MRI after chemoradiotherapy for locally advanced rectal cancer. International Journal of Colorectal Disease 2013;28(4):573-580.

57.   Weissleder R, Elizondo G, Wittenberg J, Rabito CA, Bengele HH, Josephson L. Ultrasmall superparamagnetic iron oxide: characterization of a new class of contrast agents for MR imaging. Radiology 1990;175(2):489-493.

58.   Thoeny HC, Triantafyllou M, Birkhaeuser FD, Froehlich JM, Tshering DW, Binser T, Fleischmann A, Vermathen P, Studer UE. Combined ultrasmall superparamagnetic particles of iron oxide-enhanced and diffusion-weighted magnetic resonance imaging reliably detect pelvic lymph node metastases in normal-sized nodes of bladder and prostate cancer patients. European Urology 2009;55(4):761-769.

59.   Birkhauser FD, Studer UE, Froehlich JM, Triantafyllou M, Bains LJ, Petralia G, Vermathen P, Fleischmann A, Thoeny HC. Combined ultrasmall superparamagnetic particles of iron oxide-enhanced and diffusion-weighted magnetic resonance imaging facilitates detection of metastases in normal-sized pelvic lymph nodes of patients with bladder and prostate cancer. European Urology 2013;64(6):953-960.

60.   Memarsadeghi M, Riedl CC, Kaneider A, Galid A, Rudas M, Matzek W, Helbich TH. Axillary lymph node metastases in patients with breast carcinomas: assessment with nonenhanced versus uspio-enhanced MR imaging. Radiology 2006;241(2):367-377.

61.   Kinner S, Maderwald S, Albert J, Parohl N, Corot C, Robert P, Baba HA, Barkhausen J. Discrimination of benign and malignant lymph nodes at 7.0T compared to 1.5T magnetic resonance imaging using ultrasmall particles of iron oxide: a feasibility preclinical study. Academic radiology 2013;20(12):1604-1609.

62.   Kataoka Y, Murata Y, Miyatake K, Tadokoro M, Nakatani K, Kubota K, Hamada N, Nishioka A, Ogawa Y. Diffusion-weighted Imaging for Parasternal Lymph Nodes in Breast Cancer: Report of Two Cases. Magnetic Resonance in Medical Sciences 2011;10(1):53-57.

63.   Xu L, Tian J, Liu Y, Li C. Accuracy of diffusion-weighted (DW) MRI with background signal suppression (MR-DWIBS) in diagnosis of mediastinal lymph node metastasis of nonsmall-cell lung cancer (NSCLC). Journal of Magnetic Resonance Imaging 2014;40(1):200-205.

64.   Takahara T, Imai Y, Yamashita T, Yasuda S, Nasu S, Van Cauteren M. Diffusion weighted whole body imaging with background body signal suppression (DWIBS): technical improvement using free breathing, STIR and high resolution 3D display. Radiation medicine 2004;22(4):275-282.

65.   Kwee TC, Takahara T, Ochiai R, Nievelstein RAJ, Luijten PR. Diffusion-weighted whole-body imaging with background body signal suppression (DWIBS): features and potential applications in oncology. European Radiology 2008;18(9):1937-1952.

66.   Donati OF, Jung SI, Vargas HA, Gultekin DH, Zheng J, Moskowitz CS, Hricak H, Zelefsky MJ, Akin O. Multiparametric Prostate MR Imaging with T2-weighted, Diffusion-weighted, and Dynamic Contrast-enhanced Sequences: Are All Pulse Sequences Necessary to Detect Locally Recurrent Prostate Cancer after Radiation Therapy? Radiology 2013;268(2):440-450.

67.   Isebaert S, Van Poppel H, Oyen R, Van den Bergh L, Haustermans K, Joniau S, Lerut E, De Wever L, De Keyzer F, Budiharto T, Slagmolen P. Multiparametric MRI for prostate cancer localization in correlation to whole-mount histopathology. Journal of Magnetic Resonance Imaging 2013;37(6):1392-1401.

68.   Arlinghaus LR, Yankeelov TE. Diffusion-Weighted MRI. In: Yankeelov TE, Pickens DR, Price RR, editors. Quantitative MRI in cancer: Taylor & Francis; 2012. p 81-97.

69.   Dietrich O, Biffar A, Baur-Melnyk A, Reiser MF. Technical aspects of MR diffusion imaging of the body. European Journal of Radiology 2010;76(3):314-322.

70.   Chenevert TL. Principles of Diffusion-Weighted Imaging (DW-MRI) as Applied to Body Imaging. In: Koh DM, H.C. T, editors. Diffusion-Weighted MR Imaging. London: Springer; 2010. p 1-17.

71.   White NS, McDonald CR, Farid N, Kuperman J, Karow D, Schenker-Ahmed NM, Bartsch H, Rakow-Penner R, Holland D, Shabaik A, Bjørnerud A, Hope T, Hattangadi-Gluth J, Liss M, Parsons JK, Chen CC, Raman S, Margolis D, Reiter RE, Marks L, Kesari S, Mundt AJ, Kane CJ, Carter BS, Bradley WG, Dale AM. Diffusion-Weighted Imaging in Cancer: Physical Foundations and Applications of Restriction Spectrum Imaging. Cancer research 2014;74(17):4638-4652.

72.   Le Bihan D. Apparent diffusion coefficient and beyond: what diffusion MR imaging can tell us about tissue structure. Radiology 2013;268(2):318-322.

73.   Padhani AR, Collins D, Hammoud DA, Rustin GJS, Taouli B, Choyke PL, Liu G, Koh DM, Chenevert TL, Thoeny HC, Takahara T, Dzik-Jurasz A, Ross BD, Van Cauteren M.

Diffusion-weighted magnetic resonance imaging as a cancer biomarker: consensus and recommendations. Neoplasia 2009;11(2):102-125.

74.   Maier SE, Mulkern RV. Biexponential analysis of diffusion-related signal decay in normal human cortical and deep gray matter. Magnetic Resonance Imaging 2008;26(7):897-904.

75.   Anderson AW, Xie J, Pizzonia J, Bronen RA, Spencer DD, Gore JC. Effects of cell volume fraction changes on apparent diffusion in human cells. Magn Reson Imaging 2000;18(6):689-695.

76.   Latour LL, Svoboda K, Mitra PP, Sotak CH. Time-dependent diffusion of water in a biological model system. Proceedings of the National Academy of Sciences 1994;91(4):1229-1233.

77.   van der Toorn A, Syková E, Dijkhuizen RM, Vořišek I, Vargová L, Škobisová E, van Lookeren Campagne M, Reese T, Nicolay K. Dynamic changes in water ADC, energy metabolism, extracellular space volume, and tortuosity in neonatal rat brain during global ischemia. Magnetic Resonance in Medicine 1996;36(1):52-60.

78.   Basser PJ, Jones DK. Diffusion-tensor MRI: theory, experimental design and data analysis - a technical review. NMR in Biomedicine 2002;15(7-8):456-467.

79.   Stejskal EO, Tanner JE. Spin diffusion measurements: spin echoes in the presence of a time-dependent field gradient. Journal of Chemical Physics 1965;42(1):288.

80.   Mukherjee P, Berman JI, Chung SW, Hess CP, Henry RG. Diffusion Tensor MR Imaging and Fiber Tractography: Theoretic Underpinnings. American Journal of Neuroradiology 2008;29(4):632-641.

81.   Hagmann P, Jonasson L, Maeder P, Thiran J-P, Wedeen VJ, Meuli R. Understanding diffusion MR imaging techniques: from scalar diffusion-weighted imaging to diffusion tensor imaging and beyond. Radiographics 2006;26 Suppl 1:S205-U219.

82.	Fornasa F, Nesoti MV, Bovo C, Bonavina MG. Diffusion-weighted magnetic resonance imaging in the characterization of axillary lymph nodes in patients with breast cancer. Journal of Magnetic Resonance Imaging 2012;36(4):858-864.

83.	Scaranelo AM, Eiada R, Jacks LM, Kulkarni SR, Crystal P. Accuracy of unenhanced MR imaging in the detection of axillary lymph node metastasis: study of reproducibility and reliability. Radiology 2012;262(2):425-434.

84.	Luo N, Su D, Jin G, Liu L, Zhu X, Xie D, Liu Y. Apparent diffusion coefficient ratio between axillary lymph node with primary tumor to detect nodal metastasis in breast cancer patients. Journal of Magnetic Resonance Imaging 2013;38(4):824-828.

85.	Rechichi G, Galimberti S, Oriani M, Perego P, Valsecchi MG, Sironi S. ADC maps in the prediction of pelvic lymph nodal metastatic regions in endometrial cancer. European Radiology 2013;23(1):65-74.

86.	Abdel Razek AAK, Soliman NY, Elkhamary S, Alsharaway MK, Tawfik A. Role of diffusion-weighted MR imaging in cervical lymphadenopathy. European radiology 2006;16(7):1468-1477.

87.	Luciani A, Pigneur F, Ghozali F, Dao T-H, Cunin P, Meyblum E, De Baecque-Fontaine C, Alamdari A, Maison P, Deux JF, Lagrange JL, Lantieri L, Rahmouni A. Ex vivo MRI of axillary lymph nodes in breast cancer. European Journal of Radiology 2009;69(1):59-66.

88.	Lambregts DMJ, Beets GL, Maas M, Curvo-Semedo L, Kessels AGH, Thywissen T, Beets-Tan RGH. Tumour ADC measurements in rectal cancer: effect of ROI methods on ADC values and interobserver variability. European Radiology 2011;21(12):2567-2574.

89.	Thoeny HC, Froehlich JM, Triantafyllou M, Huesler J, Bains LJ, Vermathen P, Fleischmann A, Studer UE. Metastases in normal-sized pelvic lymph nodes: detection with diffusion-weighted MR imaging. Radiology 2014;273(1):125.

90.   Korteweg MA, Zwanenburg JJM, van Diest PJ, van den Bosch MAAJ, Luijten PR, van Hillegersberg R, Mali WPTM, Veldhuis WB. Characterization of ex vivo healthy human axillary lymph nodes with high resolution 7 Tesla MRI. European radiology 2011;21(2):310-317.

91.   Holzapfel K, Duetsch S, Fauser C, Eiber M, Rummeny EJ, Gaa J. Value of diffusion-weighted MR imaging in the differentiation between benign and malignant cervical lymph nodes. European Journal of Radiology 2009;72(3):381-387.

92.   Yamaguchi K, Schacht D, Nakazono T, Irie H, Abe H. Diffusion weighted images of metastatic as compared with nonmetastatic axillary lymph nodes in patients with newly diagnosed breast cancer. Journal of Magnetic Resonance Imaging 2014;42(3):771-778.

93.   Chatterjee A, Watson G, Myint E, Sved P, McEntee M, Bourne R. Changes in Epithelium, Stroma, and Lumen Space Correlate More Strongly with Gleason Pattern and Are Stronger Predictors of Prostate ADC Changes than Cellularity Metrics. Radiology 2015;277(3):751-762.

94.   Sugahara T, Korogi Y, Kochi M, Ikushima I, Shigematu Y, Hirai T, Okuda T, Liang L, Ge Y, Komohara Y, Ushio Y, Takahashi M. Usefulness of diffusion-weighted MRI with echo-planar technique in the evaluation of cellularity in gliomas. Journal of Magnetic Resonance Imaging 1999;9(1):53-60.

95.   Gupta RK, Cloughesy TF, Sinha U, Garakian J, Lazareff J, Rubino G, Rubino L, Becker DP, Vinters HV, Alger JR. Relationships between choline magnetic resonance spectroscopy, apparent diffusion coefficient and quantitative histopathology in human glioma. Journal of neuro-oncology 2000;50(3):215-226.

96.   Gauvain KM, McKinstry RC, Mukherjee P, Perry A, Neil JJ, Kaufman BA, Hayashi RJ. Evaluating pediatric brain tumor cellularity with diffusion-tensor imaging. American Journal of Roentgenology 2001;177(2):449-454.

97. Guo Y, Cai Y-Q, Cai Z-L, Gao Y-G, An N-Y, Ma L, Mahankali S, Gao J-H. Differentiation of clinically benign and malignant breast lesions using diffusion-weighted imaging. Journal of Magnetic Resonance Imaging 2002;16(2):172-178.

98. Yoshikawa MI, Ohsumi S, Sugata S, Kataoka M, Takashima S, Mochizuki T, Ikura H, Imai Y. Relation between cancer cellularity and apparent diffusion coefficient values using diffusion-weighted magnetic resonance imaging in breast cancer. Radiation medicine 2008;26(4):222-226.

99. Hatakenaka M, Soeda H, Yabuuchi H, Matsuo Y, Kamitani T, Oda Y, Tsuneyoshi M, Honda H. Apparent diffusion coefficients of breast tumors: clinical application. Magnetic Resonance in Medical Sciences 2008;7(1):23-29.

100. Zelhof B, Pickles M, Liney G, Gibbs P, Rodrigues G, Kraus S, Turnbull L. Correlation of diffusion-weighted magnetic resonance data with cellularity in prostate cancer. British Journal of Urology International 2009;103(7):883-883.

101. Gibbs P, Liney GP, Pickles MD, Zelhof B, Rodrigues G, Turnbull LW. Correlation of ADC and T2 Measurements With Cell Density in Prostate Cancer at 3.0 Tesla. Investigative radiology 2009;44(9):572-576.

102. Wang XZ, Wang B, Gao ZQ, Liu JG, Liu ZQ, Niu QL, Sun ZK, Yuan YX. Diffusion-weighted imaging of prostate cancer: Correlation between apparent diffusion coefficient values and tumor proliferation. Journal of Magnetic Resonance Imaging 2009;29(6):1360-1366.

103. Wu X, Pertovaara H, Dastidar P, Vornanen M, Paavolainen L, Marjomäki V, Järvenpää R, Eskola H, Kellokumpu-Lehtinen P-L. ADC measurements in diffuse large B-cell lymphoma and follicular lymphoma: a DWI and cellularity study. European Journal of Radiology 2013;82(4):e158-E164.

104. Surov A, Caysa H, Wienke A, Spielmann RP, Fiedler E. Correlation between different ADC fractions,cell count, Ki-67, total nucleic areas and average nucleic areas in meningothelial meningiomas. Anticancer research 2015;35(12):6841-6846.

105. Onishi N, Kanao S, Kataoka M, Iima M, Sakaguchi R, Kawai M, Kataoka TR, Mikami Y, Toi M, Togashi K. Apparent diffusion coefficient as a potential surrogate marker for Ki-67 index in mucinous breast carcinoma. Journal of Magnetic Resonance Imaging 2015;41(3):610-615.

106. Borren A, Groenendaal G, Moman MR, Boeken Kruger AE, van Diest PJ, van Vulpen M, Philippens MEP, van der Heide UA. Accurate prostate tumour detection with multiparametric magnetic resonance imaging: dependence on histological properties. Acta Oncologica 2014;53(1):88-95.

107. Rosenkrantz AB, Mendrinos S, Babb JS, Taneja SS. Prostate cancer foci detected on multiparametric magnetic resonance imaging are histologically distinct from those not detected. The Journal of Urology 2012;187(6):2032-2038.

108. Langer DL, Van Der Kwast TH, Evans AJ, Plotkin A, Trachtenberg J, Wilson BC, Haider MA. Prostate tissue composition and MR measurements: Investigating the relationships between ADC, T2, Ktrans, Ve, and corresponding histologic features. Radiology 2010;255(2):485-494.

109. Taouli B, Tolia AJ, Losada M, Babb JS, Chan ES, Bannan MA, Tobias H. Diffusion-Weighted MRI for Quantification of Liver Fibrosis: Preliminary Experience. American Journal of Roentgenology 2007;189(4):799-806.

110. Venkataraman G, Rycyna K, Rabanser A, Heinze G, Baesens BM, Ananthanarayanan V, Paner GP, Barkan GA, Flanigan RC, Wojcik EM. Morphometric signature differences in nuclei of Gleason pattern 4 areas in Gleason 7 prostate cancer with differing primary grades on needle biopsy. J Urol 2009;181(1):88-93; discussion 93-84.

111. Irshad H, Veillard A, Roux L, Racoceanu D. Methods for Nuclei Detection, Segmentation, and Classification in Digital Histopathology: A Review—Current Status and Future Potential. IEEE Reviews in Biomedical Engineering 2014;7:97-114.

112. Mulkern RV, Barnes AS, Haker SJ, Hung YP, Rybicki FJ, Maier SE, Tempany CMC. Biexponential characterization of prostate tissue water diffusion decay curves over an extended b-factor range. Magnetic Resonance Imaging 2006;24(5):563-568.

113. Shinmoto H, Oshio K, Tanimoto A, Higuchi N, Okuda S, Kuribayashi S, Mulkern RV. Biexponential apparent diffusion coefficients in prostate cancer. Magnetic Resonance Imaging 2009;27(3):355-359.

114. Bennett KM, Schmainda KM, Bennett RT, Rowe DB, Lu H, Hyde JS. Characterization of continuously distributed cortical water diffusion rates with a stretched-exponential model. Magnetic Resonance in Medicine 2003;50(4):727-734.

115. Jensen JH, Helpern JA. MRI quantification of non-Gaussian water diffusion by kurtosis analysis. NMR in biomedicine 2010;23(7):698-710.

116. Le Bihan D, van Zijl P. From the diffusion coefficient to the diffusion tensor. NMR Biomed 2002;15(7-8):431-434.

117. Thelwall PE, Grant SC, Stanisz GJ, Blackband SJ. Human erythrocyte ghosts: exploring the origins of multiexponential water diffusion in a model biological tissue with magnetic resonance. Magnetic Resonance in Medicine 2002;48(4):649-657.

118. Grant SC, Buckley DL, Gibbs S, Webb AG, Blackband SJ. MR microscopy of multicomponent diffusion in single neurons. Magnetic Resonance in Medicine 2001;46(6):1107-1112.

119. Forder JR, Bui JD, Buckley DL, Blackband SJ. MR imaging measurement of compartmental water diffusion in perfused heart slices. American Journal of Physiology - Heart and Circulatory Physiology 2001;281(3):H1280.

120. Jensen JH, Helpern JA, Ramani A, Lu H, Kaczynski K. Diffusional kurtosis imaging: the quantification of non-gaussian water diffusion by means of magnetic resonance imaging. Magnetic Resonance in Medicine 2005;53(6):1432-1440.

121. Liu X, Zhou L, Peng W, Wang H, Zhang Y. Comparison of stretched-Exponential and monoexponential model diffusion-Weighted imaging in prostate cancer and normal tissues. Journal of Magnetic Resonance Imaging 2015;42(4):1078-1085.

122. Tamura C, Shinmoto H, Soga S, Okamura T, Sato H, Okuaki T, Pang Y, Kosuda S, Kaji T. Diffusion kurtosis imaging study of prostate cancer: Preliminary findings. Journal of Magnetic Resonance Imaging 2014;40(3):723-729.

123. Bihan DL, Breton E, Lallemand D, Aubin ML, Vignaud J, Laval-Jeantet M. Separation of diffusion and perfusion in intravoxel incoherent motion MR imaging. Radiology 1988;168(2):497-505.

124. Yu X-p, Wen L, Hou J, Bi F, Hu P, Wang H, Wang W. Discrimination between Metastatic and Nonmetastatic Mesorectal Lymph Nodes in Rectal Cancer Using Intravoxel Incoherent Motion Diffusion-weighted Magnetic Resonance Imaging. Academic Radiology 2016;23(4):479-485.

125. Qiu L, Liu XL, Liu SR, Weng ZP, Chen XQ, Feng YZ, Cai XR, Guo CY. Role of quantitative intravoxel incoherent motion parameters in the preoperative diagnosis of nodal metastasis in patients with rectal carcinoma. Journal of Magnetic Resonance Imaging 2016;44(4):1031-1039.

126. Hauser T, Essig M, Jensen A, Laun FB, Munter M, Maier-Hein KH, Stieltjes B. Prediction of treatment response in head and neck carcinomas using IVIM-DWI: Evaluation of lymph node metastasis. European Journal of Radiology 2014;83(5):783-787.

127. Panagiotaki E, Walker-Samuel S, Siow B, Johnson SP, Rajkumar V, Pedley RB, Lythgoe MF, Alexander DC. Noninvasive quantification of solid tumor microstructure using VERDICT MRI. Cancer research 2014;74(7):1902-1912.

128. Reynaud O. Time-Dependent Diffusion MRI in Cancer: Tissue Modeling and Applications. Frontiers in Physics 2017;5(58).

129. Panagiotaki E, Chan RW, Dikaios N, Ahmed HU, O'Callaghan J, Freeman A, Atkinson D, Punwani S, Hawkes DJ, Alexander DC. Microstructural characterization of normal and malignant human prostate tissue with vascular, extracellular, and restricted diffusion for cytometry in tumours magnetic resonance imaging. Investive Radiology 2015;50(4):218-227.

130. Panagiotaki E, Schneider T, Siow B, Hall MG, Lythgoe MF, Alexander DC. Compartment models of the diffusion MR signal in brain white matter: A taxonomy and comparison. NeuroImage 2012;59(3):2241-2254.

131. Xu J, Humphrey PA, Kibel AS, Snyder AZ, Narra VR, Ackerman JJH, Song S-K. Magnetic resonance diffusion characteristics of histologically defined prostate cancer in humans. Magnetic Resonance in Medicine 2009;61(4):842-850.

132. Bourne R, Bongers A, Charles N, Power C, Sved P, Watson G. Effect of formalin fixation on biexponential modeling of diffusion decay in prostate tissue. Magnetic Resonance in Medicine 2013;70(4):1160-1166.

133. Field A. Discovering Statistics Using SPSS Third Edition. London: Sage Publications; 2009. 857 p.

134. Kobus T, Laak JAWMVD, Maas MC, Hambrock T, Bruggink CC, Kaa CAHVD, Scheenen TWJ, Heerschap A. Contribution of histopathologic tissue composition to quantitative MR spectroscopy and diffusion-weighted imaging of the prostate. Radiology 2016;278(3):801-811.

135. Iwamuro M, Kondo E, Takata K, Yoshino T, Okada H. Diagnosis of follicular lymphoma of the gastrointestinal tract: A better initial diagnostic workup. World Journal of Gastroenterology 2016;22(4):1674-1683.

136. Dietrich O, Raya JG, Reeder SB, Reiser MF, Schoenberg SO. Measurement of signal-to-noise ratios in MR images: influence of multichannel coils, parallel imaging, and reconstruction filters. Journal of Magnetic Resonance Imaging 2007;26(2):375-385.

137. Basser PJ. Inferring microstructural features and the physiological state of tissues from diffusion-weighted images. NMR in Biomedicine 1995;8(7):333-344.

138. Liang S. Modelling of diffusion-weighted MRI signals in non-neural tissue (Doctoral dissertation): Victoria University; 2017.

139. Cook P, Bai Y, Nedjati-Gilani S, Seunarine K, Hall M, Parker G, Alexander D. Camino: Open-source diffusion-MRI reconstruction and processing. Proceedings of the 14th Annual Meeting International Society for Magnetic Resonance in Medicine 2006;Seattle WA, USA:2759.

140. Cleveland GG, Chang DC, Hazlewood CF, Rorschach HE. Nuclear magnetic resonance measurement of skeletal muscle: anisotrophy of the diffusion coefficient of the intracellular water. Biophysical Journal 1976;16(9):1043-1053.

141. Brownstein KR, Tarr CE. Importance of classical diffusion in NMR studies of water in biological cells. Physical Review A 1979;19(6):2446-2453.

142. Jacobs JG, Johnston E, Freeman A, Patel D, Rodriguez-Justo M, Atkinson D, Punwani S, Brostow G, Alexander DC, Panagiotaki E. Histological validation of VERDICT cellularity map in a prostatectomy case. Proceedings of the 14th Annual Meeting International Society for Magnetic Resonance in Medicine 2016:p2497.

143. Li H, Jiang X, Xie J, McIntyre JO, Gore JC, Xu J. Time-Dependent Influence of Cell Membrane Permeability on MR Diffusion Measurements: Effect of Permeability on Diffusion MR. Magnetic Resonance in Medicine 2016;75(5):1927-1934.

144. Le Bihan D. The 'wet mind': water and functional neuroimaging. Physics in Medicine and Biology 2007;52(7):R57-R90.

145. Hall MG, Bongers A, Sved P, Watson G, Bourne RM. Assessment of non-Gaussian diffusion with singly and doubly stretched biexponential models of diffusion-weighted MRI (DWI) signal attenuation in prostate tissue. NMR in Biomedicine 2015;28(4):486-495.

146. Pyatigorskaya N, Le Bihan D, Reynaud O, Ciobanu L. Relationship between the diffusion time and the diffusion MRI signal observed at 17.2 Tesla in the healthy rat brain cortex. Magnetic Resonance in Medicine 2014;72(2):492-500.

147. Li H, Jiang X, Xie J, McIntyre JO, Gore JC, Xu J. Time-Dependent Influence of Cell Membrane Permeability on MR Diffusion Measurements. Magnetic Resonance in Medicine 2016;75(5):1927-1934.

Research Output

International Conference Proceedings

- **Sahalan**, M., Chatterjee, A., Kurniawan. N., Cowin, G., Gluch, L., Power, C., Watson, G., Tay, K., Fletcher, J., Taylor, D., Bourne, R (2017). *Diffusion-weighted MRI of node tissue: correlation of mean diffusivities and cellularity.* Proc. Intl. Soc. Mag. Reson. Med. 25 (2017) Honolulu, USA.

- **Sahalan**, M., Chatterjee, A., Kurniawan. N., Cowin, G., Gluch, L., Power, C., Watson, G., Tay, K., Fletcher, J., Taylor, D., Bourne, R (2015). *Diffusion-weighted MRI of fixed lymph node tissue,* 39th Annual Meeting of Australian Society for Biophysics jointly with Biophysics Society of Japan (2015), Armidale, Australia

Local Conference Proceedings

- **Sahalan**, M., Kurniawan. N., Cowin, G., Gluch, L., Power, C., Watson, G., Tay, K., Bourne, R. (2014). *Diffusion MRI of Lymph Nodes: Preliminary findings.* Postgraduate Cancer Research Symposium and Imagine U - Creating the Future Higher Degree Research conference, Sydney, Australia

- **Sahalan**, M., Kurniawan. N., Cowin, G., Gluch, L., Power, C., Watson, G., Tay, K., Bourne, R. (2013). *Diffusion MRI of Lymph Nodes: Preliminary findings.* Postgraduate Cancer Research Symposium, Sydney, Australia

Awards and Grants

- International Society for Magnetic Resonance in Medicine (ISMRM) Educational Stipend (2017)

- Australian Society for Biophysics travel award (2015)

Appendix

Ethics Permission for human samples

Contact: Sydney Local Health District Human Research Ethics Committee –
CRGH
Concord Repatriation General Hospital (CRGH)
Concord NSW 2139
Telephone: (02) 9767 5622
Email: crgh.ethics@sswahs.nsw.gov.au

Our Ref: 2015-133

CONCORD
REPATRIATION GENERAL
HOSPITAL

20 August 2015

Dr Roger Bourne
Discipline of Medical Radiation Sciences
Brain and Mind Research Institute
Level 7 94 Mallett St
CAMPERDOWN
NSW 2050

Dear Dr Bourne,

Re: **LNR/15/CRGH/158** **(CH62/6/2015-133)**
Magnetic resonance microimaging of human lymph node tissue

Thank you for submitting the above project for single ethical and scientific review. This project was first considered by the Executive Ethical Review Panel of the Sydney Local Health District Human Research Ethics Committee – CRGH at its meeting held on 4 August 2015. This Human Research Ethics Committee (HREC) has been accredited by the NSW Ministry of Health as a lead HREC under the model for single ethical and scientific review.

This lead HREC is constituted and operates in accordance with the National Health and Medical Research Council's *National Statement on Ethical Conduct in Human Research* and the *CPMP/ICH Note for Guidance on Good Clinical Practice*.

I am pleased to advise that the Committee has granted ethical approval of this research project. The documents reviewed and approved include:

Low & Negligible Risk Research (LNR) Ethics Application Form – submission code
AU/6/E6B0219
Protocol – Version 2 dated 10/08/2015
Letter of invitation
Participant Information Sheet & Consent Form – Version 2 dated 10/08/2015
Data Collection Form – Version 1 dated 10 August 2015 – *page 1 to be stored in separate secure location to page 2.*

The HREC has provided ethical and scientific approval for the following sites:
1. Concord Repatriation General Hospital
2. Brain and Mind Research Institute, University of Sydney

You are reminded that this letter constitutes ethical approval only. You must not commence this research project at Concord Hospital until a Site Specific Application has been reviewed and approved and separate authorisation from the Chief Executive or delegate has been obtained.

Page 1

Please note the following conditions of approval:

1. You will immediately report anything which might warrant review of ethical approval of the project in the specified format, including unforeseen events that might affect continued ethical acceptability of the project, (including Serious Adverse Events).

2. Proposed changes to the research protocol, conduct of the research, or length of HREC approval will be provided to the HREC for review in the specified format.

3. You will notify the HREC, giving reasons, if the project is discontinued at a site before the expected date of completion.

4. This study involves a University of Sydney site and has been approved under an agreement to undertake ethical review for an external entity between the Sydney Local Health District and the University of Sydney. We will include your study in our annual report to the University of Sydney. Should you have questions regarding this agreement or indemnity please contact the University's Clinical Trials Governance group

5. You will provide an annual report to the HREC, and at completion of the study in the specified format.

6. You will adhere to the study protocol at all times.

7. HREC approval is granted on the assumption that all students and early career researchers are adequately supervised by the principal and senior investigators on a project. This supervision would ensure that all privacy concerns are met (including the completion of confidentiality agreements by participating students) and that both students and participants are supported in the conduct of the study in line with the approved research protocol.

HREC approval is valid for five (5) years subject to the supply of an annual progress report. The first report should be sent to the Concord Hospital Research Office by **31/08/2016.**

Should you have any queries about the HREC's consideration of your project please contact the Executive Officer - (02) 9767-5622. The HREC Terms of Reference, Standard Operating Procedures, membership and standard forms are available from the website: www.sswahs.nsw.gov.au/concord/ethics .

We wish you every success in your research.

Please quote the above file number in all correspondence.

Yours sincerely,

Mr Leo Turner
Deputy Chairman
SLHD Human Research Ethics Committee – CRGH

Please complete the boxes below and return a copy of this page to the Concord Hospital Research Office:

☐   *I acknowledge and accept the Conditions of Ethical Approval.*

Ethics Permission for animal samples

From: Animal Ethics

Sent: Wednesday, 16 December 2015 3:57 PM

To: Roger Bourne

Cc: Richard Malik

Subject: Notification of Tissue Sample use- AEC outcomes

Importance: High

Dear Roger,

RE: Supply and use of animal tissues from a pathology laboratory for research purposes.

The Notification of Tissue Sample Use was considered by the Animal Ethics Committee (AEC) on the 15th of December 2015 via out of round review session.

The Committee has approved your Notification of Tissue Sampling request and acknowledges your right to proceed.

Please do not hesitate to contact the Research Integrity (Animal Ethics) Office at animal.ethics@sydney.edu.au should you require further information or clarification.

Warm regards,

Animal Ethics Administration

Office of Research Integrity | Research Portfolio THE UNIVERSITY OF SYDNEY Lv 2 | Margaret Telfer Building (K07) | The University of Sydney | NSW | 2006 T +61 2 8627 8174 | F +61 2 8627 8177 E animal.ethics@sydney.edu.au | W http://sydney.edu.au/ethics

Diffusion-weighted MRI of node tissue: correlation of mean diffusivities and cellularity.

Mariaulpa Sahalan[1], Aritrick Chatterjee[1], Nyoman Kurniawan[2], Gary Cowin[2], Laurence Gluch[3], Carl Power[4], Geoffrey Watson[5], Kevin Tay[6], Julie Fletcher[7], David Taylor[8], Roger Bourne[1]

[1]Faculty of Health Sciences, University of Sydney, NSW, Australia, [2]Centre for Advanced Imaging, University of Queensland, Brisbane, Australia, [3]The Strathfield Breast Centre, NSW, Australia, [4]Biological Resources Imaging Laboratory, University of New South Wales, NSW, Australia, [5]Tissue Pathology and Diagnostic Oncology, Royal Prince Alfred Hospital, NSW, Australia, [6]Westmead Breast Cancer Institute, NSW, Australia, [7]Concord Repatriation General Hospital, NSW, Australia, [8]Vetnostics, NSW, Australia.

Synopsis: Improvement of sensitivity and specificity in DWI-based assessment of nodal diseases is dependent on a better understanding of how nodal microstructures affect the water diffusivity in tissue. In this abstract we report the first diffusion microimaging investigation of formalin fixed node tissue with the aim of assessing any correlation between mean diffusivity and cellularity. Mean diffusivity was calculated in ROI corresponding to distinct node sub-structures. Nuclei were segmented semi-automatically to measure the cellularity metrics: nuclear count and nuclear area. The results showed there is no significant correlation between mean diffusivity with cellularity metrics in the nodal tissues.

Introduction: Diffusion-weighted MRI (DWI) is increasingly being used for detection and assessment of primary tumours but has limited application in secondary diseases such as nodal diseases due to considerable overlap in the range of diffusivities reported for malignant and benign nodes[1,2]. Changes in diffusivity are commonly attributed to variations in 'cellularity' although outside brain tissue evidence is limited. In prostate tissue, changes in partial volume of tissue components with distinct diffusivities (stroma/epithelium/lumen) correlate more strongly with measured ADC than cellularity metrics[3]. Distinct diffusivities of tissue microstructures were reported in prostate and breast tissue[4,5]. Here we report a diffusion microimaging investigation of node tissue with the aim of assessing any correlation between mean diffusivity and cellularity.

Methods: Twenty three formalin fixed node tissue cores (3-mm in diameter) were obtained from eleven subjects. Tissue cores were immersed in 0.2% v/v Magnevist and imaged in a Bruker AV700 with 16.4 T microimaging system (5 mm birdcage RF coil, Micro5 gradient set) using a 3D spin echo DTI sequence with TE/TR = 21/400 ms, $\delta/\Delta = 2/12$ ms , and b-values of 50 ,196 , 435 , 766 , 1190 , 1700, 2307, and 3000 s/mm^2 in 6 directions with two 'b=0' reference measurement at 40m isotropic resolution. Mean diffusivity (MD) was calculated in manually selected regions of interest (ROI) corresponding to distinct node sub-structures: parenchyma in benign, metastatic, and Non-Hodgkin lymphoma. Post imaging tissue was sectioned parallel to the MRI planes and stained with H&E stains. Nuclei were segmented semi-automatically (Figure 1) in Image Pro Premier and used to measure the cellularity metrics: nuclear count and nuclear area. Pearson correlation coefficient was used to compare MD with nuclear count and nuclear area. One way ANOVA with post hoc Tukey test was used to test the difference in MD and cellularity metrics.

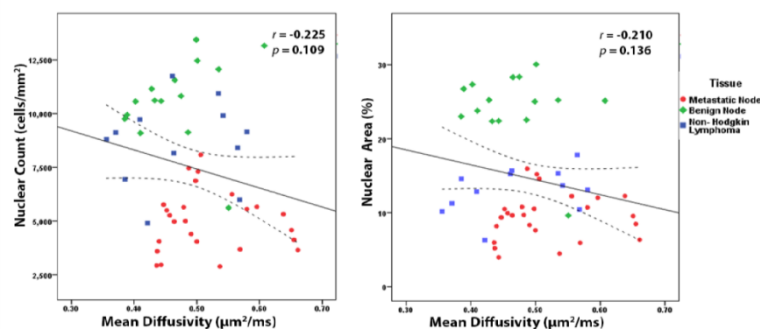|	Benign Node	Metastatic Node	Non- Hodgkin Lymphoma
Mean Diffusivity (μm²/ms)	0.46 ± 0.09	0.52 ± 0.09	0.47 ± 0.13
Nuclear Count (cells/mm²)	10665 ± 250	5021 ± 205	8650 ± 496
Nuclear Area (%)	24.3 ± 1.31	9.5 ± 0.40	13.0 ± 0.63
No. of Subjects	4	4	3
Voxels	19446	26412	14141

Table 1. Summary of cellularity metrics

Figure 2. Correlation of mean diffusivity with cellularity metrics.
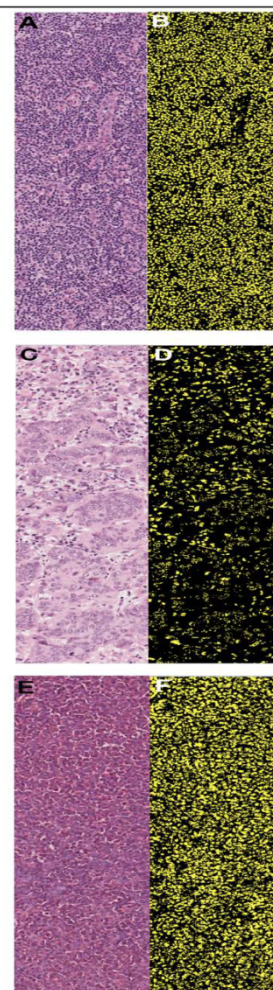
Figure 1. Semi-automated segmentation of H&E stained section images on *RIGHT* column for benign node (A), metastatic node (C), Non-Hodgkin lymphoma (D). Corresponding nuclei were segmented in each nodal diseases for estimation of cellularity in *LEFT* column (B), (E) , (F).

Results and Discussion: Table 1 summarizes the mean diffusivities (MD) values and cellularity measurements in the sub-structure of the node, parenchyma in three different nodal diseases. Distinct diffusivities were found in node sub-structures, higher diffusivity value was found in capsule region as compared to parenchyma region of the node (results not shown). No significant mean diffusivity differences ($F = 2.93$, $p = 0.063$) were evident in benign, metastatic and Non-Hodgkin lymphoma nodes. Benign and Non-Hodgkin nodes shows similar mean diffusivity values of (0.46 ± 0.09 μm²/ms) and (0.47 ± 0.13 μm²/ms) respectively. There were significant differences for the cellularity metrics: nuclear count ($F = 54.41$, $p < 0.05$) and nuclear area ($F = 77.89$, $p < 0.05$). Figure 2 shows the correlation between mean diffusivity with cellularity

metrics of the nodal tissue. Mean diffusivity shows no statistically significant correlation with nuclear count ($r = -0.225$, $p = 0.109$) and nuclear area ($r = -0.21$, $p = 0.136$) (Figure 2). The result from this study was similar to the finding in prostate tissue where diffusivity correlates better gland components than cellularity[3]

Conclusion: Diffusivity in parenchyma region of the three nodal diseases showed no significant difference. There is no significant correlation between mean diffusivity with cellularity metrics in the nodal tissues. This represents a first step towards improving our understanding of DWI-based clinical assessment of nodal disease.

References [1] Sumi et al. AJR. (2006) 186(3):749-57 [2] Kamitani et al. Clin Imag (2013) 37(1):56-61 [3] Chatterjee et a.l Radiology (2012) 68(2):614-20. [4] Bourne et al. Magn Reson Med (2012) 68(2):614-20 [5] Norddin et al. Magn Reson Med (2014) doi:10.1002/mrm.25555.

MATLAB Code

The Matlab code was written by Dr Roger Bourne from University of Sydney for prostate tissue. Modifications were by Mariaulpa Sahalan for application in lymph node tissue.

1. MATLAB Code for Monoexponential Analysis

```matlab
% This function loads the voxel array, as well as the b-values, then goes
through
% and calculates the specific fit for the data
% For multiprocessing, run "matplotlib local <# of processors on machine>"

% Load in the Analyze Data Cube.  Loads as a SpatialImage object.
%NiiImageCube = load_nii('N22.img'); % This loads correctly

% ---------------------------------------------------------------------
-------------------

close all

addpath(fullfile('\Users\msah3230\Documents\Nodes_DataReading_Analysis\N23'
))
NiiImageCube = load_nii('N22.nii'); % This loads correctly
NiiImageData_org = NiiImageCube.img;
NiiImageData = permute(NiiImageData_org,[2 3 1 4]);
[XDim,YDim,ZDim,BDim] = size(NiiImageData); % Get the dimensions of the
data cube
AxisDim = 6 % Number of directional axes in this cube
RefBImages = 2
SignalImagesPerAxis = (BDim-RefBImages)/AxisDim
RefBValue = 16.;
BValueArray = [1098. 1065. 1098. 1065. 1097. 1065.]; % For all axis
measurements b1000
ImageDataArray = zeros(XDim,YDim,ZDim,AxisDim,SignalImagesPerAxis);

% Before running a monoexponential analysis, a cube of tissue data needs to
be analyzed for the noise values
%NoiseSTD = AnalyzeImageCubeSNR();
NoiseSTD = 0.00;
RefDataArray = double(NiiImageData(:,:,:,1:RefBImages)) - NoiseSTD;

% Separate out the axis measurements into the axis dimension
for a = 1:AxisDim
    StartSlice = RefBImages+1+((a-1)*SignalImagesPerAxis);
    EndSlice = RefBImages+(a*SignalImagesPerAxis);
    ImageDataArray(:,:,:,a,:)                                         =
double(NiiImageData(:,:,:,StartSlice:EndSlice)) - NoiseSTD; % use only one
b0 value and subtract the noise
end

% The array will be the same size as the data cube with additional
dimensions for fitted parameters and residuals.
% MonoexpFitArray = zeros(XDim,YDim,ZDim,AxisDim,3); % A0,ADC,RSS
PolyDTIFitArray = zeros(XDim,YDim,ZDim,AxisDim); % ADC
```

```matlab
fit_options  =  optimset('Display',  'off',  'Algorithm',  'trust-region-
reflective','TolX', 1.e-8);

% Setup progress bar
numprofiles = AxisDim*XDim*YDim % exclude inner loop (axisdim)
profilecount = 0;
tic;
h_wb1 = waitbar(0, 'Progress bar');

% Rejig order of looping to put longest loop in parfor
for a = 1:AxisDim
    BValues = [RefBValue, BValueArray(a)]; % Set the b values for this axis
    for i = 1:XDim
        for j = 1:YDim
            % These arrays must be declared to use the parfor
%             FittedA0  = zeros(1,ZDim);
            FittedADC = zeros(1,ZDim);
%             FittedRSS = zeros(1,ZDim);
            profilecount = profilecount + 1;
            for k=1:ZDim
% To fit the signal, merge the reference array with the image array
% Also take the mean of the signal at the b-values before adding to array
                FitSignal          =          [mean(RefDataArray(i,j,k,:)),
ImageDataArray(i,j,k,a,:)];
                if max(FitSignal) > 1000.
                    % Slope   calculation   -   safeguard   against   zero
denominator
                    if FitSignal(2) > 0.
                        FittedADC(k)                                   =
log(FitSignal(1)/FitSignal(2))/(BValues(2)-BValues(1));
                    end
                    %Linear/poly
%                     LogData = log(FitSignal);
%                     [fitdata, S] = polyfit(BValues,LogData,1);
%                     FittedADC(k) = -fitdata(1);
                end
            end
            % Now copy to the main fit array outside of the parfor
%             MonoexpFitArray(i,j,:,a,1) = FittedA0;
%             MonoexpFitArray(i,j,:,a,2) = FittedADC;
            PolyDTIFitArray(i,j,:,a) = FittedADC;
%             MonoexpFitArray(i,j,:,a,3) = FittedRSS;

            % Update progress bar
            inner_loop_time = toc/profilecount;
            time_remaining = (numprofiles-profilecount)*inner_loop_time;
            d=datestr(clock);
            if time_remaining/60 > 180
                waitbar(profilecount/numprofiles, h_wb1,['Estimated  finish
time = ',d(13:17),' plus ', num2str(time_remaining/3600),' hours']);
            else
                waitbar(profilecount/numprofiles, h_wb1,['Estimated  finish
time = ',d(13:17),' plus ', num2str(time_remaining/60),' minutes']);
            end
        end
    end
    sprintf('Outer Loop: %d ',  a)
end
```

```
% Save data array
NewDirName = sprintf('%s', datestr(now, 'yyyyddmm_HHMMSS'));
mkdir(NewDirName);
cd(NewDirName);

% For Nifti data cube save
% NiiFitCube = make_nii(MonoexpFitArray);
NiiFitCube = make_nii(PolyDTIFitArray);

% save_nii(NiiFitCube,'E7b1000MonoexpFitCube.nii')
save_nii(NiiFitCube,'N22b1000PolyFitCube.nii')
cd('..');
close(h_wb1);
toc

%-------------------------------------------------------------------------

function MeasuredNoiseSTD = AnalyzeImageCubeSNR()
NiiNoiseCube = load_nii('N22.img'); % This loads correctly
NoiseDataCube = NiiNoiseCube.img;
[NoiseXDim,NoiseYDim,NoiseZDim,NoiseBDim] = size(NoiseDataCube); % Get the
dimensions of the data cube
% For E7, 40x60x40 are the dimensions
% Check for at least two b0 values
if NoiseBDim < 2
    disp('ERROR: Less than 2 b0 values in reference image cube')
end

% Load in data and analyze
BRefImage1 = NoiseDataCube(:,:,:,1);
BRefImage2 = NoiseDataCube(:,:,:,2); % if there are more images add after
this point and adjust mean/std
NoiseData = double(BRefImage1 - BRefImage2);
MeasuredNoiseSTD = std(NoiseData(:))

% MeasuredSignal = (mean(BRefImage1(:)) + mean(BRefImage2(:)))/2.;
% NoiseMean = mean(BRefImage1(:) - BRefImage2(:))
% SNR = MeasuredSignal/MeasuredNoiseSTD

%-------------------------------------------------------------------------

function signal = MonoexpDecay(x, xdata)
%model function for lsqcurvefit
a0  = x(1);
adc = x(2);
signal = a0*exp(-adc*xdata);

% ----------------------------------------------------------------------
------------------
```

2. MATLAB Code for Diffusion Tensor Analysis

```matlab
% ------------------------------------------------------------------
------------------

close all

% Calculate Diffusion Tensor for D1 and D2 values
TensorImageCube = load_nii('N16b1000PolyFitCube.nii');
TensorImageCube = TensorImageCube.img;
[XDim,YDim,ZDim,AxisDim] = size(TensorImageCube); % Get the dimensions of
the data cube with only D fit parameter

% Now loop through and combine the different parameters into the various
components
TensorCube = zeros(XDim,YDim,ZDim,4,3);
FACube = zeros(XDim,YDim,ZDim);
MDCube = zeros(XDim,YDim,ZDim);

% Enter the gradient matrix from the scan
%ScanDirectionMatrix = [1. 0.5 1.; 1. -0.5 1.; 0.5 1. 1.; -0.5 1. 1.; 1. 1.
0.5; 1. 1. -0.5;];
ScanDirectionMatrix = [0.7 0.3 0.7; 0.7 -0.3 0.7; 0.3 0.7 0.7;-0.3 0.7 0.7;
0.7 0.7 0.3; 0.7 0.7 -0.3;];
GradientMatrix          =          (1/2.25)*[ScanDirectionMatrix(:,1).^2
ScanDirectionMatrix(:,2).^2 ScanDirectionMatrix(:,3).^2 ...
    2*ScanDirectionMatrix(:,1).*ScanDirectionMatrix(:,2)
2*ScanDirectionMatrix(:,1).*ScanDirectionMatrix(:,3) ...
    2*ScanDirectionMatrix(:,2).*ScanDirectionMatrix(:,3)]

% Now loop through and calculate all values for each voxel
for i = 1:XDim
    for j = 1:YDim
        for k = 1:ZDim
            % Create both the fast and slow values.
            CurrentVoxelADC         =         1000.*[TensorImageCube(i,j,k,1);
TensorImageCube(i,j,k,2); TensorImageCube(i,j,k,3); ...
                TensorImageCube(i,j,k,4);         TensorImageCube(i,j,k,5);
TensorImageCube(i,j,k,6)];

            % Exclude if any of diffusion values are zero
            if all(CurrentVoxelADC)
                DTValues = GradientMatrix\CurrentVoxelADC;
                % Use values to calculate the diffusion tensor matrix
                DTMatrix = [DTValues(1) DTValues(4) DTValues(5);...
                        DTValues(4) DTValues(2) DTValues(6);...
                        DTValues(5) DTValues(6) DTValues(3)];

                % Calculate eigenvalues
                [VMatrix,EigMatrix] = eig(DTMatrix);
                Lambda = diag(EigMatrix);

                % Save tensor data
                TensorCube(i,j,k,1,:) = Lambda';
                TensorCube(i,j,k,2:4,:) = VMatrix;

%      Save nifti data
%      NiftiTensorCube(i,j,k,:) = [DTValues(1) DTValues(4) DTValues(5) ...
```

```matlab
%         DTValues(4) DTValues(2) DTValues(6) ...
%         DTValues(5) DTValues(6) DTValues(3)];

                % ANISOTROPY AND MEAN DIFFUSIVITY CALCULATIONS
                Numerator  =  sqrt((Lambda(1)-Lambda(2))^2  +  (Lambda(1)-
Lambda(3))^2 + (Lambda(3)-Lambda(2))^2);
                Denominator  =  sqrt(2*(Lambda(1)^2  +  Lambda(2)^2  +
Lambda(3)^2));
                FACube(i,j,k)  =  Numerator./Denominator;  %  Fractional
Anisotropy
                MDCube(i,j,k) = mean(Lambda); % Mean Diffusivity

            end
        end
    end
end

% Histogram of Mean Diffusivity
MDValues = reshape(MDCube,XDim*YDim*ZDim,1);

% ReducedMDCube = ReducedMDCube(ReducedMDCube < 5.1); % If you want to
restrict the range, use this
% ReducedMDCube = ReducedMDCube(ReducedMDCube > 0.); % If you want to
restrict the range, use this
figure;hist(MDValues,200);title('Histogram of MD values');

% Histogram of FA
FAValues = reshape(FACube,XDim*YDim*ZDim,1);
figure;hist(FAValues,200);title('Histogram of FA values');

% 2D Histogram of FA vs MD for ADC
MDValues = reshape(MDCube,XDim*YDim*ZDim,1);
FAValues = reshape(FACube,XDim*YDim*ZDim,1);
FAMDHistValues = [MDValues FAValues];
MDBinWidth = 0.025;
MDBins = 0:MDBinWidth:2.5;
FABinWidth = 0.025;
FABins = 0:FABinWidth:1.25;
figure;hist3(FAMDHistValues, 'edges', (73));
set(gcf, 'renderer', 'opengl');
set(get(gca,'child'), 'FaceColor', 'interp', 'CDataMode', 'auto');
view(2)
caxis([0 250]); % scale the histogram colorbar range
title('2D Histogram of FA vs. MD for ADC values');

% Display an image slice
figure;h1 = imagesc(FACube(:,:,15));
figure;h2 = imagesc(MDCube(:,:,15));

stophere = 1;
return

% ------------------------------------------------------------------------
------------------
```